AD-A064 149 SCIENCE APPLICATIONS INC MCLEAN VA F/G 18/3
THEORETICAL AIR BLAST LOADING ESTIMATES ON THE M-X SHELTER, THE--ETC(U)
JUN 78 B S CHAMGERS, D T HOVE, R I ISSA DNA001-77-C-0059
UNCLASSIFIED SAI-78-503-AO DNA-4610F NL

1 OF 2
AD
A064149

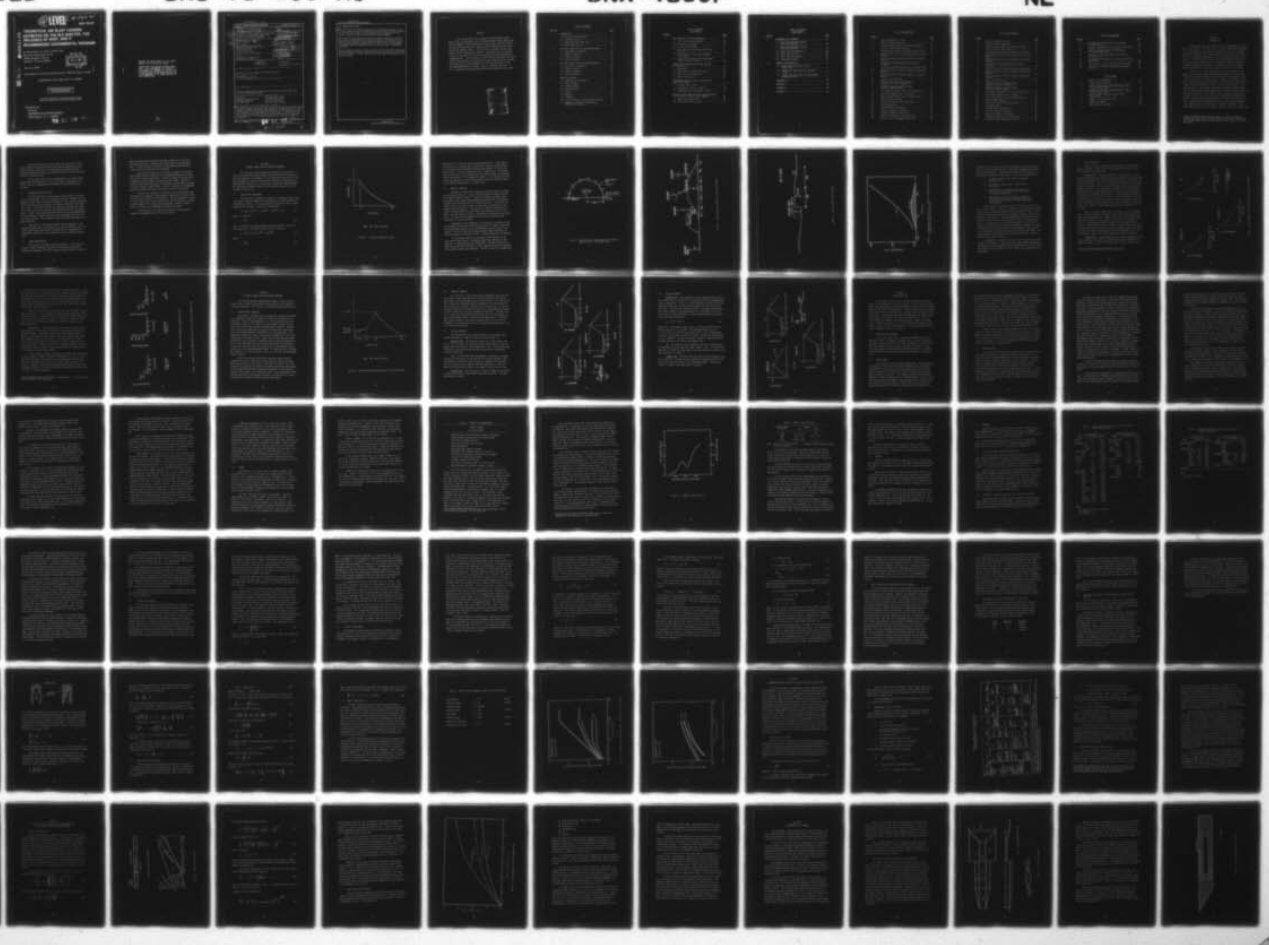

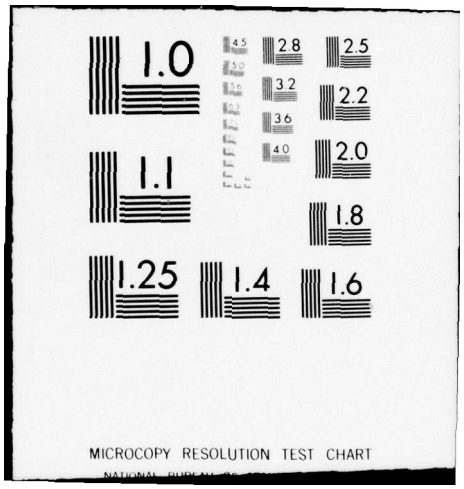
1.0
1.1
1.25
1.4
1.6
1.8
2.0
2.2
2.5
2.8
3.2
3.6
4.0
4.5
5.0
MICROCOPY RESOLUTION TEST CHART

(12) LEVEL II AD-E300 414
NW

DNA 4610F

THEORETICAL AIR BLAST LOADING ESTIMATES ON THE M-X SHELTER, THE INFLUENCE OF DUST, AND A RECOMMENDED EXPERIMENTAL PROGRAM

B. Chambers, D. Hove, and R. Issa
Science Applications, Inc.
8400 Westpark Drive
McLean, Virginia 22101

DDC
RECEIVED
FEB 5 1979
B

30 June 1978

Final Report for Period 8 November 1976—31 March 1978

CONTRACT No. DNA 001-77-C-0059

APPROVED FOR PUBLIC RELEASE;
DISTRIBUTION UNLIMITED.

THIS WORK SPONSORED BY THE DEFENSE NUCLEAR AGENCY
UNDER RDT&E RMSS CODE B344077464 Y99QAXSG65507 H2590D.

Prepared for
Director
DEFENSE NUCLEAR AGENCY
Washington, D. C. 20305

78 11 28 020

DDC FILE COPY AD A064149

Destroy this report when it is no longer needed. Do not return to sender.

PLEASE NOTIFY THE DEFENSE NUCLEAR AGENCY, ATTN: TISI, WASHINGTON, D.C. 20305, IF YOUR ADDRESS IS INCORRECT, IF YOU WISH TO BE DELETED FROM THE DISTRIBUTION LIST, OR IF THE ADDRESSEE IS NO LONGER EMPLOYED BY YOUR ORGANIZATION.

UNCLASSIFIED

SECURITY CLASSIFICATION OF THIS PAGE (When Data Entered)

REPORT DOCUMENTATION PAGE

READ INSTRUCTIONS BEFORE COMPLETING FORM

1. REPORT NUMBER: DNA 4610F, AD-E300 414
2. GOVT ACCESSION NO.:
3. RECIPIENT'S CATALOG NUMBER:
4. TITLE (and Subtitle): THEORETICAL AIR BLAST LOADING ESTIMATES ON THE M-X SHELTER, THE INFLUENCE OF DUST, AND A RECOMMENDED EXPERIMENTAL PROGRAM.
5. TYPE OF REPORT & PERIOD COVERED: Final Report for Period 8 Nov 76—31 Mar 78
6. PERFORMING ORG. REPORT NUMBER: SAI-78-503-AO
7. AUTHOR(s): Burton S. Chambers, III; Duane T. Hove; Raad I. Issa
8. CONTRACT OR GRANT NUMBER(s): DNA 001-77-C-0059
9. PERFORMING ORGANIZATION NAME AND ADDRESS: Science Applications, Inc., 8400 Westpark Drive, McLean, Virginia 22101
10. PROGRAM ELEMENT, PROJECT, TASK AREA & WORK UNIT NUMBERS: NWED Subtask Y99QAXSG655-07; G655
11. CONTROLLING OFFICE NAME AND ADDRESS: Director, Defense Nuclear Agency (SPSS), Washington, D.C. 20305
12. REPORT DATE: 30 June 1978
13. NUMBER OF PAGES: 146
14. MONITORING AGENCY NAME & ADDRESS (if different from Controlling Office): 143p.
15. SECURITY CLASS (of this report): UNCLASSIFIED
15a. DECLASSIFICATION/DOWNGRADING SCHEDULE:
16. DISTRIBUTION STATEMENT (of this Report): Approved for public release; distribution unlimited. DNA, SBIE
17. DISTRIBUTION STATEMENT (of the abstract entered in Block 20, if different from Report):
18. SUPPLEMENTARY NOTES: This work sponsored by the Defense Nuclear Agency under RDT&E RMSS Code B344077464 Y99QAXSG65507 H2590D.
19. KEY WORDS (Continue on reverse side if necessary and identify by block number)

Air Blast	Pre-Shock Dust Lofting
Nuclear Air Blast Precursor	Post-Shock Dust Lofting
Non-Ideal Blast Wave	Air Blast Simulation
Air Blast Loads	Shock Tube Test Planning

20. ABSTRACT (Continue on reverse side if necessary and identify by block number)

This report discusses three activities performed in support of the M-X concept validation program, each specifically addressing various aspects of air blast loading on the M-X above-ground shelter concept. The three activities were (1) estimation of air blast loads on the M-X shelter; (2) modeling the pre- and post-shock dust lofting for air blast calculations; and (3) shock tube test planning for air blast loads measurements on a small scale model of M-X shelter.

DD FORM 1 JAN 73 1473 EDITION OF 1 NOV 65 IS O[illegible]

78 11 28 020

UNCLASSIFIED

SECURITY CLASSIFICATION OF THIS PAGE (When Data Entered)

(over)

408 404 LB

20. ABSTRACT (Continued)

The first activity involved the generation of engineering estimates of the air blast loading on two orientations (end-on and side-on) of the M-X shelter for ultimate use by others for setting up structural response code calculations. Both ideal and precursed waveforms were considered.

The second activity involved a review of the nuclear data base to identify data useful to understanding the relative importance of lofted dust in the flow on air blast loading. Also theoretical models used for late-time dust lofting were reviewed to determine their utility to the air blast problem. A recommended model was developed for future inclusion into a hydrodynamic code, HULL.

The third activity involved a review of shock tubes in the United States that would be appropriate for use in measuring the air blast loads on a small model of the M-X shelter. The CERF shock tube was chosen and an experimental program was planned.

A

1473B

PREFACE

The work described in this report was performed by Science Applications, Incorporated (SAI) for Defense Nuclear Agency (DNA) under contract DNA001-77-C-0059 entitled "Air Blast Loads on the M-X Shelter." The work performed under this contract covers principally three independent but related efforts. The first was to estimate the air blast loads on the M-X above-ground shelter. The second was to review dust lofting in the context of air blast calculations and make appropriate recommendations. The third was to review existing shock tube facilities, choose one appropriate for measuring air blast loads on the M-X shelter and develop a test plan appropriate to the time constraints of the joint DNA/SAMSO/AFWL M-X Program. Capt. J. Stockton, USAF, and Mr. T. Kennedy were the DNA Contracting Officer Representatives (COR).

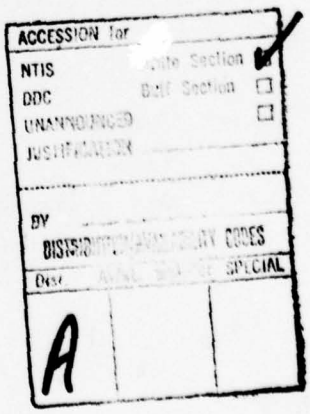

TABLE OF CONTENTS

SECTION		PAGE
1	INTRODUCTION	7
	1.1 Air Blast Loads Estimates	8
	1.2 Influence of Dust	8
	1.3 Laboratory Shock Tube Tests	10
	1.4 Report Organization	10
2	AIR BLAST LOADS FOR THE CLASSICAL WAVEFORM	12
	2.1 Description of Waveform	12
	2.2 Method of Analysis	14
	2.3 Side-On Incidence	20
	2.4 End-On Incidence	22
3	AIR BLAST LOADS FOR THE PRECURSOR WAVEFORM	26
	3.1 Description of Waveform	26
	3.2 Method of Analysis	28
	3.3 Side-On Incidence	28
	3.4 End-On Incidence	30
4	NUCLEAR DATA BASE	32
	4.1 Sandstone and Greenhouse	32
	4.2 Buster-Jangle	32
	4.3 Tumbler-Snapper	33
	4.4 Upshot-Knothole	37
	4.5 Teapot	40
	4.6 Redwing	46
	4.7 Plumbbob	47
	4.8 List of Precursor and Non-Precursor Shots	47
	4.9 Summary of Conclusion from NTS Data Related to Air Blast	47

TABLE OF CONTENTS
(continued)

SECTION		PAGE
5	POST-SHOCK DUST LOFTING MECHANISMS	51
	5.1 IITRI Dust Environment Model	51
	5.2 ATI Dust Lofting Model	53
	5.3 S^3 Dust Lofting Model	55
	5.4 Dust Lofting by the Nuclear Air Blast Precursor	60
	5.5 Applicability of Dust Lofting Models to Air Blast	61
	5.6 Wind Tunnel and Shock Tube Experimental Studies of Dust Lofting	62
6	SIMPLE ANALYTIC MODEL FOR THERMAL BLOW-OFF OF PRESHOCK DUST	64
	6.1 Background	64
	6.2 Attenuation of Radiation by Dust	65
	6.3 Model for Dust Production	67
	6.4 Model Sensitivities	69
7	RECOMMENDED MODELS FOR DUST LOFTING IN AIR BLAST CALCULATIONS	73
	7.1 Preshock Dust Lofting	73
	7.2 Aerodynamic Lofting in SCOUR 2	74
	7.3 Implementation of the Models in HULL	76
8	REVIEW OF SHOCK TUBE FACILITIES FOR APPLICATION TO M-X SHELTER AIR BLAST LOADS PROGRAM	80
	8.1 Shock Tube Capabilities	80
	8.2 Shock Tube Facility Survey	83

TABLE OF CONTENTS
(continued)

SECTION		PAGE
9	RECOMMENDED TEST PROGRAM	87
	9.1 Shock Tube Experiment Design - Classical Waveforms	88
	9.2 Shock Tube Experiment Design - Precursor Waveforms	96
	9.3 Shock Tube Instrumentation	104
	9.4 Shock Tube Test Plan	106
	9.5 Shock Tube Data Analysis	107
	9.6 Theoretical Support	110
10	SUMMARY AND CONCLUSIONS	111
	10.1 Summary and Conclusions for Air Blast Loads	111
	10.2 Summary and Conclusions for Influence of Dust	111
	10.3 Summary and Conclusions for Experimental Program Planning	112
	REFERENCES	113
	APPENDIX A	119
	APPENDIX B	127
	APPENDIX C	131

LIST OF ILLUSTRATIONS

NUMBER		PAGE
1	Classical Waveform of Pulse.....	13
2	Relative Shelter Dimensions.....	15
3	Idealized Shock Loading for Side-On Incidence.....	16
4	End-On Incidence Shock Loading.....	17
5	Instantaneous Pressure Distribution within Pulse...	18
6	Shelter Loading for Side-On Incidence of Classical Waveform.....	21
7	Shelter Loading for End-On Incidence of Classical Waveform.....	23
8	Comparison with DABS Experiment for End-On Incidence.....	25
9	Scaled Precursor Waveform Used for Estimated Loads.	27
10	Shelter Loading for Side-On Incidence on Precursor Waveform.....	29
11	Shelter Loading for End-On Incidence of Precursor Waveform.....	31
12	Teapot 12 Dust Densities.....	44
13	Parameter Studies on Blow-Off Model: Geometrical vs. Mie Screening.....	71
14	Parameter Studies on Blow-Off Model: Effect of Blow-Off Energy.....	72
15	Flux Normal to Ground from a 2 MT Surface Burst.....	78
16	Shock Tube Schematic and X-T Diagram.....	81
17	Shock Strength versus Initial Pressure Ratio.....	84
18	Shelter Model Dimensions.....	89
19	Shock Tube Ground Plane Cross-Section.....	91
20	Test Model Insert.....	92
21	Selected Model Orientations.....	93
22	Pressure Transducer Locations.....	94
23	Example Transducer Installation.....	95
24	Precursor Formation in CERF Shock Tube.....	98
25	Heated Air Layer Temperature Profiles.....	99

LIST OF ILLUSTRATIONS

NUMBER		PAGE
1	Classical Waveform of Pulse.....	13
2	Relative Shelter Dimensions.....	15
3	Idealized Shock Loading for Side-On Incidence.....	16
4	End-On Incidence Shock Loading.....	17
5	Instantaneous Pressure Distribution within Pulse...	18
6	Shelter Loading for Side-On Incidence of Classical Waveform.....	21
7	Shelter Loading for End-On Incidence of Classical Waveform.....	23
8	Comparison with DABS Experiment for End-On Incidence.....	25
9	Scaled Precursor Waveform Used for Estimated Loads.	27
10	Shelter Loading for Side-On Incidence on Precursor Waveform.....	29
11	Shelter Loading for End-On Incidence of Precursor Waveform.....	31
12	Teapot 12 Dust Densities.....	44
13	Parameter Studies on Blow-Off Model: Geometrical vs. Mie Screening.....	71
14	Parameter Studies on Blow-Off Model: Effect of Blow-Off Energy.....	72
15	Flux Normal to Ground from a 2 MT Surface Burst.....	78
16	Shock Tube Schematic and X-T Diagram.....	81
17	Shock Strength versus Initial Pressure Ratio.....	84
18	Shelter Model Dimensions.....	89
19	Shock Tube Ground Plane Cross-Section.....	91
20	Test Model Insert.....	92
21	Selected Model Orientations.....	93
22	Pressure Transducer Locations.....	94
23	Example Transducer Installation.....	95
24	Precursor Formation in CERF Shock Tube.....	98
25	Heated Air Layer Temperature Profiles.....	99

LIST OF ILLUSTRATIONS

NUMBER		PAGE
26	Equivalent Air Temperature for a Hydrogen/ Nitrogen Mixture	103
27	Schematic Representation of Precursor Flow Field	120
28	Geometric Nomenclature Used in Derivation of Fireball Shape Factor	132
29	Percent Error of Point Source as a Function of h/R_f for $r/R_f = 2$.	
30	Nomenclature for Derivation of Effective Reflection Coefficient	137
31a	Variation of $x \equiv R'_f/R_f$ with Scaled Burst Height	139
31b	Variation of Effective Yield with Scaled Burst Height	139

LIST OF TABLES

1	Teapot 12 Instrumentation	42
2	Teapot 12 Dust Densities	45
3	Established Precursor and Non-Precursor Shots: Trinity through Teapot	48
4	Established Precursor and Non-Precursor Shots: Redwing through 1962	49
5	Blow-Off Model Parameter Values for NTS Calculations	70
6	Summary of Soil Blow-Off Data	75
7	Summary Test Matrix	108
8	Shock Tube Test Schedule	109

SECTION 1
INTRODUCTION

Presented below are the results of three independently performed but related efforts. The first effort resulted in engineering estimates of air blast loads on the M-X above-ground shelter due to a 1 megaton nuclear surface burst. The second resulted in a review of dust lofting as well as recommended approaches for future precursed air blast calculations. The third resulted in a review of existing shock tube facilities, and then for one such facility a test plan. Before proceeding a summary paragraph on precursors is provided since each discussion assumes some familiarity with the subject on the part of the reader.

During the U.S. above-ground nuclear testing programs at the Nevada Test Site (NTS), many single nuclear bursts over dry dusty surfaces led to waveforms altered from those that would be expected from a nuclear burst over an ideal* surface at ranges of strategic interest (e.g., the nuclear air blast precursor). The formation of the precursor results from the propagation of the air blast into a hot layer of air, characterized by a high sound speed, that has previously been created over the ground by the complex interaction of thermal radiation from the burst with the ground. The resultant static overpressure and dynamic pressure of the air blast at points near the surface have been seen to be quite different from those expected over a thermally reflecting surface. Instead of the instantaneous rise to a single peak followed by an exponential decay, the waveform, for example, can consist of two peaks each having a finite rise time. Typically, the static overpressure

*Ideal surfaces are those that are perfectly rigid and reflecting, whereas non-ideal surfaces are those that can interact with the fireball thermal radiation and possibly generate a hot thermal layer above the ground.

peaks are less than the single peak expected over ideal surfaces. On the other hand, the dynamic pressure has been seen to be two to three times as great as that over the ideal surface.

1.1 AIR BLAST LOADS ESTIMATES

Other organizations, tasked with performing simple structural response calculations for DNA, needed estimates of the air blast loads on the M-X shelter in order to set up and perform their calculations. These estimates were generated by SAI via applications of various well known techniques for ideal waveforms. In addition, gross estimates were made for precursed type waveforms obtained by extrapolation of similar waveforms from nuclear shots at NTS with yields of tens of kilotons and various heights of bursts (no surface bursts).

The calculations reported here are engineering estimates of the loads on the M-X shelter due to a nuclear 1 megaton surface burst. Both classical and precursor affected waveforms were considered. The results of the calculations provided the pressure-time variations at the centers of the side walls and roof of the M-X shelter for side-on as well as end-on incidence of the waves, and were provided to the community early in the program in briefing form (Reference 1). The results were subsequently compared with numerical solutions of the equations of inviscid flow and with available experimental data, and those comparisons are also included.

1.2 INFLUENCE OF DUST

Since precursors have not been observed to form over water, experimental precursor data do not exist for megaton size bursts. These data only exist for bursts in the tens of kt range. Precursor effects are not scaleable in the usual sense since more thermal energy is deposited on the ground by a higher yield nuclear weapon than deposited by a lower yield nuclear weapon at the same given scaled range both after and before the air shock arrives. Hence dynamic pressure could be increased (or decreased) as yield increases.

The only means available by treaty to study precursor effects at yields of strategic interest is through a combination of theoretical analysis (e.g., calculations) and experimental simulation. Previous AFWL calculations (References 2 and 3) for example, have shown that a precursor can be caused to form calculationally with a hydrodynamic computer code when energy is deposited in near surface zones. In these studies, however, no dust was considered in the flow and although significant enhancements in dynamic pressure are obtainable using simply heated layers (ignoring for the moment the fact that these layers get heated via conduction from the preshock lofted dust), no attempt had been made at the time this effort was started to understand what effects would result for plausible dust densities.

Since in the M-X Validation Phase the Air Force is considering land mobile systems sited in dry, dusty areas, it is reasonable to expect that dusty flow could be of some importance. One M-X concept consists of partially buried shelters whose damage could be increased by an enhancement of the dynamic pressure.

In order to be able to perform dusty flow calculations, a model of the dust lofting process is needed that will be appropriate for air blast calculations rather than other applications (e.g., late time dust cloud loading). The principal distinction is that the lofting processes of interest here are those that will directly affect the air blast propagation itself. (This in turn could affect late time lofting.) For a 1 megaton surface burst the air blast will be affected over times of the order of tens to hundreds of milliseconds whereas the late time lofting occurs over seconds to minutes.

The procedure followed in the course of this effort was first to review the nuclear data base to identify those data useful to understanding the relative importance of lofted dust in the flow on air blast loading. That review consisted primarily of a review of other work that was done earlier in the late time dust lofting community. Other laboratory data were reviewed as deemed appropriate.

The second main thrust of this effort was the review of theoretical efforts that had identified dust lofting mechanisms and estimated lofted dust densities. The formulations representing these mechanisms were then evaluated to determine which ones should (and then could) be included in HULL.

Finally, this effort led to recommendations as to which mechanisms would be appropriate for use in any future calculations. As a result, specific recommendations (and models) were formulated (and revised).

1.3 LABORATORY SHOCK TUBE TESTS

Estimates made of air blast loads on the M-X shelter indicate that the loads appear to be less severe for precursor waveforms (in the absence of dust) than for classical waveforms. Peak reflected pressures are not as high, and the precursor toe causes the loading to be spread out in time. This lack of severity is contrary to weapons test experience, and points out the uncertainty associated with precursor predictions. There is some indication that precursors may be accompanied by a large increase in dynamic pressure, which presumably would increase the structure loads. The influence of dust on the shelter loads has not been quantified.

Proof tests of the shelter loads are being conducted in the large scale DABS series S experiments for classical waveforms, but laboratory shock tubes provide a more flexible tool to experimentally investigate classical air blast loads and could also produce precursor loads.

1.4 REPORT ORGANIZATION

This report is divided into four main parts. The first part, Sections 2 and 3, addresses the effort associated with providing engineering estimates of air blast loads on the M-X shelter. Section 2

deals with the loading resulting from the incidence of a classical waveform and Section 3 considers the loading from a precursed waveform. In both sections, discussions of the waveform, the method of analysis and the calculations are presented.

The second part consists of Sections 4 through 7 and reviews dust lofting and the formulation of a recommended approach for future precursed air blast calculations. Section 4 summarizes the pertinent information available from a nuclear data base review. Section 5 reviews certain post-shock dust lofting models, and Section 6 discusses a pre-shock thermal blowoff model. Section 7 presents the recommended approach to modeling the dust lofting for air blast calculations.

The third part consists of Sections 8 and 9 and addresses the formulation of a program to experimentally measure the air blast loads on a small scale model of the M-X shelter. Section 8 presents a review of shock tube facilities and a selection of one for design of an experimental program of air blast loads measurements on the M-X shelter. Section 9 presents the recommended experimental program.

Finally Section 10, contains the principal conclusions and summary of recommendations for the entire effort.

SECTION 2
AIRBLAST LOADS FOR THE CLASSICAL WAVEFORM

This section presents engineering estimates of the airblast loads on the M-X above ground shelter resulting from the incidence of a classical waveform. The waveform is first described (Section 2.1), and then the method of analysis including the simplifying assumptions and approximations (Section 2.2) is described. Results are then presented for the side-on incidence (Section 2.3) followed by those for end-on incidence (Section 2.4).

2.1 DESCRIPTION OF WAVEFORM

The blast wave considered is that due to a megaton surface burst. The range of interest (1840 feet) corresponds to a peak overpressure at the shelter of 600 psi. The overpressure variation with time is shown schematically in Figure 1, and can be expressed as:

$$\Delta p = 600\ (.23e^{-2.6\tau} + .35e^{-21\tau} + .42e^{-110\tau})\ (1-\tau) \qquad (1)$$

where τ is given by

$$\tau \equiv \frac{t}{1.1} \qquad (2)$$

and t is the time in seconds measured from the instant of arrival of the shock front. The dynamic pressure pulse is given by:

$$Q = 1470\ (1-w)^2\ (.4e^{-90w} + .6e^{-260w}) \qquad (3)$$

where:

$$w \equiv \frac{t}{2.5} \qquad (4)$$

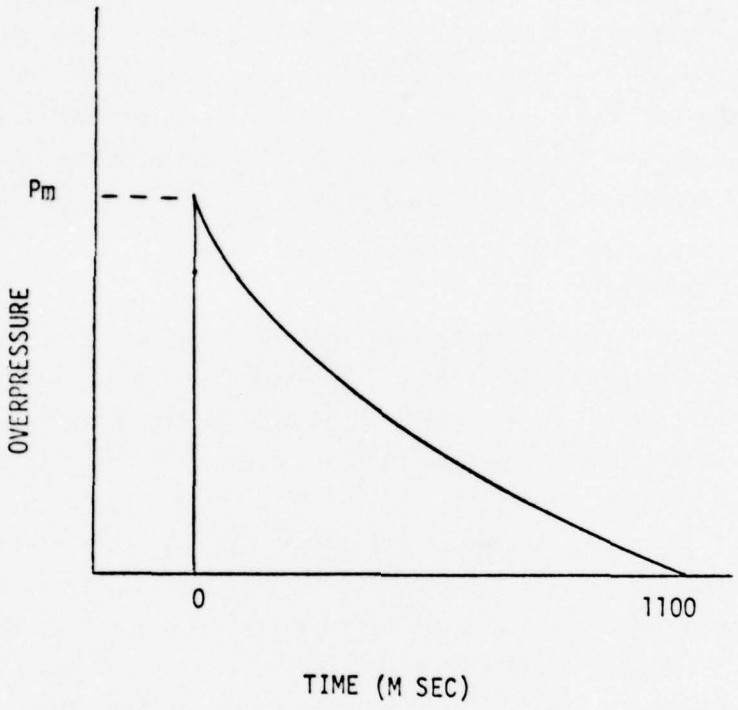

NOTE: PM = 600 psi nominal

Figure 1. Classical waveform or pulse.

Expressions (1) to (4) are given by Brode (Reference 4). Other quantities which are of interest and are obtainable from the cited reference are the radius of the hemispherical blast wave (1840 ft. or 561 m) and the velocity of the shock front (6700 ft/s or 2040 m/sec). The proportion of the radius of the hemispherical blast wave relative to the dimensions of the shelter is illustrated in Figure 2. It is evident from the figure that the part of the blast wave which interacts with the shelter can be treated approximately as a plane front.

2.2 METHOD OF ANALYSIS

Two modes of interaction between the blast wave and the shelter are considered; they are: side-on incidence shown in Figure 3 and end-on incidence shown in Figure 4. Loads on structures are often calculated with a quasi-steady drag assumption using the free field dynamic pressure and an average value of a "drag coefficient." This gives the dynamic load at any given instant of time given the variation of the dynamic pressure with time. This approach is good for evaluating the loads on surfaces which are traversed by the pressure pulse in a very short time such that the surface is subjected to the same pressure everywhere. In practice, the approach can be used for relatively small structures or for vertical walls.

Examination of the dimensions of the shelter in relation to the instantaneous distribution of the pressure pulse in Figure 5 shows that the instantaneous pressure varies considerably along each face of the shelter. The use of the quasi-steady approach cannot, therefore, be justified except for the vertical door. Another method must be employed.

In the present method of calculation, the deflection of the blast wave at each corner is considered separately, whereby the overpressure is calculated after each deflection. The wave system set up after the successive deflections is quite complex and cannot be analyzed fully except by numerical techniques. In order to arrive at engineering

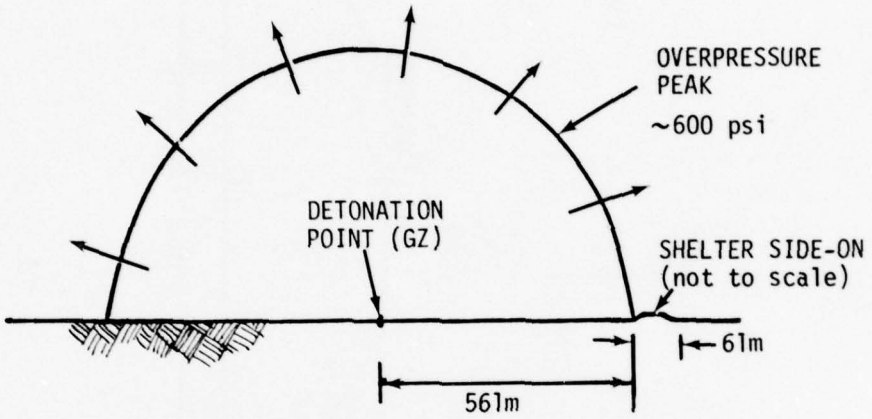

Figure 2. Relative shelter dimensions with respect to 600 psi from a 1 MT surface burst.

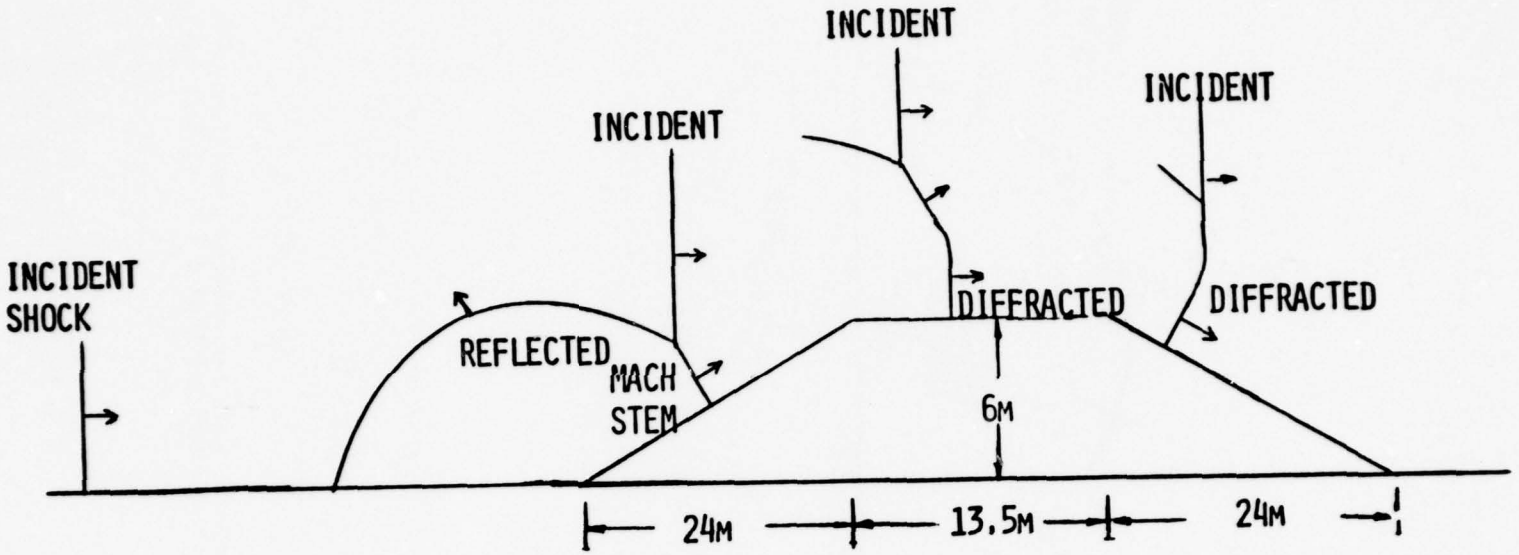

Figure 3. Idealized shock loading for side-on incidence.

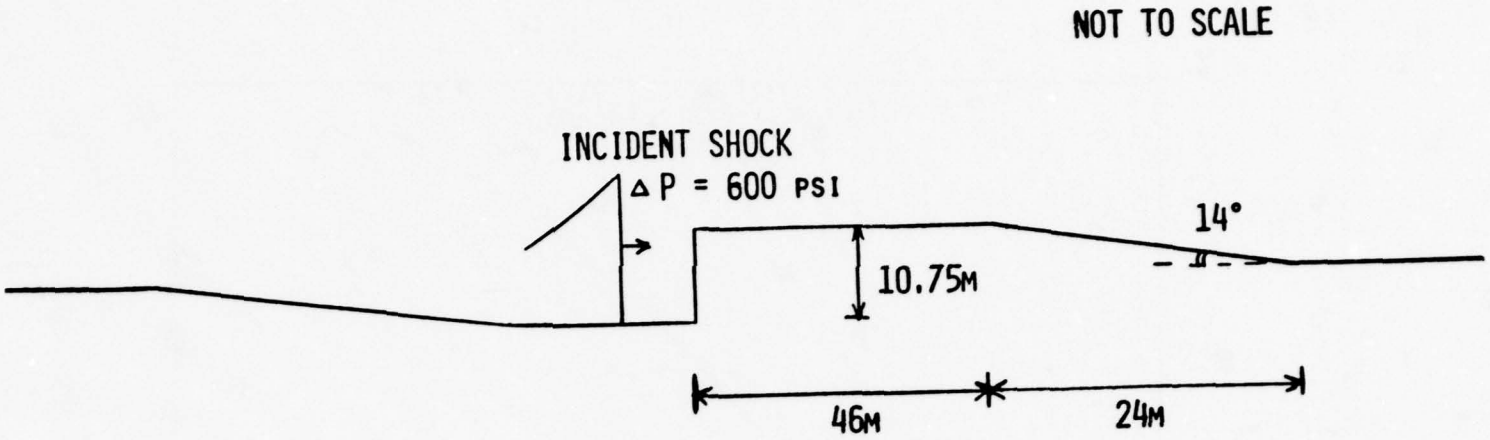

Figure 4. End-on incidence shock loading

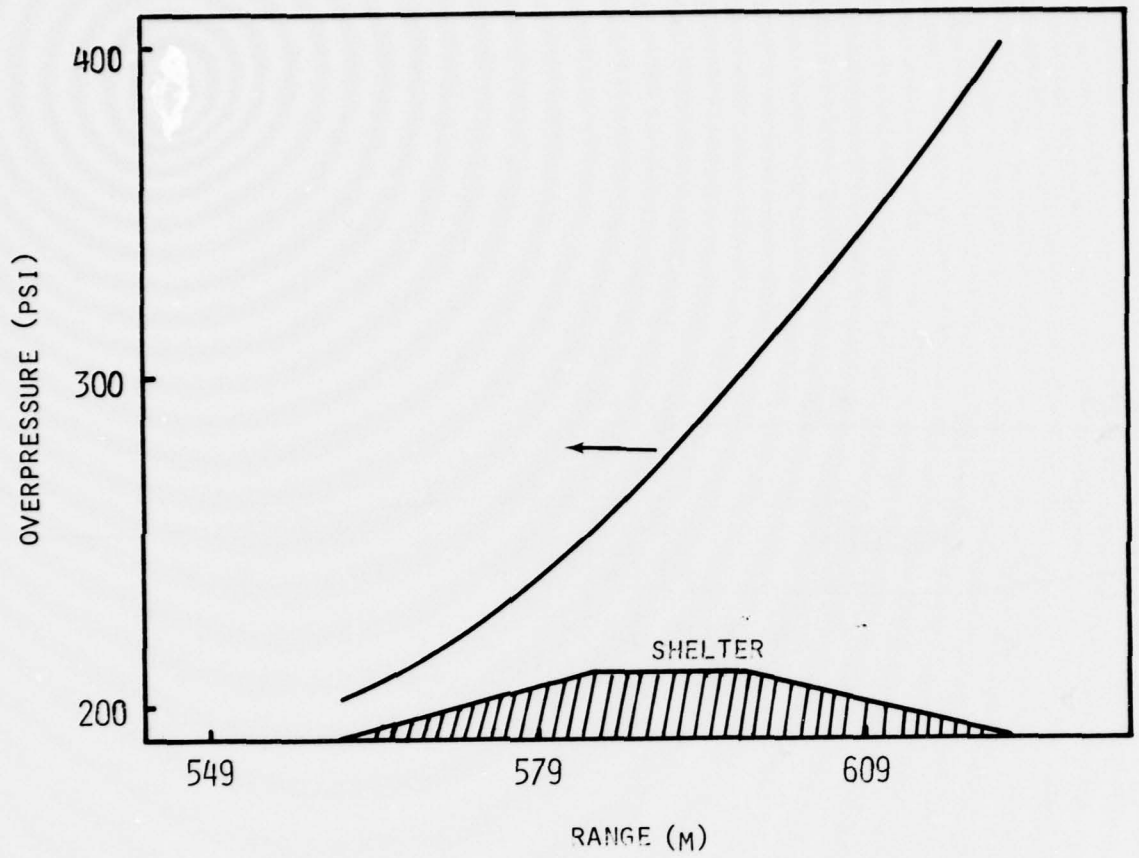

Figure 5. Instantaneous free field (i.e., without interaction with shelter) pressure distribution within pulse.

estimates of the overpressure after each deflection without having to resort to sophisticated techniques, simplifying assumptions are introduced into the analysis. The assumptions made herein are based on experimental observations (Reference 5). They can be summarized by:

(i) The generic shape of the pulse is unaltered by deflections.

(ii) The duration of the pulse is unaffected by deflections.

(iii) The reflection of the peak overpressure is idealized by the reflection of a single shock of the same overpressure.

(iv) The pressure in the pulse after reflection is determined by scaling the incident pressure by the same reflection factor as that for the peak overpressure.

These assumptions obviate the need to analyze the whole of the wave system in detail. All that is required is to calculate the reflection factor for the peak overpressure at each change of slope. These factors are determined by the use of Whitham's method as follows (see Reference 5 for details). Given the Mach number of the shock front, a value for a function w called the Whitham function is obtained from a chart. To this value of w, the deflection angle of the surface (in radians) is either added or subtracted depending on whether the change in slope gives rise to a compression or an expansion. The new value of w is then used to obtain a new value for the shock Mach number from the same chart. The pressure across the deflected shock is then obtained from the shock relations.

An exception is made in the case of the reflection at the vertical door of the shelter. There, the quasi-steady method recommended in Reference 6 is used to determine the average pressure load on the door. This method is more suited to vertical surfaces than the approach outlined above.

2.3 SIDE-ON INCIDENCE

Figure 3 shows an idealized shock reflection at the shelter for side-on incidence. Details of the calculation of the pressure after each deflection are given below.

Windward Face: The shock undergoes a Mach reflection at the foot of the sloping face, and the strength of the Mach stem is determined by Whitham's method. The reflection factor obtained is 1.24 which gives a peak overpressure of 744 psi. As suggested in Reference 5, this figure should be increased by a 20% uncertainty factor to give a conservative estimate of 890 psi. The value agrees reasonably well with reflection factors obtained by experiment (Reference 7) and by finite-difference calculations by Srinivasa (Reference 8). If the pressure in the pulse is scaled by the same reflection factor of 1.48, the midpoint pressure variation shown in the top left panel of Figure 6 is obtained. The present calculations are also compared with finite-difference calculations by the HULL* method. The agreement between the two predictions is excellent.

Roof: It can be assumed that as the shock clears the windward face, the shock undergoes a diffraction which brings the overpressure back to the freefield value. However, by the time the freefield blast reaches the location of the midpoint of the roof, it has decayed to 540 psi. The calculated pressure variation is shown compared with the numerical calculations by the HULL code in Figure 6 (upper right panel). The calculated peak pressures do not agree everywhere, but this shouldn't be surprising since the techniques we used are approximate. Our estimates, however, appear to be on the conservative side as intended.

Leeward Face: On the leeward face, the shock undergoes a further diffraction, and the decrease in overpressure is again evaluated by Whitham's method. The free field peak overpressure at midpoint of the

*HULL results are supplied by AFWL/DYM (Reference 9).

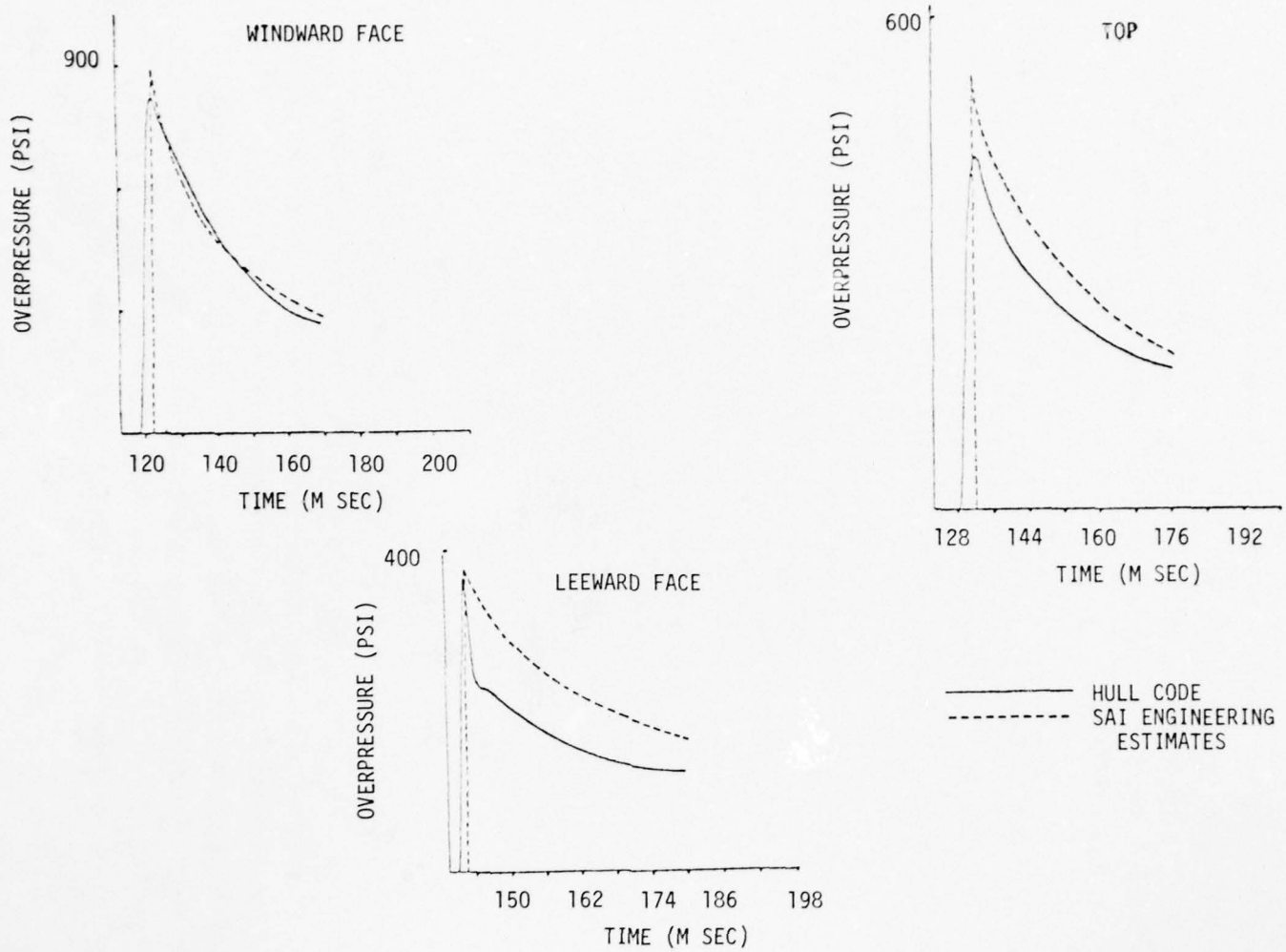

Figure 6. Shelter loading for side-on incidence of classical waveform

face has now decayed to 480 psi; the diffracted peak overpressure is found to be 380 psi. Peak overpressures calculated by this method (Figure 6) agree well with the HULL calculation. However, the HULL calculations show an abrupt fall in pressure immediately behind the shock front. This may be attributed to the generation of vortices at the top corner of the face.

2.4 END-ON INCIDENCE

Figure 4 shows an idealized shock reflection at the shelter for end-on incidence. The loading on the separate faces is determined as follows.

Windward Face: The quasi-steady method (outlined in Reference 6) is applied to calculate the average-pressure loading on the vertical door. First, the reflection factor for a head on reflection for a shock of overpressure 600 psi is found to be 7.4. This gives a reflected peak pressure of 4440 psi. Next, the speed of the rarefaction wave which propagates from the top of the door to the bottom and back up again is found to be 4620 ft/s. This gives a propagation time of 15ms, during which the average pressure decays linearly. After 15 ms, the average pressure is given by:

$$P_{av} = P(t) + C_d\, Q(t) \qquad (5)$$

where $P(t)$ and $Q(t)$ are the incident static pressure and the incident dynamic pressure, and C_d is a drag coefficient. The value of C_d is usually determined from experiment. However, no such data are available at 600 psi incident pressure, and the present value of 1.8 for C_d is obtained by extrapolating known values at lower pressures (100 and 300 psi). The variation of average pressure with time is shown at the top left panel of Figure 7 along with the HULL prediction. The HULL calculation is not achieving the full reflected value of pressure, because

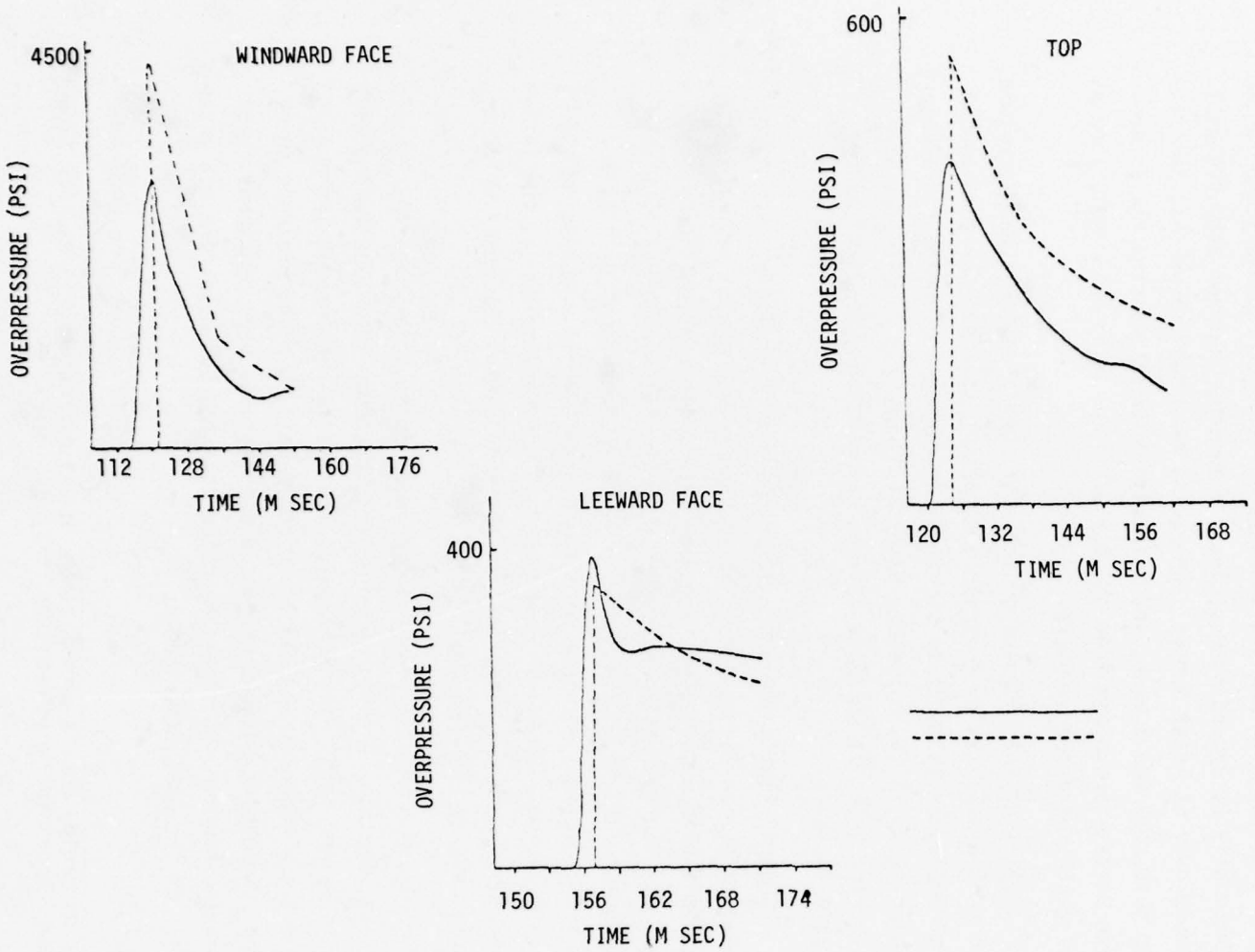

Figure 7. Shelter loading for end-on incidence of classical waveform

of the smearing of the shock due to the finite difference scheme. Since the zone size was 1 m, and the shock speed is about 2 m/msec, and further, the shock will be spread over at least 6 zones*, the peak pressure will be spread over at least 3 msec. One notes from the figure that the rise to the HULL peak was 6 msec, and this rise time allows time for a rarefaction wave to propagate from the top of the face to the middle thereby reducing the reflected pressure.

Roof: At the midpoint on the roof, the free field peak pressure decays to 550 psi. It is reasonable to assume that the pressure at the foot of the shock is equal to the free field pressure, hence the pressure variation shown in the top right panel of Figure 7 is obtained. Here again, there exist differences between our earlier estimates and the HULL calculations.

Leeward Side: The shock undergoes a diffraction at the top of the leeward side. The change in peak pressure was again evaluated from Whitham's method. Given that the peak free field pressure decays to 450 psi at the midpoint location on the face, the peak pressure behind the diffracted shock should be 350 psi. The lower panel of Figure 7 shows the calculated pressure variations with time as compared to the HULL calculations. Similar to the case of side-on incidence, the latter calculations exhibit a sharp fall in pressure behind the shock which is not predicted by the empirical method.

Figure 8 shows a comparison between calculations and the Dynamic Air Blast Simulator (DABS), experiments (Reference 10). The left panel shows the experimental incident wave, the middle panel shows the pressure on the windward side, and the right panel shows the pressure on the top. Agreement between predicted and measured peak pressures seems reasonable, however, it should be noted that the estimates did not agree with all of the DABS experiments.

*Shock spreading occurs over 6 zones in one dimension. It usually occurs over more zones in two dimensions.

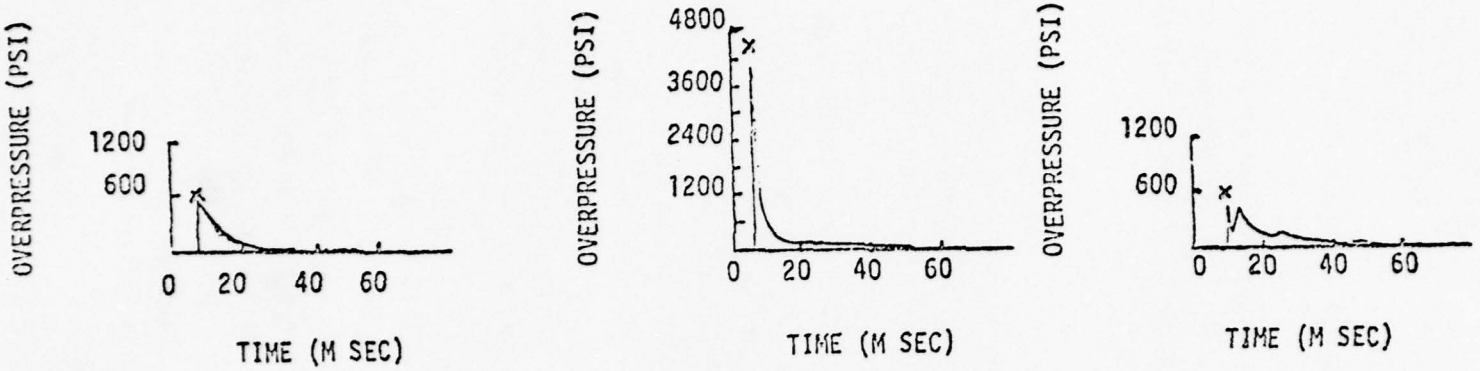

NOTE: SYMBOL (X) DENOTES CALCULATED VALUE

Figure 8. Comparison with DABS experiment for end-on incidence (Reference 10)

SECTION 3
AIR BLAST LOADS FOR THE PRECURSOR WAVEFORM

This section presents engineering estimates of the air blast loads on the M-X above ground shelter resulting from the incidence of a precursed waveform. This section is structured the same as Section 2.

3.1 DESCRIPTION OF WAVEFORM

The precursor waveform used in the present calculations (Figure 9) is obtained by cube root scaling of an empirical formulation provided by J. Keefer of BRL (Reference 11). This scaling and the fact that Keefer's data are for shots at various heights of burst (no surface bursts) makes the waveform and overpressure uncertain. Furthermore it has been assumed that the dynamic pressure can be obtained by use of the Rankine-Hugoniot relationships as if the wave were a one-dimensional shock with a peak overpressure corresponding to the scaled overpressure from Keefer's data. Recent AFWL calculations have demonstrated that this assumption is generally not warranted (References 12 and 13), and therefore the loads predicted herein may be conservative. In any event, any additional contribution due to the enhanced dynamic pressure could be straightforwardly added. An important point to remember, however, is no data currently exist as to how large the enhancement factor should be.

Since the following calculations have been based primarily (excepting the case of the vertical door) upon the value of the peak overpressure and not on the shape of the pulse, the results are insensitive to the waveform, and except for possible significant enhancement of the dynamic pressure give a reasonable guideline for the precursor loading on the shelter in the absence of dust. Dust loading may further increase the effect of the dynamic pressure, but there exists no quantitative data available to assess the dust contribution.

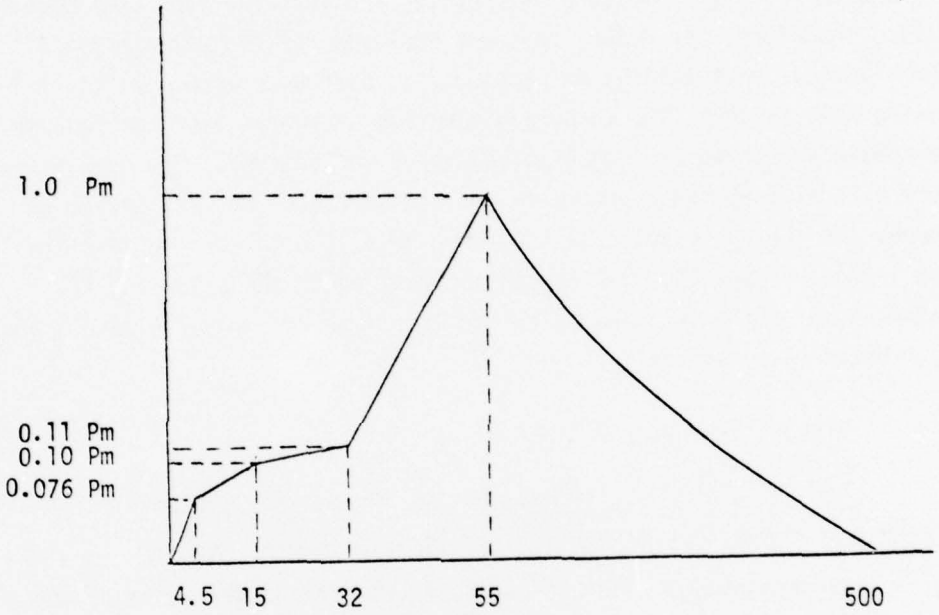

NOTE: PM = 600 psi nominal

Figure 9. Scaled precursor waveform used for estimated loads.

3.2 METHOD OF ANALYSIS

As in the case of the classical wave interaction with the shelter, a quasi-steady state approach to the calculation of the load on the shelter is not reasonable, except for the vertical door (see Section 2.2). Therefore, the method that was employed for the calculation of the classical wave loading in Section 2 is used here also. In the following calculations, the shape and duration of the waveform are assumed to remain unaltered as the pulse undergoes reflections. The peak pressure is scaled by the appropriate reflection factor at each change of shape, and the whole pulse is scaled by that same factor. Unlike the quasi-steady approach, the present approach does not allow for the attenuation of the oncoming pulse due to reflected expansion waves, and is, therefore conservative.

3.3 SIDE-ON INCIDENCE

The calculation of the reflection factors for the peak overpressure proceeds in a manner similar to that in Section 2.3.

Windward Side: The reflection factor for a shock wave of 600 psi is 1.24. In this case, the safety factor of 20 percent is not included since the figure is on the conservative side. The top left panel of Figure 10 gives the pressure variation with time at the midpoint location on the face.

Top: The free-field peak overpressure in the pulse is assumed to decay with distance as in the case of the classical waveform, and the pressure on the roof of the structure is assumed to be the same as that of the free field at 540 psi. The top right panel in Figure 10 shows the pressure-time history at the midpoint location on the face.

Leeward Face: The lower panel in Figure 10 shows the variations of pressure with time at the midpoint location on the face. The peak overpressure is 380 psi.

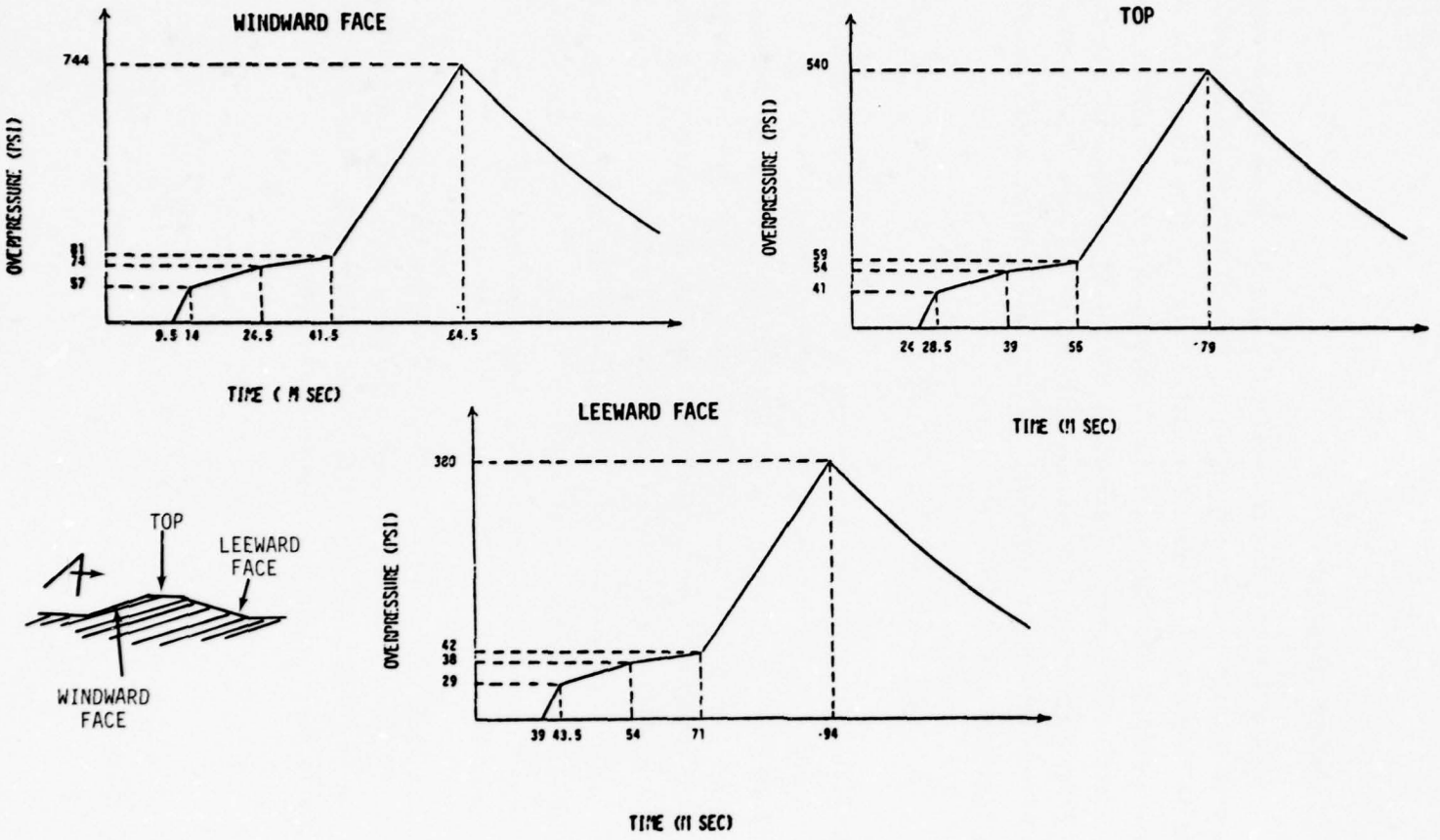

Figure 10. Shelter loading for side-on incidence of precursor waveform

3.4 END-ON INCIDENCE

Windward Face: The calculation of the average-pressure load on this vertical face is carried out in accordance with the recommendation given in Reference 6. First it is noted that the rise time of the overpressure exceeds the time taken for an expansion fan to traverse the front face. Therefore, no reflection process is assumed, and the pressure rises linearly to the maximum value in a time equal to the rise time of the incident overpressure. After attaining the peak, the pressure then varies according to:

$$P_{av} = P(t) + C_d\, Q(t) \qquad (6)$$

where $Q(t)$ is the dynamic pressure and C_d is the drag coefficient for which a value of 1.8 is assumed. The maximum pressure occurs at $t = 55$ ms (the rise time of the incident pulse). For an overpressure of 600 psi, the dynamic pressure is 1270 psi. Hence, the maximum value of P_{av} is 2890 psi. The top left panel in Figure 11 shows the average pressure variation with time on the windward face.

Top: The pressure at the midpoint on the roof is determined in the same way as for the classical shock loading. That is, the pressure waveform is assumed to be the same as the free-field and is shown in the top right panel in Figure 11.

Leeward Face: The free-field peak pressure at the midpoint location is 450 psi. The peak pressure behind the diffracted shock at that location is found to be 350 psi by the Whitham method. The pressure history is shown in the lower panel of Figure 11.

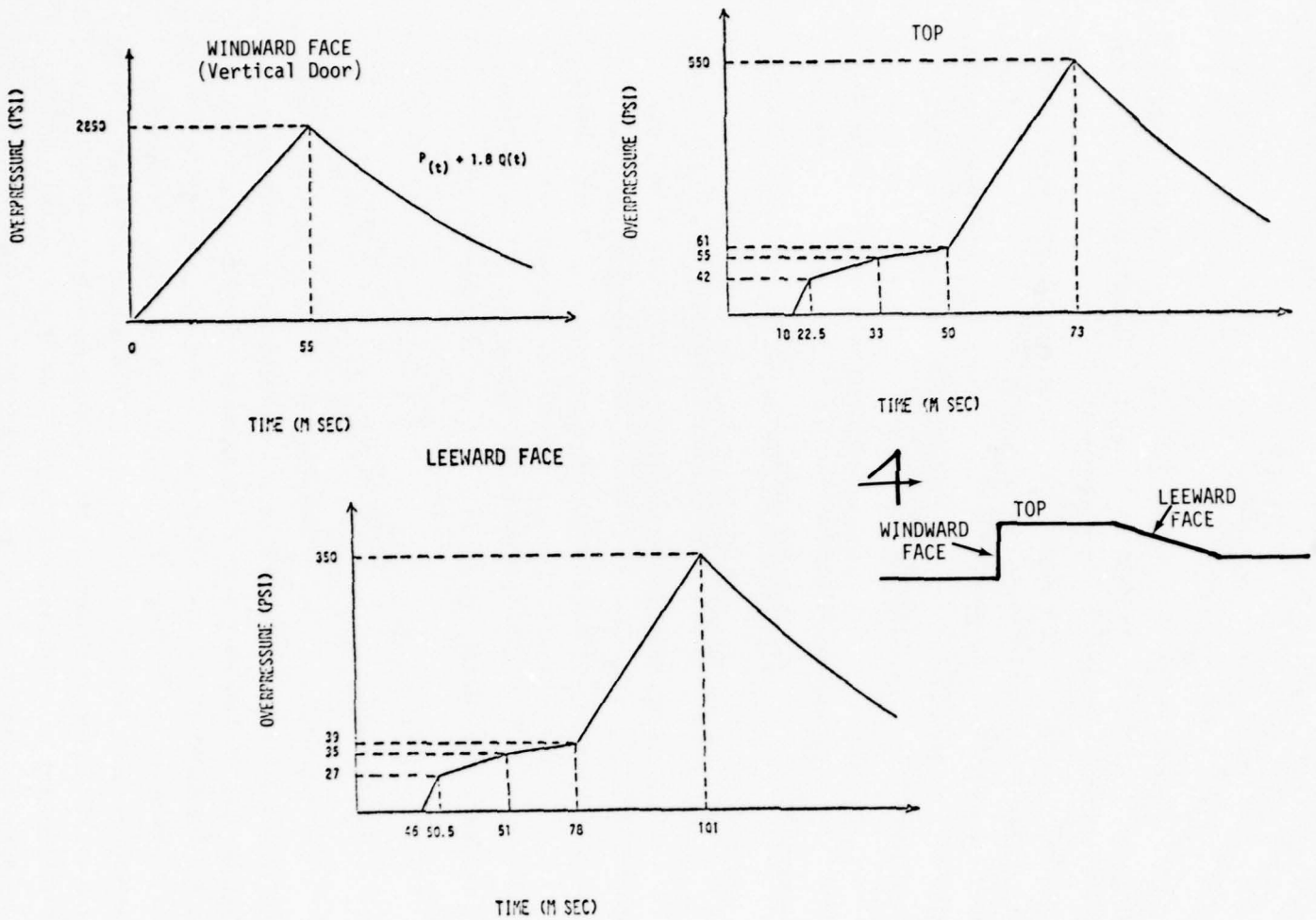

Figure 11. Shelter loading for end-on incidence of precursor waveform.

SECTION 4
NUCLEAR DATA BASE

This section is the first of four that pertain to the investigation of the influence of dust on air blast. In this section we repeat some of the observations that had been made earlier by SAI in a study of late time dust lofting (Reference 14). These observations were reviewed during this effort to determine their relevance to the influence of dust on air blast. The observations have been summarized; the reader should refer back to the reference for a more detailed account. The first seven subsections summarize the various pertinent nuclear test operations. Section 4.8 consists of a list of precursed and non-precursed shots. Finally, Section 4.9 summarizes the conclusions drawn from this review pertinent to the air blast work.

4.1 SANDSTONE AND GREENHOUSE

In the seven tower shots of operations SANDSTONE (1948) and GREENHOUSE (1951) conducted at Eniwetok, there was clear evidence of blast wave anomalies in the form of lower overpressure, faster arrival, and larger dynamic pressure than was expected on the basis of ideal blast wave theory for near-surface bursts (Reference 15). In addition, the pressure-time records were highly abnormal compared to the ideal case.

4.2 BUSTER-JANGLE

In the four air drops of BUSTER-JANGLE (1951), there were great discrepancies from the ideal HOB curves (Reference 16). Furthermore, large amounts of dust were seen to be produced before shock arrival, and the transport of the dust after shock arrival was much different when a precursor was present. For example, consider the differences between the Baker and Charlie shots. On BUSTER BAKER, 3.5 kt at 1118 ft, there was no precursor evident in the pressure records. Preshock dust was evident out to ground radii of 1890 ft, where the preshock dust layer had a measured rise velocity of about 80 ft/sec (Reference 17).

From the ground level technical photography, the shape of the dust layer after the shock had passed, but before the fireball began to rise, was that of a mound or cone perhaps 100 ft. high at the center, and extending in radius to about 2000 ft. However, on BUSTER CHARLIE, 14 kt at 1132 ft, the situation was different. The air pressure records showed severe perturbations from what would have been expected for a blast over an ideal surface. Peak overpressure was considerably lower than free air overpressure out to about 10 psi. The precursor propagated faster at first, then slowed rather abruptly and finally approached the ideal case. Peak dynamic pressure was a factor of 2 or 3 higher at first, and finally approached the ideal value. Finally, the pressure-time records showed an extended "front porch" on the wave form, and a peak pressure later.

The dust layer history on BUSTER CHARLIE was also significantly different. Before shock arrival, preshock dust was evident as in BUSTER BAKER. Behind the shock wave, a wall of dust rose very quickly and was carried out radially with the shock, giving the appearance of an expanding disc seen edge-on. The disc was markedly different from the more conical dust layer seen on BUSTER BAKER.

4.3 TUMBLER-SNAPPER

As a result of the military requirement for accurate assessment of ground level damage as a function of range and HOB, the four air drops of operation TUMBLER-SNAPPER (1952) were instrumented to provide data on the blast and dust environment for precursor shots. The experiments included overpressure waveforms, dynamic pressure, time of arrival, thermal pulse, preshock air temperatures, dust densities, and technical photography of the shock wave and the dust layer. Instrumentation for preshock air temperatures was included because the higher shock propagation velocity seen on BUSTER-JANGLE could be understood more easily if the existence of a layer of heated air near the ground could be established.

Preshock air temperatures on operation TUMBLER were measured at several ranges by three groups: NRDL (Naval Radiological Defense Laboratory) fielded aspirated thermocouples at several ground ranges and heights (References 18 and 19); NEL (Naval Electronics Laboratory) made sonic velocity measurements and thus, indirectly, air temperature measurements (References 20 and 21); and NRL (Naval Research Laboratory) conducted measurements of air temperature before shock arrival with aspirated wire tension gauges (Reference 22). The results of these direct preshock air temperature measurements were inconsistent: the three independent methods showed different measured preshock air temperature histories and different variations with range and height above ground surface. This disagreement was the cause of considerable confusion at the time, and is discussed at length in DASA 1200 (Reference 23). Although it was not possible from these measurements to determine an empirical preshock air temperature curve, the large number of measurements taken nevertheless indicate with a high degree of confidence that on TUMBLER 4 (DOG), 19 kt at 1040 ft, preshock air temperatures rose more than $100^{o}C$ out to ranges corresponding to normal thermal radiation fluences of about 15 cal/cm^2 and overpressure of about 8 psi (References 21 and 24). On TUMBLER 1-3 (ABLE, BAKER, and CHARLIE) significant air temperature rises were seen also, but due to lower yields or higher HOB, these air temperatures occurred at lower blast overpressures.

It can be concluded from the TUMBLER measurements that the heating of the air is due to the interaction of thermal radiation with the surface, followed by some process that transfers heat to the air above.

In the blast-wave measurements, an immediate correlation can be seen. The blast waves for TUMBLER 1-3 encountered the hot air layer only at low overpressure, but in TUMBLER 4, because of the yield and HOB, the blast wave encountered the hot layer at considerably higher

overpressures (Reference 25). The overpressure waveforms and times of arrival showed no precursor effects for the first three shots, but a strong precursor developed on TUMBLER 4 (Reference 24). This indicated a probable relation between preshock air temperatures and the existence of a precursor.

The technical photography on operation TUMBLER confirmed the existence of a precursor effect as seen in the overpressure measurements. An excellent example is shown on the frontispiece of Reference 24. A more detailed photograph, reproduced in Reference 26 shows the TUMBLER 4 blast wave at 1345 ft from GZ. The incident and reflected waves are clearly seen, along with a precursor extending out several hundred feet. A layer of preshock dust perhaps 10 ft high is visible, and the foot of the precursor can be seen extending into this layer. Another photograph of the preshock dust is given on p. 55 of Reference 24. Immediately after the foot of the precursor has passed, the dust can be seen to rise rapidly in a "rooster tail" effect, to heights of hundreds of feet. There is thus evidence that the TUMBLER 4 precursor consisted of a blast wave running ahead in a layer of preheated air loaded with dust raised before shock arrival.

Measurements of preshock dust density and particle size were included in operation TUMBLER. These indicated, on all four shots, concentrations of preshock dust, a factor of 10 to 100 over background dust densities (Reference 27). Furthermore, the measured particle size of the preshock dust was about the same as that of the background dust.

On TUMBLER 4 the technical photography showed that the precursor formed after the arrival of the shock at GZ, the first photographs indicating a precursor at 500 ft ground range. The precursor was seen out to 2100 ft ground range, and existed for about 700 msec. The height at which the precursor front was seen to join the incident shock wave increased to a maximum of 350 ft and then decreased (Reference 23).

The most dramatic finding in the TUMBLER 4 technical photography was the rapid growth of an optically dense dust cloud immediately after precursor arrival. This copious dust layer was seen only on TUMBLER 4, and grew to heights of several hundred feet.

Later in time the measured overpressure waveform begins to revert to that of an ideal blast wave. The dust that travels at first seemingly attached to the precursor wave eventually becomes detached and lags behind. At still later times, the dust layer comes to a halt, at a height of several hundred feet, with indications that the dust is highest at the periphery and lower in toward GZ, giving the appearance of a hemitoroid. This is fairly evident in the documentary photography (Reference 24). It is not evident in the technical photography because of the location of the cameras at ground level.

The existence of the precursor effect and its relation to dust production, originally noted in the BUSTER-JANGLE data, were confirmed during TUMBLER-SNAPPER and the data base was greatly expanded. Besides the very good data on overpressure time history mentioned above, high quality thermal pulse data were obtained (Reference 28). Technical photography of the shock wave and dust layer was extensive and of high quality (References 23, 24 and 26). Direct measurements of air temperature near the ground before shock arrival were not of as high quality as the data just mentioned, but when compared with indirect measurements based on shock propagation in heated layers, it could be concluded that the precursor was thermal in origin, and a result of certain complex flow patterns that arise when a shock runs ahead into a heated layer (References 18-25). Data on dust density in the air before shock arrival were not of consistent high quality, but the evidence is strong that dust densities at least a factor of 10 higher than background dust densities accompanied the formation of the heated air layer (Reference 27).

4.4 UPSHOT-KNOTHOLE

The pronounced precursor effects seen on operation TUMBLER-SNAPPER, and their potential influence on military effectiveness of air drops, led to an extensive experimental program on operation UPSHOT-KNOTHOLE (1953). Of the 11 shots, 4 were especially well instrumented and photographed: UK 1 (ANNIE), UK 9 (ENCORE), UK 10 (GRABLE), and UK 11 (CLIMAX).* All of these shots had strong precursors except UK 9.

Instrumentation on this series included air blast (References 29 and 30), dynamic pressure (Reference 31), overpressure wave forms (Reference 32), and preshock air temperature from sound speed (Reference 21). In particular, a discussion of the relation between Mach reflection and the "knee" in the overpressure-ground range plot is given in Reference 33. Preshock air temperature measurements were made by SRI, NRDL, and NEL on GRABLE and CLIMAX (Reference 33).

The technical photography on UPSHOT-KNOTHOLE is especially good, and is much more convincing than any analysis of the data; after looking at these photographs it is difficult to avoid the conclusion that production of a large dust pedestal is uniquely a precursor effect.

On UK 1 (ANNIE, 16 kt at 300 ft) a strong precursor was observed. At the same time, thermal radiation effects were more intense than expected (Reference 33). Very good determinations were made of shock time of arrival and fireball radius (Reference 29), although the history and characteristics of the ground dust layer were not fully documented on this shot.

On UK 9 (ENCORE, 27 kt at 2425 ft) no precursor was observed in the time-of-arrival or overpressure-range data, but there was evidence of Mach stem formation earlier than had been expected (Reference 29). Good time-of-arrival and fireball radius measurements were reported (Reference 29). Both of these quantities agreed, when scaled,

*UPSHOT-KNOTHOLE 8 (HARRY) was detonated 11 days after UPSHOT-KNOTHOLE 9. This sequencing has caused some confusion in the literature.

to the results from TUMBLER-ABLE, which was at the same scaled HOB (Reference 33). The overpressure waveforms likewise showed ideal behavior with no sign of a precursor (Reference 33).

The technical photography from ENCORE provided excellent data on the behavior of the dust layer in the absence of a precursor. Reference 29 contains excellent shock photography at 700, 2800, and 4000 ft. The shock was nearly ideal in shape, and the Mach reflection was clearly seen.

It is important to note here that behind this shock wave no dust layer is observed to rise; at much later times, when negative phase winds begin, some dust is observed to be swept back toward the stem, but absolutely no evidence was seen in these photographs for the abrupt rise of the dust pedestal behind the shock front, which is so typical of precursor shots. Thus, ENCORE serves as a non-precursor example for establishing the correlation between the precursor and dust lofting.

UK 10 (GRABLE, 15 kt at 524 ft) provided good evidence for dust behavior in a precursor shot. Very strong precursor behavior was seen on the time-of-arrival curve and on the overpressure time history (References 29 and 33). Shock photography confirmed the existence of a precursor; the Mach stem and precursor front can be very clearly distinguished in these photographs (Reference 29). Immediately behind the precursor the dust layer can be seen to rise very rapidly, with rise velocities of hundreds of feet per second (Reference 29). The precursor was seen to develop at a range of about 200 ft, and by 800 ft, several fronts could be seen; some of these were apparently reflected waves.

At later times the precursor flow was seen to be still well established out to 1900 ft. The top of the Mach stem is visible, along with the precursor front and attendant dust. At the latest time available in the technical photography, the dust pedestal was 100 ft high at a range of 1300 ft (Reference 33).

The photographs from GRABLE are perhaps the best available for illustrating dust lofting behind a precursor. The motion picture film are reported in References 23 and 29. The rise velocity of the dust front at 1200 ft is 1000 fps and a rapid rise of the dust to 250 ft was observed. The dust pedestal finally extended to 2700 ft (Reference 23).

The preshock air temperature measurements on GRABLE were made to support development of a theoretical model for the precursor. Direct measurements by NRDL are reported (Reference 33), and indirect measurements, from the orientation of the precursor wave front, are discussed in Reference 29. These determinations of preshock air temperature are not consistent with each other, as was discussed in Section 4.3.

UPSHOT-KNOTHOLE 11 (CLIMAX, 61 kt at 1334 ft) confirmed the conclusions from GRABLE. The time-of-arrival curves reported in Reference 29 showed strong precursor behavior. Likewise, the overpressure-radius and pressure-time histories showed strong precursor effects as did the technical photography (Reference 33). The precursor was observed to persist out to 3400 ft (about 7 psi) in agreement with the results on TUMBLER-SNAPPER 4 and GRABLE (Reference 33). At this range, several effects were noted on CLIMAX, and were also seen on re-examination of TUMBLER-SNAPPER 4, ANNIE, GRABLE, and several other shots. First, the end of the precursor "front porch" on the pressure-time records corresponded to the "knee," or change in slope of the overpressure-range curve; both occurring at a range of 3400 ft. Also the photographic appearance of the blast wave changed at this same point from an obvious precursor shape to that of an ideal wave. Finally, the dust pedestal, which had been thrown up behind the precursor wave, suddenly at this point began to lag behind the shock front for the first time, and eventually came to rest at 4200 ft (Reference 33). CLIMAX was historically the most convincing demonstration of the nature of the precursor, its primary effects, and its role in raising dust.

CLIMAX was detonated at Area T-7, Yucca Flats, while GRABLE was detonated over Frenchman Flats. These surfaces differ in some respects, providing an indication of the role of the ground surface in precursor formation and dust production. Preshock air temperatures were recorded with the NRDL thermocouple gauge (Reference 33). The troubling lack of consistency between various preshock air temperature measurements, mentioned before, is summarized in DASA 1200, Reference 23. However, the air temperature measurements from GRABLE, CLIMAX, and DOG (UK 10, 11, and TS-4) showed less erratic behavior in the individual records and were more consistent among themselves than were most of the other temperature records discussed in DASA 1200 (Reference 23). In particular, the NRDL direct thermocouple measurements, reported in Reference 33, and the indirect air temperature measurements from the precursor angle reported in Reference 29 are in good agreement for these shots.

4.5 TEAPOT

There were 13 air or tower shots on operation TEAPOT (1955). All were at Area T-3 or T-7 of Yucca Flats, except TEAPOT 12 (MET) which was over a somewhat different soil at Frenchman Flats. A major concern in the planning and instrumentation of TEAPOT was to extend the data base on the blast precursor (Reference 33). This program was realized mostly through extensive photography on most shots, through thermal flux measurements, and especially through an extensive experimental program on TEAPOT 12 (MET).

The other shots were not as well instrumented. Very good photography exists on TEAPOT 1 (WASP, 1 kt at 762 ft), TEAPOT 3 (TESLA, 7 kt at 300 ft), and TEAPOT 6 (BEE, 8 kt at 500 ft). This photography shows clear precursor behavior on TESLA and BEE, along with the characteristic dust pedestal formation immediately behind the precursor (Reference 34). WASP has no precursor, and the technical photography confirms that no dust pedestal was formed (Reference 34).

TEAPOT 4 (TURK, 43 kt at 500 ft) was not well covered in the technical photography (Reference 34). However, reports that strong precursor evidence was seen in the photography and overpressure records can be found in Reference 23. Furthermore, other technical and documentary photography show an especially pronounced dust pedestal on TURK. The same is true of TEAPOT 9 (WASP PRIME, 3 kt at 740 ft).

TEAPOT 5 (HORNET, 4 kt at 300 ft) was noteworthy also in that a smoke layer was generated over one of the blast lines prior to detonation (Reference 35). A similar experiment, reported in Reference 23 was done on UK 10. On both of these shots, a precursor was observed on the pressure records along the blast lines that had no smoke, and no precursor was observed along the smoke-covered surface.

Of the remaining TEAPOT shots, only TEAPOT 12 (MET, 22 kt at 400 ft) was extensively studied. TEAPOT 7 (ESS) was a buried burst, and TEAPOT 10 (HA) was a high-altitude burst. The data from TEAPOT 8, 11, 13 and 14 had not been reduced at the time the test reports were written and thus were not reviewed.

TEAPOT 12 was perhaps the single most instrumented shot of any U.S. test. Table 1 is a partial list of the instrumentation on this shot (Reference 35). Surface gauges were placed from 750 ft out; gauges at 3 and 10 ft heights were placed on hardened towers starting at 1250 ft. These towers were designed to allow measurements to be made through the passage of the shock wave.

Table 1. TEAPOT 12 instrumentation

TEAPOT 12 (MET) 22 kt at 400 ft
Separate blast lines over water, asphalt, and desert
Baffled Wiancko overpressure at various heights
Pitot-static dynamic pressure
Dust flow pitch [arc tan (u_y/u_x)]
Blast photography
GREG gauge total dynamic pressure
SNOB gauge total dynamic pressure of air only
Dust density by beta densitometer and snap sampler
Preshock air temperatures by NRDL
Preshock sound velocity by NEL
Test plots of concrete, wood, ivy, and fir trees
Drag measurements on spheres placed on surface

Times of blast arrival for TEAPOT 12 were shortest over the asphalt line and increased over desert and water. Even the water line arrival times were slightly less than ideal, indicating a weak precursor over water (Reference 35).* This is the only mention of a precursor over water that was found in the NTS and PPG data reviewed. The time-of-arrival curves clearly indicate the existence and extent of precursor behavior (Reference 35). "Second arrival," i.e., the arrival time of the maximum overpressure, was carefully studied to see if it corresponded to the arrival of the main shock. The conclusion is well documented that the "main shock," that is, the shock that would be expected at the point of intersection between the incident and reflected waves if the blast were ideal, simply does not exist (Reference 35). There is no evidence, either on TEAPOT 12 or on any other shot studied, that a "main shock" exists at the ground on precursor shots.

*It is possible this could have resulted from 3-dimensional effects affecting the measurements over the water line.

Over the asphalt blast line, the precursor was formed close in (Reference 35). A dense wave of dust was rapidly thrown up behind the precursor front and carried outward with the precursor (Reference 35). The arrival of this dust front at the 3-foot and 10-foot gauges corresponded to the "main shock," that is, the second peak, in dynamic pressure (Reference 35). The precursor developed between 1250 and 2000 ft and was fairly constant to 3000 ft (Reference 35). The dust cloud over asphalt was hundreds of feet high by 2500 ft. The instrumentation towers, usually 50 ft high, were blackened on the side facing GZ (Reference 35).

Over the desert line, a surface of more direct tactical interest, the behavior was less pronounced. The precursor developed later and was still developing at 2000 to 3000 ft, where the asphalt precursor was already well developed (Reference 35). This was attributed to the more intense interaction of the thermal pulse with the asphalt surface that would be expected on a very absorbing black surface.* Over the desert line, the characteristic precursor dust layer was produced. It swept outward, seemingly at the same velocity as the precursor wave, to 1900 ft. Here the dust began to lag behind the precursor, with the dust front making an angle of 20^{o} to the horizontal, until it eventually stopped at 3100 ft (Reference 35). The precursor itself was detectable out to 6 psi (Reference 35). The waveform returned to ideal shape at 4000 ft (Reference 35).

Dust density in the advancing dust pedestal was measured at several ground ranges (Reference 36). At 2000 ft, the dust front just began to separate and lag behind the shock. In the interval from 40 to 360 msec after shock arrival, the ratio of dust density to total density (dust and air) rose from 0.12 to 0.75 at a height of 3 ft as shown in Figure 12. A single measurement at 10 ft gave 0.42 (Reference 35). No measurements are available at higher stations. The available data taken from Reference 35 are shown in Table 2.

*Outgassing of some gas of different gamma than air could also contribute to the formation of a precursor wave.

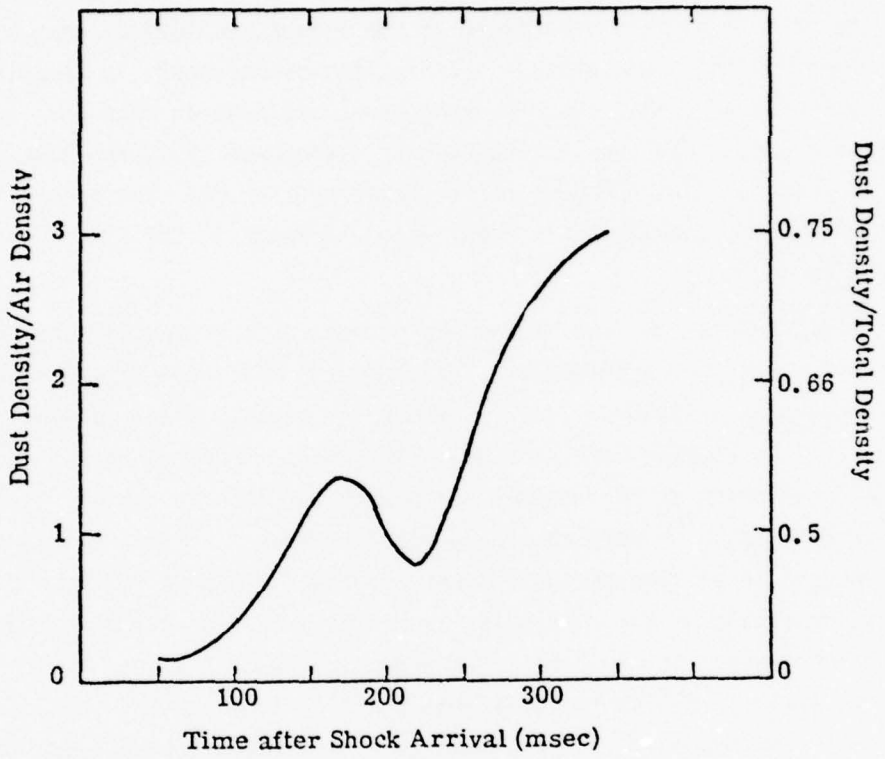

Figure 12. TEAPOT 12 dust densities.

Table 2. TEAPOT 12 dust densities

GROUND RANGE (ft)	HEIGHT 3 ft	10 ft
2000	0.12 - 0.75	0.43
2500	0.05 - 0.19	0.06 - 0.11
3000	0.04 - 0.05	0

NOTE: Source: WT 1153, Reference . Tabulated values are dust density over total density.

A shortcoming in the beta densitometer data is the failure of the total density measurements. Due to the experimental configuration, the measured quantity was relative density, as in Figure 12. A total density experiment for calibration failed because of gamma ray background (Reference 35).

On UPSHOT-KNOTHOLE the origin of the precursor was established with a good degree of certainty to be a thermal layer near the ground. For this reason, TEAPOT 12 was instrumented to measure the preshock air temperatures.

The NEL preshock sound velocity measurements were believed to be better on TEAPOT 12 than on any other shot (Reference 35). Nevertheless, certain anomalies have not been explained. First, the sound velocity records show little difference over water, asphalt, or desert. Furthermore, the velocities were much lower than those observed on TUMBLER and UPSHOT-KNOTHOLE (Reference 37). Post shot equipment checks showed no environmental degradation that would lead to a conclusion that the gauges had been damaged during the measurements.

The NRDL thermocouple air temperature measurements were not entirely satisfactory either. The records were erratic and dropped to ambient before the shock arrived (Reference 35). It was conjectured at the time that these records could be showing the effect of extreme turbulence from convective flow. A few of the NRDL measurements on TEAPOT 4

(TURK, 43 kt at 500 ft) were significantly better (Reference). They were more consistent and showed less fluctuation before shock arrival. TURK was detonated at Area T-7 of Yucca Flats, whereas TEAPOT 12 was at Frenchman Flats. Also TEAPOT 12 was detonated in the daytime, whereas TURK was at night. It is possible that evaporation of dew made the MET soil drier than the TURK soil. These discrepancies have never been resolved.

The shock photography is particularly good on TEAPOT 12 (References 34, 38 and 39). The attachment of the dust front to the front of the precursor is evident, as is the location and orientation of the precursor front.

4.6 REDWING

Operation REDWING (1956) was conducted at PPG. Since from the NTS experience, no precursors or only very weak precursors were expected over water, no instrumentation for preshock air temperatures had been reported.

Nevertheless, evidence of precursor behavior was clearly seen on two shots in the overpressure records and the technical photograph (Reference 15, 40-43), but the precursors were weak and appeared only over land. These shots were ZUNI and LACROSSE, and are noteworthy in that they provide the first evidence of precursor behavior for surface blasts.

On LACROSSE non-ideal overpressure and dynamic pressure time histories were observed; arrival time and peak overpressure were close to ideal (Reference 23). Little dust was seen to be raised over the island. On ZUNI all blast data showed non ideal behavior and a clear precursor is seen in the technical photography (Reference 23). No data were found on dust production in ZUNI.

4.7 PLUMBBOB

Precursor behavior was confirmed on at least 7 shots from operation PLUMBBOB (1957). The best known of these shots is PLUMBBOB 6 (PRISCILLA, 37 kt at 700 ft). The precursor is evident in the air blast records and is quite strong (References 44 and 45).

A history of the PRISCILLA precursor is given in DASA 1200 (Reference 23). Further preshock air temperature measurements were made on this shot but were not of high quality (Reference 2).

4.8 LIST OF PRECURSOR AND NON-PRECURSOR SHOTS

In the preceding sections the principal features of the nuclear blast precursor phenomenon have been described for NTS shots at various HOBs. Tables 3 and 4 list in chronological order all the shots mentioned in DASA 1200 as definitely having a precursor or definitely not (Reference 23). A similar list occurs in DASA 1141 (Reference 15).

The existence of a precursor has been established on the surface bursts BRAVO, LACROSSE, ZUNI, and SMALL BOY (Reference 23), but not on JANGLE S, MIKE, KOON, or CACTUS. On all PPG shots the non-existence of precursors has been established over water only. There exist no data that would imply that precursor formation is rare for land surface bursts. Criteria based on yield and HOB have been fairly successful in predicting precursor existence; that of Shelton, as discussed in DASA 1200, is particularly successful (Reference 15).

4.9 SUMMARY OF CONCLUSION FROM NTS DATA RELATED TO AIR BLAST

The earlier sections have pointed to various nuclear data that can be found in the many references made. Pertinent to the air blast efforts, we feel that the following conclusions are warranted based on what has been demonstrated in the earlier parts of this section.

Table 3. Established precursor and non-precursor shots: TRINITY through TEAPOT

PRECURSOR SHOTS			NON-PRECURSOR SHOTS		
NAME	YIELD(Kt)	HOB(ft)	NAME	YIELD(Kt)	HOB(ft)
TRINITY	(19)	(100)	CROSSROADS ABLE		(520)
GREENHOUSE DOG		(300)	BUSTER ABLE	(<0.1)	(100)
EASY	(47)	(300)	BAKER	(3.5)	(1118)
GEORGE		(200)	JANGLE S	(1.2)	(0)
BUSTER CHARLIE	(14)	(1132)	TUMBLER ABLE	(1)	(793)
EASY	(31)	(1314)	BAKER	(1)	(1050)
TUMBLER DOG	(19)	(1040)	CHARLIE	(31)	(3447)
IVY KING		(1480)[a]	IVY MIKE	(1040)	(0)
UK 1	(16)	(300)	UK 4	(11)	(6020)[b]
10	(15)	(524)	9	(27)	(2425)[b]
11	(61)	(1334)	CASTLE ROMEO		(0)
CASTLE BRAVO	(1500)	(0)	KOON	(~100)	(0)[c]
TEAPOT MOTH	(2)	(300)	YANKEE		(0)
TESLA	(7)	(300)	NECTAR		(0)
TURK	(43)	(500)	TEAPOT WASP	(1)	(762)
HORNET	(4)	(300)			
BEE	(8)	(500)			
APPLE-1	(14)	(500)			
WASP PRIME	(3)	(740)			
POST	(2)	(300)			
MET	(22)	(400)			
APPLE-2	(29)	(500)			
ZUCCHINI	(28)	(500)			

NOTES:

(a) Over land but not over water
(b) ENCORE
(c) Shot in rain

Table 4. Established precursor and non-precursor shots: REDWING through 1962

PRECURSOR SHOTS			NON-PRECURSOR SHOTS		
NAME	YIELD(Kt)	HOB(ft)	NAME	YIELD(kt)	HOB(ft)
REDWING LACROSSE		(0)	REDWING CHEROKEE		(320)
ZUNI		(0)	HURON		(0)
PLUMBBOB WILSON	(10)	(500)	INCA		(0)
PRISCILLA	(37)	(700)	MOHAWK		(0)
HOOD	(74)	(1500)	PLUMBBOB FRANKLIN	(0.14)	(300)
OWENS	(9.7)	(500)	KEPLER	(10)	(500)[a]
SMOKY	(44)	(700)	SHASTA	(17)	(500)
GALILEO	(11)	(500)	CHARLESTON	(12)	(1500)
MORGAN	(8)	(500)	HARDTACK 1 - All Shots		
SMALLBOY		(0)			

NOTES:

(a) Heavily shielded

- The presence of the ground can be important to the formation of the air blast and dust lofting
- Dust can be lofted prior to shock arrival
- A hot layer can be generated near the ground
- The hot layer is heated air containing particulate matter
- The hot layer can significantly modify the air blast flow field (e.g., form a precursor)
- Passage of the precursor generates a significant upward component of material velocity
- A copious dust layer can follow a precursor and grow to several hundred feet
- High dust layers are not raised behind non-precursed flows
- The data on dust lofting are inadequate to allow an empirical model to be developed from the NTS nuclear series.

SECTION 5

POST-SHOCK DUST LOFTING MECHANISMS

The formation of the sweep-up dust cloud and the mass loading within the cloud have been described by several investigators (References 14, 46 and 47). The models presented in Reference 46 and 47 may be described as aerodynamic shear models, where the air flow induced by the passage of the blast wave results in aerodynamic forces that loft individual particles into the flow field. Although these models were developed for other specific reasons, the possible use of them to describe late time cloud development had been considered earlier (Reference 14) by SAI. For this effort it was decided that these models should be reviewed again, but this time in the context of possible use in air blast calculations. Before discussing their utility the description of the available models, taken from Reference 14, is briefly summarized in the next three subsections.

5.1 IITRI DUST ENVIRONMENT MODEL

The Illinois Institute of Technology Research Institute (IITRI) study, which is described in detail in Reference 46, is oriented toward environments which are potentially detrimental to hardened power systems, particularly air intake and exhaust systems. For this application, the formation and transport of the near-surface dust cloud by the blast-wave induced wind field and the subsequent transport of the cloud by ambient winds are of primary interest. The blast-wave model used in Reference 46 includes the influence of the negative phase flow field but not the influence of the afterwinds induced by the rising fireball. The ground surface conditions may be specified and may be variable. The airborne dust densities are assumed to be sufficiently small that there is no influence of the dust on the air flow field. Thermal effects are not included in the model.

The IITRI dust model may be conveniently partitioned into early-time and late-time phases. The early-time behavior of the dust cloud is described by an erosion or lofting process, a transport process, and the particle size distribution. This early-time dust cloud is driven by the blast-wave wind field. The end of the early-time phase, after the cessation of the inward directed air velocities associated with the negative phase, provides the initial conditions for the late-time phase. The late-time dust cloud history, which includes a growth phase and a settling phase, is determined by the magnitude of the ambient winds.

The early-time lofting or erosion process is driven by the horizontal motion of the air. The aerodynamic forces acting on individual particles loft each of these particles independently. The number of particles eroded per unit time is related to the particle size, the particle mass density, the in situ soil density, the horizontal air velocity, the particle terminal velocity, and an empirical erosion constant. It is assumed that the air velocity must be greater than 5 times the terminal velocity before a particle can leave the surface. The terminal velocity is determined as a function of particle size using air properties and a smooth-sphere drag coefficient. The total mass available for lofting is determined by the erodible depth. Land use, such as agricultural or urban, is accounted for in the specification of the soil-related model parameters.

In the IITRI model for dust transport, it is assumed that the horizontal motion of the dust, after lofting, is identical to the horizontal motion of the air. Particle lag relative to the air is, therefore, neglected. The horizontal air velocity is also assumed to be uniform in the vertical direction, so that the boundary-layer velocity distribution attendant to the flow behind the blast wave is not included in the model. The vertical transport of the dust is subject to the effects of air turbulence, which provides local upward particle motion and gravitational forces. The local vertical velocity is assumed to be a fraction (≈ 0.5) of the horizontal velocity.

The final parameter employed in the IITRI model for the early-time dust environment is the normalized dust distribution function, the density of particles (number per unit volume) of a given diameter associated with a given lofting position. It is assumed that this distribution is similar at all times and for all particle sizes.

The complete early-time dust distribution is determined by combining the descriptions of the lofting process, the transport process, and the normalized particle distribution function. The contributions of each dust packet, representing a given particle size and lofting location, are transported through the flow field and integrated to give the total loading as a function of time, height, and range from the burst point. This description of the dust environment is assumed valid to the time of cessation of the blast-induced winds.

Following the early-time phase, the dust environment is described by a late-time model but since the latter is of no interest to this effort, it is not reviewed here.

5.2 ATI DUST LOFTING MODEL

A lofting and transport model that potentially includes all pertinent regions of the nuclear dust cloud was developed by Applied Theory, Inc. (ATI) and reported in Reference 47. The aerodynamic shear lofting model that provides the dust source is based on previous descriptions of particle lofting in naturally occurring dust and sand storms. The transport model, a hydrocode called DUST, generates the complete nuclear wind field in a discrete spatial grid as a function of time and permits tracking of trajectories of an arbitrary number of particles through the flow field. The blast-induced wind, the negative phase, and the afterwinds associated with the rising fireball are described by the transport model. The sizes of particles available and the particle size distribution may be specified as functions of range from the burst point.

The shape of the developing crater is modeled at each time step in the calculation so that material lofted from within the crater region originates from the actual crater surface. The effect of the airborne dust particles on the air flow field is assumed negligible. The low density region occupied by the fireball is considered in the model and the particle trajectory calculation accounts for the effect of the hot gases. No other thermal effects are included in the model.

The ATI dust model may be considered to be comprised of a lofting model and a transport model. In the terminology applied earlier to the IITRI model, the ATI model describes only the early-time phase of the dust transport.

The ATI dust lofting model describes a mechanism for injecting surface material into the flow field associated with a nuclear burst. The background for the model was developed in the literature for dust and sand storms; however, additional assumptions were required because of the high air velocities in the positive phase for the nuclear case. With respect to these additional assumptions, the ATI model was designed to give an upper limit to the amount of material lofted in a nuclear surface burst. As in the IITRI model, particle-to-particle interactions are neglected. The horizontal gas velocity near the ground (actually between the surface and the first grid point in the hydrocode calculation) is specified by the logarithmic law of the wall for turbulent boundary layers. This is a velocity profile characteristic of high Reynolds number flows over flat plates and in pipes. The formulation used is:

$$\frac{U}{u_\tau} = 2.5 \ln \left(\frac{2gy}{u_\tau^2} \right) + 9.7 \qquad (7)$$

where U is the horizontal gas velocity at height y above the surface and the shear velocity, u_τ, is defined by:

$$u_\tau = \sqrt{\frac{\tau}{\rho}} \qquad (8)$$

where τ is the surface shear stress and ρ is the gas density. The velocity U and density ρ are evaluated at the height of the first grid point above the surface [y in Equation 7]. The vertical gas velocity between the surface and the height y is assumed to vary linearly from zero to the hydrocode vertical gas velocity at height y. The implication of these assumptions is that the height of the aerodynamic shear layer is equal to the height of the first hydrocode grid point above the surface, and that the gas velocity components within the shear layer are determined by the corresponding components of the gas velocity at this point.

The mechanism for lofting a dust particle is as follows. The gas delivers a horizontal force per unit area, equal to the local shear stress, from Equation 8. This force is converted to vertical momentum. Various restrictions are placed on the vertical velocity of the particle, depending on the particle size and the maximum horizontal gas velocity at the edge of the shear layer. Since the vertical momentum is specified, these restrictions affect the amount of mass lofted as well as the injection velocity. A maximum size particle that can be lofted also results.

Once injected into the flow field, the individual particles are tracked using the DUST code. The smooth-sphere drag law is employed for the particle drag. The instantaneous position and velocity of each particle are computed at each time. Mass and momentum densities are then computed as functions of range, altitude, time, and particle size. When a particle impacts the ground, the impact position, velocity, and time are recorded and the particle is deleted from the calculation.

5.3 S^3 DUST LOFTING MODEL

The SCOUR dust lofting model was developed by Systems, Science and Software (S^3) to describe the sweep-up dust lofting process and the eventual transport of the lofted dust into the central cloud and stem. The model is delineated in detail in Reference 48. The aerodynamic

shear model for dust lofting is an extension of that reported in Reference 47, with additional consideration given to the simulation of particle diffusion within the surface boundary layer and the effects of turbulence in the boundary layer and the flow field. The boundary layer model is considerably more developed than that employed in the ATI model (Reference 47) and is considered separately from the transport model in the following paragraphs. The SHELL hydrocode results are used for the nuclear wind field in the transport model. As in the DUST code (Reference 47), the flow field is provided on a spatial grid as a function of time and representative particles are tracked through the flow field. The SHELL flow field includes the blast-induced positive phase, the negative phase, and the afterwinds. The soil available for lofting is assumed to be comprised of a finite number of particle sizes with the size distribution specified by a mass weighting function. Variable surface conditions are not included, and it is assumed that no particles are lofted from the crater region. As in the models described previously, the effect of airborne dust particles on the air flow (including that within the boundary layer) is assumed negligible. The effect of the developing boundary layer on the SHELL flow field is not considered. The SHELL flow field description includes the variation of gas properties associated with the hot fireball. No other thermal effects are included in the S^3 model.

The S^3 dust model may be described as a combination of a lofting model and a transport model, with the boundary-layer model providing a means of transporting the lofted particles to sufficient altitudes to be injected into the SHELL flow field. In the terminology applied previously, the S^3 model describes only the early-time dust transport phase. Effects of ambient winds are not included.

The S^3 dust lofting model is comprised of two lofting mechanisms: aerodynamic lofting due to surface shear and ejection of new particles as a result of impacting of previously lofted particles. The aerodynamic shear model is based on the literature related to dust and sand storms, the previous ATI model (Reference 47), and recent experimental data for dust lofting by high velocity air streams and shock waves (References 49, 50). The positive and negative phases are considered separately; however, the same basic lofting model is applied in both phases. A formulation derived from the law of the wall

$$\frac{u_\tau}{U} = \frac{0.707}{2.87 + 0.7 \ln \frac{x}{k_s}} \; ; \quad \frac{x}{k_s} \geq 1 \tag{9}$$

is employed for the shear velocity of u_τ (Equation 8). This is described as a perfectly rough wall boundary-layer model in Reference 48. The term k_s is a roughness height equal to a characteristic height of certain size particles in the boundary layer. For positive phase, x is the distance behind the blast wave, and the boundary-layer growth is based on a quasi-steady formulation of the boundary layer behind the shock wave. The negative phase boundary-layer growth is assumed to be analogous to that for an impulsively started flat plate moving at velocity U. For this phase

$$x = \int_{t_o}^{t} U \, d \, t \tag{10}$$

where t_o is the time at which the negative phase begins at a given range from the burst point. For both phases, the incompressible integral boundary-layer equation is solved using a 0.5 power-law profile. The boundary-layer thickness is restricted to a maximum of 100 m.

The aerodynamic shear lofting model is driven by the local shear velocity u_τ. The total mass lofted is given by

$$\dot{m}u_\tau = 0.1(\tau - \tau_{th}) \, dA \tag{11}$$

where $\dot{m}$ is the mass lofting rate from surface area dA, and τ_{th} is a threshold shear level below which no lofting will occur. Particles are ejected vertically with a velocity equal to u_τ at a delay time t_d after shock arrival. A correlation for t_d was derived from shock tube data.

When a previously lofted particle impacts the ground, a new particle is ejected with zero horizontal velocity and vertical velocity equal to

$$V_{ejection} = -V_{impacting} + 0.1 \, |U_{impacting}| \, . \tag{12}$$

The same mass is ejected and the size of the characteristic particle being ejected is selected randomly from the postulated particle size distribution of the in situ soil. This part of the model describes the equilibrium saltation condition.

The major difference between the S^3 and ATI models, rests in the descriptions of the air velocity distribution within the boundary layer. In the ATI model, the boundary-layer thickness is simply the distance from the surface to the first grid point in the flow field. The horizontal gas velocity was given by Equation 7 and the vertical gas velocity was assumed to vary linearly from zero at the surface to the vertical flow field velocity at the first grid point in the flow field. In the S^3 SCOUR model, the boundary-layer thickness, $\delta < 100$ m, is calculated as a function of the range from the burst point and time. The horizontal gas velocity is assumed to be given by the 0.5 power-law profile. The vertical velocity is described by a number of diffusion and turbulence components:

- A SCOUR velocity

$$V = 0.5u_\tau \quad , \quad y \leq \frac{\delta}{4} \tag{13}$$

- A turbulence velocity for upward motion

$$V = 0.5u_\tau + 2v_{diff}, \quad \frac{\delta}{4} < y < \frac{5\delta}{4} \tag{14}$$

where

$$v_{diff} = \frac{\theta}{\zeta} U \tag{15}$$

θ is the boundary-layer momentum thickness, and ζ equals the distance behind the shock wave for the positive phase or is given by Equation 10 for the negative phase:

- A turbulence velocity for downward motion

$$V = -0.5u_\tau \quad , \quad \frac{\delta}{4} < y < \frac{5\delta}{4} \tag{16}$$

- An updraft velocity

$$V_{up} = V \frac{y}{\delta} \quad , \quad y \leq \delta \tag{17}$$

where V is the vertical flow field velocity at the edge of the boundary layer. The net vertical velocity within the boundary layer is given by the sum of Equations 13, 14, or 16 and 17. The upward and downward turbulence velocities, Equations 14 and 16, respectively, are applied randomly. Note that the updraft velocity, Equation 17, is identical to the vertical velocity used in the ATI model (Reference 47).

When applying the SCOUR model, the SHELL flow field provides the edge conditions for the boundary-layer calculation. The region around the burst point is partitioned into annular rings, and the lofting criteria are applied to determine the mass lofted and the time of lofting for each ring. Each representative particle is then transported across the boundary layer and into the flow field. The smooth-sphere drag law is employed for the particle drag. An additional turbulence term is

modeled for the particles in the flow field by reducing the gravitational forces whenever the particles are descending. The positions and velocities of all particles are recorded at each time step in the calculation. If a particle impacts, a new particle is ejected as discussed above. The output of the SCOUR code is comprised of the local dust concentration versus range, altitude, and time, the total mass airborne, the mass above a given surface zone, the mass in a disc between two altitudes, the boundary-layer properties, and the number of particles created.

5.4 DUST LOFTING BY THE NUCLEAR AIR BLAST PRECURSOR

Two of the current sweep-up dust cloud models (ATI and S^3) couple the prescription of the wall shear and boundary-layer growth with flow fields computed using hydrocodes. However, the hydrocode calculations were performed with the assumption that the ground surface is an ideal rigid surface and no precursor forms. Under those conditions the velocity vectors near the ground surface are horizontal, and in the absence of preshock thermal effects, any dust lofting would be the result of surface shear stress and particle impacts, the mechanisms employed in the current modeling efforts reviewed above. Because the velocity vectors are parallel to the surface for bursts over ideal surfaces, the particles lofted by these mechanisms attain only a fraction of the observed altitude. When the results obtained using the pure aerodynamic shear models were compared to the available experimental data, it was seen that the predicted dust heights reach only a fraction of the observed heights for some events unless the equations of motion are modified to include very large-scale turbulent diffusion terms that have not at the present time been verified experimentally (Reference 14). The discrepancies between the model predictions and the observations are believed to be related to several factors, the most important of which is the effect of fireball thermal radiation on the ground surface prior to the arrival of the air blast wave and the formation of the blast-wave precursor.

Over non-ideal surfaces the blast wave encounters a heated near-surface dust and air layer causing the portion of the wave in the heated layer to propagate faster than the main wave above due to the higher sound speeds in the hot layer. The result is similar to the classical lateral wave (Reference 51), i.e., the blast-wave precursor. Velocity vectors in the precursor are not parallel to the ground; they have large vertical velocity components. Hence, any dust that would be injected into the precursor region would be lofted by these vertical components that are absent in the ideal blast-wave calculations. This is confirmed by the fact that the weapons tests in Nevada where blast-wave precursors were present consistently indicated that large clouds of dust were observed to rise immediately behind the precursor wave front, as was discussed in Section 4. In addition, the results of dust particle trajectory calculations in the precursor region indicate that the precursor flow field is sufficient to loft dust to the observed altitudes.

5.5 APPLICABILITY OF DUST LOFTING MODELS TO AIR BLAST

The applicability of the current dust lofting and transport models to the prediction of air blast for precursor bursts is summarized below. The IITRI model (Reference 46) was developed using correlations for many non-precursor and precursor bursts and thus represents an average, and for that reason is considered to be of limited general usefulness to the air blast problem.

Model	Reference	Precursor
IITRI	7.1	Limited
ATI	7.2	Possible
S^3	7.3	Possible

The ATI and S^3 models have been applied primarily to non-precursor bursts. The mechanisms for simulating precursor bursts are inherent in the approaches employed, so that precursor bursts may be analyzed simply by using the appropriate hydrocode calculation for the flow field. It is evident, however, that the aerodynamic shear lofting model may not be sufficient for precursor bursts, and for this reason we are recommending a simple model for the preshock thermally lofted dust.

Since the S^3 models are the ones most recently worked on and embody the important features of the ATI model (at least for this application) we limited our effort to further consideration of only the S^3 models.

5.6 WIND TUNNEL AND SHOCK TUBE EXPERIMENTAL STUDIES OF DUST LOFTING

For the most part few data exist upon which to confidently model the dust lofting phenomena. References 49 and 50 for the most part contain the limits of our knowledge. The data from Reference 49 was incorporated into the SCOUR and SCOUR 2 models.

Hartenbaum reported his wind tunnel studies of particulate lofting at free stream speeds of between 112 and 376 in Reference 49. The most important data to come from these experiments was the measured lofting rate which was 1/10 that being predicted prior to his experiments in 1971. Kirsh (Reference 48) used these data in the SCOUR model; however, uncertainty exists as to the validity of using these data for M-X applications for the following reasons. First, the maximum speeds considered are low by a factor of ten to twenty when compared to the nuclear air blast of interest in the M-X problem. Secondly, the cohesiveness of the soil is not considered. Nevertheless, these do represent the best data available and should be used in an interactive dust calculation to estimate the plausible influence of dust on air blast loading for M-X.

Ausherman (Reference 50) performed some shock tube tests to investigate the initial dust-lofting process occurring just behind a blast wave passing over a soil-like surface. The primary result of the study showed the importance of soil porosity. Rarefaction waves propagated from the soil surface and caused the otherwise plane shock (which was normal to the soil surface) to become curved and propagate somewhat towards the soil surface. Ausherman believes that the altered flow conditions behind the shock, i.e., the velocity gradient in the freestream, may contribute to the transport of dust once lofted. It is the opinion of this author that this effect will be small compared with the significant flow field distortions expected in a precursed event.

In any event, Ausherman does measure dust density profiles which will be useful when attention is focused on validating the SCOUR model against laboratory data.

SECTION 6
SIMPLE ANALYTIC MODEL FOR THERMAL BLOW-OFF OF PRESHOCK DUST

This section reviews a simple analytic model for thermal blow-off of dust recently developed and reported by SAI (Reference 52). A part of it is described here as necessary background for understanding the basis for the recommendations made in a later section. The following material does not include the details of how to analytically include recommended particle size distributions. Instead the basic features of the model are described and the reader is referred to Reference 52 for an example of how to use this information analytically if the appropriate particle size distributions are chosen.

6.1 BACKGROUND

As the soil heats up from fireball thermal radiation, particles are blown off into the air, where they can continue to intercept this radiation. These particles are heated radiantly and they, in turn, heat the air by conduction and convection. This dust is also available for ingestion into the blast wave, where it can be raised to altitudes of several hundred feet by the vertical velocities which occur in precursor flow fields. Therefore, production of dust by surface blow-off is important, both for creation of the preshock thermal layer necessary for precursor formation and for the dust loading of the persistent near-surface dust layer produced by precursor shots. In addition, its presence may seriously affect the air blast flow field itself.

The purpose of this Section is to review a very simple physically motivated model of this dust blow-off phenomenon. The assumption inherent in the model is that the dust blow-off is determined by the thermal radiation actually reaching the ground surface. The model therefore, has two parts: first, a model for the reduction or attenuation of

the incident radiation due to obscuration by the dust already blown off; and second, a model for dust production in terms of the attenuated radiation reaching the ground surface.

6.2 ATTENUATION OF RADIATION BY DUST

At a given time t, when there is an amount of mass dM(t)/dA per unit area blown off in the air, the transmission coefficient of the dust layer is defined to be f(t). It is assumed that extinction in the layer is proportional to the total cross sectional area occupied by dust particles:

$$1 - f = c \frac{dA_p}{dA}, \tag{18}$$

where dA_p/dA is the fraction of the area occluded by dust particles (including self-shielding, as will be explained shortly), and c is an appropriate multiplier. For instance, c = 1 corresponds to geometrical occlusion, such that extinction of the light beam is equal to the fraction of the area occluded by dust particles. For wavelengths much smaller than the particle diameter, the total cross section for the scattering from a sphere is, on the Mie theory, twice the geometrical cross section, due to diffraction effects. This corresponds to c = 2 and is probably appropriate for dust densities small enough that no self-shielding occurs.

Unless the dust density is very low, self-shielding will occur. That is, some particles will not contribute to the extinction because they are occluded by larger particles. For normal incidence, a small particle above or below a larger particle will not contribute to the extinction. Consider dust particles of diameter in the range a to a+da. Some fraction of them could be shielded by other particles above or below them and not contribute to the overall extinction coefficient, 1 - f, of the dust layer, as illustrated by the following sketch:

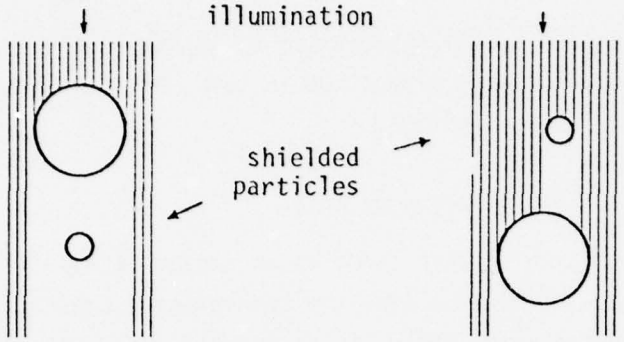

It is clear by inspection that particles of diameter a can be shielded in this fashion only by particles larger than a. For a uniform random spatial distribution of particles of diameter a, the probability that such a particle will be shielded in this fashion is just the fraction of the area occluded by particles larger than a. This will be denoted $dA_p(a)/dA$, and is a monotonic decreasing function: for particle sizes bounded by a_{min}, a_{max}, one has

$$\begin{aligned} \frac{dA_p}{dA}\ (a_{min}) &= (1 - f)/c \\ \frac{dA_p}{dA}\ (a_{max}) &= 0. \end{aligned} \tag{19}$$

This approximation neglects edge effects, i.e., partially occluded particles whose centers are occluded are considered to be totally occluded.

Now consider populating the dust layer sequentially by size, starting with the largest. With particles of diameters from a to a_{max} in the layer, the fraction of the area occluded is just $dA_p(a)/dA$. Consider the increase in this quantity as particles in the size class from a to a -da are added to the layer; it is

$$\frac{d}{da}\left(\frac{dA_p(a)}{dA}\right)(-da),$$

which is a positive quantity due to the monotonic decreasing character of dA_p/dA. The number of particles added per unit area is given in terms of the particle size distribution

$$\frac{dn}{dA} = \frac{d^2n}{dAda} \quad da. \tag{20}$$

Each of the added particles will contribute its cross-sectional area, $\pi a^2/4$, if it is not shielded. But the fraction not shielded is just $1 - dA_p(a)/dA$. Therefore, the increase in the fractional area occluded is given by

$$\frac{d}{da}\left(\frac{dA_p(a)}{dA}\right)(-da = \frac{\pi a^2}{4} \cdot \frac{d^2n}{dAda}\ da \cdot \left(1 - \frac{dA_p(a)}{dA}\right). \tag{21}$$

Integration of Equation 21 gives

$$\frac{dA_p(a)}{dA} = 1 - \exp\left(-\int_a^{a_1} \frac{a^2}{4} \frac{d^2n}{dAda}\ da\right) \tag{22}$$

where the limit a_1 is the largest particle diameter, such that $dA_p(a_1)/dA = 0$.

To proceed further, the particle size distribution must be specified. This is done in Reference 52 and is not included here. When a mass dM/dA has been blown off, Equations 19 and 22 give the transmission coefficient as

$$f(t) = c \exp\left(-B \frac{dM}{dA}\right) - (c-1). \tag{23}$$

6.3 MODEL FOR DUST PRODUCTION

The second part of the model describes the dust blow-off as a function of the radiative flux reaching the surface. In Appendix B it is shown that, within rather broad errors, dust blow-off from NTS soil is proportional to the fluence received, with a specific energy of blow-off E:

$$1230 < E < 4140 \text{ cal/gm} \tag{24}$$

where the median E_o = 2260 cal/gm.

Therefore, if $\dot{Q}(t)$ is the effective flux at the top of the dust layer (i.e., corrected for albedo), the mass blown off by time t is given by

$$\frac{dM}{dA}(t) = \frac{1}{E}\int_0^t f(t)\dot{Q}(t)\,dt. \tag{25}$$

The resulting differential equation is

$$\frac{d}{dt}\left(\frac{dM}{dA}(t)\right) = \left[c \exp\left(-B\frac{dM}{dA}\right) - (c-1)\right]\frac{\dot{Q}(t)}{E} \tag{26}$$

which can be reduced by the substitution

$$Z - \exp\left(B\frac{dM}{dA}\right) \tag{27}$$

to the linear form

$$\frac{dZ}{dt} + (c-1)\frac{B\dot{Q}}{E}Z = c\frac{B\dot{Q}}{E}. \tag{28}$$

The solution, subject to the boundary condition Z(0) = 1 and well-behaved as c goes to 1, is

$$Z(t) = 1 + \frac{1}{c-1}\left|1 - e^{-(c-1)\,BQ(t)/E}\right| \tag{29}$$

where Q is the total fluence received:

$$Q(t) = \int_0^t \dot{Q}(t)dt. \tag{30}$$

The final result, written in terms of incident fluence and a dust layer albedo α, is

$$\frac{dM}{dA}(Q) = \frac{1}{B}\ln\left[1 + \frac{1}{c-1}\left(1 - e^{-(c-1)(1-\alpha)\,BQ/E}\right)\right] \tag{31}$$

where c and E are defined in Equations (18) and (24), and B is a function of the particle size distribution. For c = 1, Equation 31 reduces to

$$\frac{dM}{dA}\ (Q) = \frac{1}{B}\ \ln\ (1 + (1-\alpha)\ BA/E). \qquad (32)$$

6.4 MODEL SENSITIVITIES

The model sensitivity to these inputs was investigated in Reference by performing parameter studies for maximum particle size, for specific energy of blow-off, and for geometrical (c=1) screening vs. Mie (c=2) screening for a particular particle size distribution. The amount of blow-off was severely reduced by screening, with Mie screening reducing it the most. Sensitivity to maximum particle size was not great (a factor of fifty percent in blow-off for a tenfold increase in particle size), nor was the effect of the poorly known specific energy of blow-off (a factor of two decrease in lofting for a factor of 3.36 in blow-off energy). The presence of the logarithm in Equation (31) is responsible for the relative insensitivity to fluence, albedo, and specific energy of blow-off.

The study was performed based on the following assumptions and approximations: 1) the incident beam is attenuated by a fraction proportional to the fractional area covered by particles; 2) occlusion is approximated by Equations (19) and (20); 3) particles are spherical; 4) particle size distribution was a hybrid lognormal - power law described in Reference ; 5) blow-off mass is proportional to the fluence received on the ground; and 6) all the blow-off mass stays in the air (fallback is not considered). For those conditions and the data in Table 5, the results are summarized in Figures 13 and 14.

Table 5. Blow-off model parameter values for NTS calculations

Grain Density	$\rho = 2.6$	gm/cm^3
Lognormal Median	$a_o = 20$	microns
Lognormal Sigma	$\sigma = 0.69078$	
Matching Point	$a_x = 180$	microns
Dust Albedo	$\alpha = 0.375$	
Blowoff Energy	$E = 2260$	cal/gm
Geometrical Screening	$c = 1$	
Maximum Particle Size	$a_1 = 50$	microns

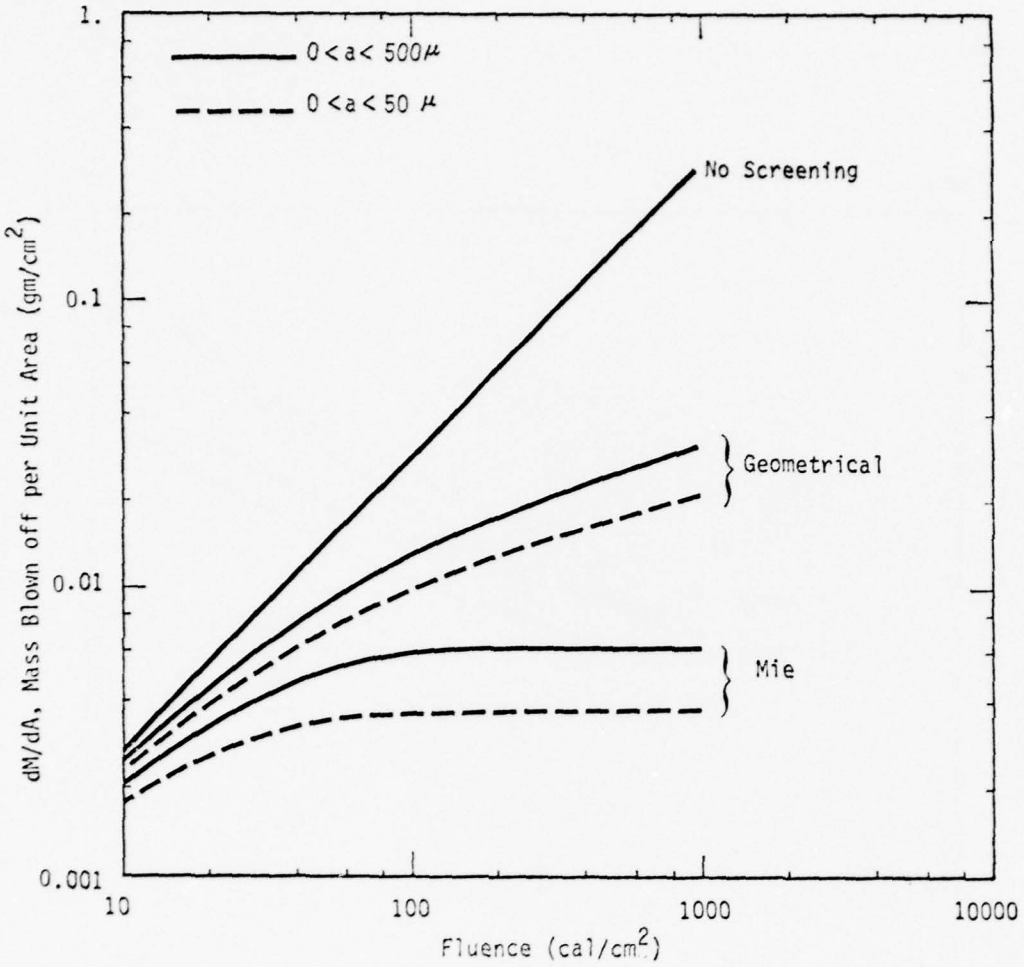

Figure 13. Parameter studies on blow-off model: geometrical vs. Mie screening

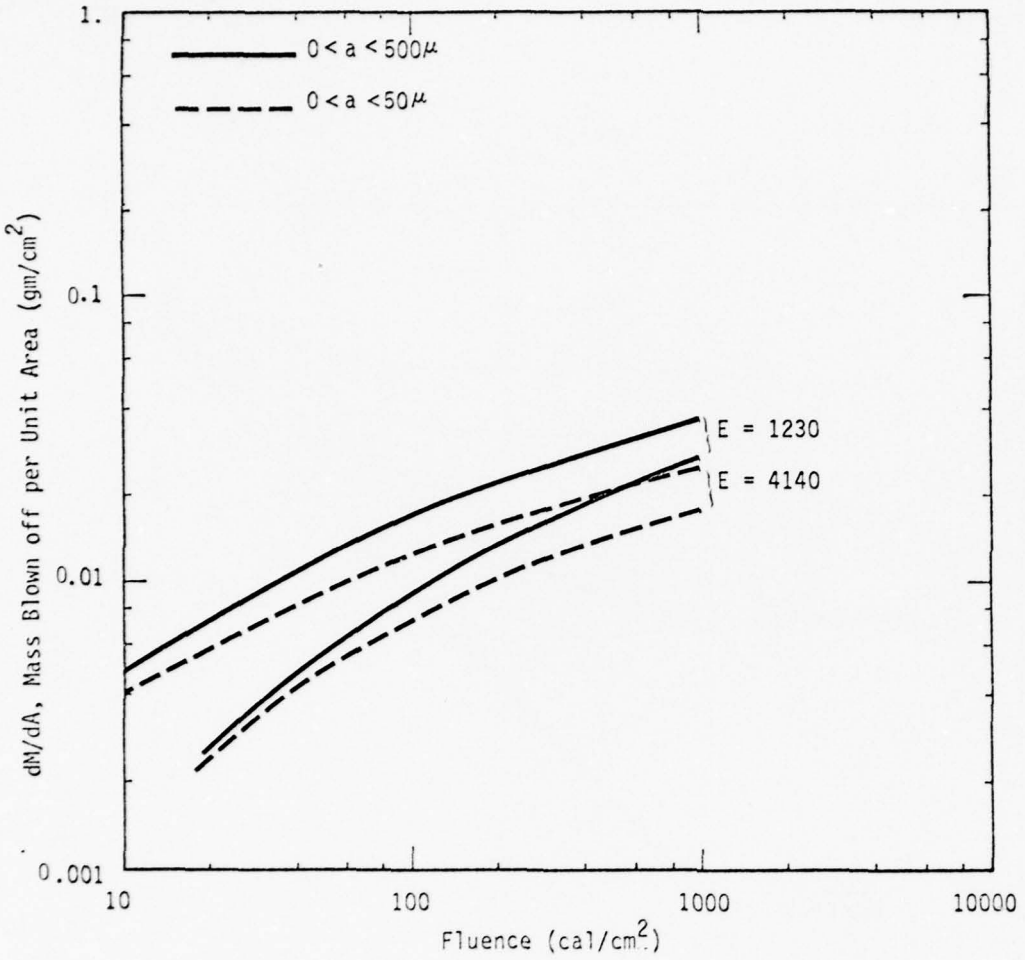

Figure 14. Parameter studies on blow-off model: effect of blow-off energy

SECTION 7

RECOMMENDED MODELS FOR DUST LOFTING IN AIR BLAST CALCULATIONS

This section presents recommendations made to DNA and the AFWL regarding models of dust lofting that it is believed the AFWL should use in HULL air blast calculations performed for the M-X Concept Validation Program. Specifically recommended is use of part of the simple first principles model, described in Section 6 and reference 52, developed for pre-shock dust that would be blown off by thermal radiation and subsequently lofted by the flow field. This model when used with coefficients recently determined from the solar furnace tests at White Sands Missile Range (WSMR) reference 53, should provide best estimates for the dust environment. For the post-shock environment it is recommended that use be made of a simplification of the dust lofting models employed in SCOUR 2. The flow field velocities needed for use in this model would come from any hydrodynamic calculation as it is being performed. The dust should be allowed to interact with the flow through an aerodynamic drag force. The following sections summarize the recommended formulation, and the final section discusses anticipated problems and their solutions.

7.1 PRE-SHOCK DUST LOFTING

Based on the basic assumption that dust blow-off (pre-shock) is determined by the thermal radiation actually reaching the ground surface, a simple yet physically motivated model was developed and discussed in Section 6. The model when calibrated with recent solar furnace experimental data, should provide the best estimate available today for specifying the lofted dust as a function of the incident thermal radiation flux.

The model when simplified for air blast calculations is

$$\dot{m} = \frac{\dot{Q}(t)}{E} \tag{33}$$

where $\dot{m}$ = mass lofting rate (gm/cm^2-sec)

$\dot{Q}$ = thermal radiation flux (cal/cm^2-sec) incident on the ground and E is dependent on the soil characteristics (cal/gm).

From the solar furnace data shown in Table 6 (which was extracted from Reference 53), E for Tularosa Basin varies between 3000 and 5000 cal/gm. To maximize the dust loading (pre-shock), the value of 3000 cal/gm should be used.

It is recommended that particles be lofted normal to the ground at a velocity of 100 cm/sec.

7.2 AERODYNAMIC LOFTING IN SCOUR 2

Based on review of the SCOUR and other reports, the following form for adding dust particles to be lofted via aerodynamic forces during and after shock passage is recommended.

$$\dot{m} = \alpha\,(\rho U_*^2 - \tau)/V_o \qquad (34)$$

$\dot{m}$ = mass lofting rate (gm/cm^2-sec)

α = 0.1 (best estimate) use 0.3 as a reasonable excursion for dry, hard soils

ρ = air density (gm/cm^3)

U_* = aerodynamic shear velocity (cm/sec)

τ = threshold shear pressure (use 1 dyne/cm^2)

V_o = particle ejection velocity (cm/sec)

For the calculation of shear velocity the use of

$$\frac{U_*}{U_e} = \frac{0.707}{(2.87+0.7\ \ln\frac{\zeta}{k_s})}\ , \quad \frac{\zeta}{k_s} \geq 1 \qquad (35)$$

U_* = Shear velocity in the boundary layer

$= \sqrt{\tau_o/\rho}$ τ_o = shear at wall, ρ = air density

Table 6. Summary of soil blow-off data[1]
(extracted from pg. 17, Reference 53)

Physical Description and Data \ Soil Types	Pure Clays	Pure Sands	Top Soils Eastern US	Minuteman Sites	Alluvial Playas Frenchman Flats	Yucca Flats	Tularosa Basin
Geophysical Soil Description: Formation	Fluvial	Littorial	Fluvial	Glacial	Alluvial	Alluvial	Alluvial
Geography			Humid Mid Latitude	Mid Latitude Steppe with Vegetation and Organics	Desert	Desert	Desert
Physical Properties[2]	High Albedo (~30%) Mean Grain Size About 10μ	Very High Albedo (~40%) Mean Grain Size about 100μ	Vegetation Cover Low Albedo Grain Size~50μ	Very Low Albedo Mean Grain Size in Range 50-100μ	High Albedo (~30%) Mean Grain Size 150μ	High Albedo (~30%)	High Albedo (~30%) Mean Grain Size 5μ
Blow Off Fluence Thresholds:[3] Smoke (cal/cm^2)	4	6	4	5	7	Little or no Smoke Activity	7
Particulate (cal/cm^2)	4 Small Particles 10-30 Large Flakes (At High Flux Only)	5-20 Depending on Moisture	7- and Higher Depending on Soil Type	None observed	6	16	10-20
Initial Velocity Smoke (m/sec)	$Q^{0.5}$	0.5	0.5	0.3 to 0.6	0.2 to 0.5	None observed	0.4
Particles	Up to 10.0 for Large Particles	1 to 2	1.0	None Observed	0.5 to 1.5	1 to 3	1 to 2
Normalized Weight Loss x 10^4 gm/cal	6	4	N/A	3 to 6.5	3	5	2 to 3
	1670 cal/gm	(Function of Moisture) 2500 cal/gm		1540 to 3333	3333	Depends strongly on Moisture	3333 to 5000
% Obscuration (At 2 sec for Q = 20 cal/cm^2 sec)	30 to 50	0% for Dry Sands - Up to 50% for Very Wet	Low	N/A	40% For Dry Sample -- Decreases with Moisture	Very Low	0% for Dry Samples Up to 50% for very Moist Samples
O_2/% Moisture (cal/cm^2/%)	3	Depends Strongly on Moisture[4]	N/A	2	Small	2	N/A
Air Temperature ΔT/ΔQ at ¼" (°K/cal/cm^2)	15	3		40	50	50	
Remarks:	Pure clays exhibit unique blow off mechanisms--very fast particle and flake blow off.	Particulate blow-off highly dependent on moistur	Sparce particulate blow off	Glassy layer formed on surface		Absence of smoke is a unique feature. Weight loss is for 5% moisture in natural state.	

1) Based on 273 tests of 25 separate soil samples over a flux range of 5 to 80 cal/cm^2 sec, table values are independent of flux unless noted.

2) Samples were investigated in both natural moisture states, dried, and for various degrees of added water, unless noted table values refer to all moisture states.

3) Thresholds are independent of flux over a range 7 to 80 cal/cm^2 sec within a factor of 2. The main flux dependent effects are observed from flux threshold of about 7 cal/cm^2 sec to about 15 cal/cm^2 sec however. See Figure 10 and 11 in above reference for further details.

4) The low value of air heating is accompanied by very high temperatures in the sand substrate.

U_e = Free stream velocity (tangent to the ground)

ζ = Distance behind air shock for the positive phase

k_s = Roughness height (depends on particle size)

as found in SCOUR is recommended, where a reasonable value of k_s would be the average (mass weighted) particle radius. For the ejection velocity use

$$V_o = (0.5 + 0.5\ N_R)\ U_\star \qquad (36)$$

where N_R is a random number between 0 and 1.

The particles should be lofted randomly in an angle between 10^o and 90^o in the plane which is normal to the ground and contains both the point in question and the burst point. The angle is measured from the ground surface. Further the particles should have a component of velocity along the ground with identical sign to that of the flow.

For both pre-shock and post-shock lofting five particle size classes (or more if feasible) are recommended for use where each class contains equal amounts (mass) of soil. In lieu of better data, we recommend the use of pre-event particle size distributions. Since interactive* dust calculations are recommended, the particle radius representing each particle class should be based on an averaging appropriate to the air particle drag.

7.3 IMPLEMENTATION OF THE MODELS IN HULL

In order to implement the above models in a hydrodynamic code (e.g., HULL) various problems will need to be addressed by experienced personnel. To use the pre-shock dust loading model a predictor of the thermal radiation arriving on the ground up to the time of shock arrival will be required. An example of such a prediction technique already

*In the sense as used in HULL. Specifically the particles and fluid are coupled through the aerodynamic dray force. Thus, each particle is affected kinematically by the flow, and conversely the flow is affected (momentum and energy exchange) by the particles.

exists in HULL for a point source fireball. It could easily be improved with an available model representing fireballs that are truncated by the ground which is included here as Appendix C for completeness. Another problem associated with the pre-shock dust lofting is accounting for the attenuation of radiation through the dust. Here, the models that exist in the AFWL Thermal Layer Predictor are recommended for use until such time that they are superceded by better models currently under development by LASL for DNA. If the attenuation effect is not included, too much dust will be lofted.

Problems associated with the scouring model have to do with what to do with the thermal radiation arriving after the shock on the flow field. Since the thermal radiation post-shock for the scenarios of interest is quite significant, we recommend that the energy be added to the dust during at least one calculation to assess its relative importance. Again the computation of attenuation (and absorption) through the dust can be based initially on the simple models in the AFWL thermal layer predictor. An example of the severity of the thermal environment is included as Figure 15 which shows the thermal radiation incident on the ground (ignoring lofted dust) at a range of 706 m for 2MT surface burst (or 4MT free field). These data were obtained with a detailed multi-frequency radiation transport code, SPUTTER (see reference 54 for example); the results are shown for SPUTTER problem FB10 (reference 55).

A problem associated with using both dust lofting models has to do with the required number of particles to adequately represent the physics. The importance of providing sufficient numbers of particles to adequately model the dust has been demonstrated at the AFWL during development of the thermal layer. If the required number is found to be affordable, use of the models above should be straightforward. If on the other hand, too many particles are required then alternative

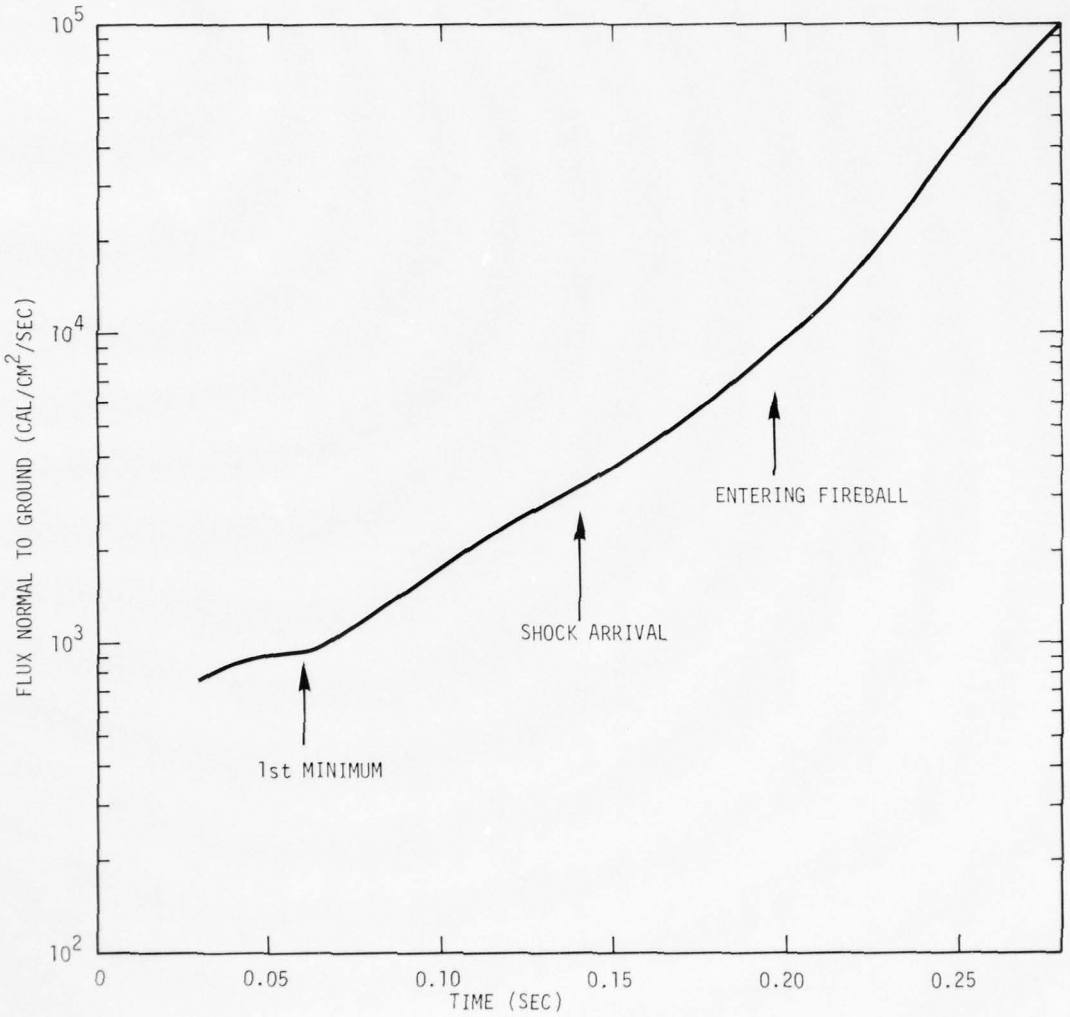

Figure 15. Flux normal to ground from a 2 MT surface burst (data from SPUTTER FB 10) range 706 m

approaches (e.g., treating the dust and air as a multimaterial ensemble) will need to be considered. However, whatever approaches are taken, the particles should be represented by more than one particle class, since the thermal heating and subsequent affect on air blast flow fields will be significant.

SECTION 8

REVIEW OF SHOCK TUBE FACILITIES FOR APPLICATION TO M-X SHELTER AIR BLAST LOADS PROGRAM

8.1 SHOCK TUBE CAPABILITIES

A shock tube provides a convenient, versatile laboratory tool to study transient gas dynamic phenomena. The operation of a shock tube is eaily illustrated by considering a constant diameter tube divided into two regions: a high pressure driver section and a lower pressure driven section separated by a diaphragm (Figure 16a). When the diaphragm is burst, a shock wave propagates down the driven section, and an expansion fan propagates back into the driver section (Figure 16b). The expansion fan converts the stagnation energy of the driver gas into the flow energy of the expanded driver gas and the work done in compressing and accelerating the driven gas. Expansion waves travel at the speed of sound relative to the local driver gas conditions; thus, the driver gas sound speed is an important parameter in creating strong shocks.

Using the notation of Figure 16 the ideal shock strength is determined (Reference 56 and 57) from

$$P_{41} = P_{21}\left\{1 - \left(P_{21}-1\right)\left[\frac{\left(\frac{\gamma_4-1}{2\gamma_4}\right)C_{V14}\ T_{14}}{\left(\frac{\gamma_1+1}{\gamma_1-1}\right)P_{21}+1}\right]^{1/2}\right\}^{\frac{2\gamma_4}{1-\gamma_4}} \qquad (37)$$

where the double subscript implies a ratio. The shock Mach number is

$$M_s = \left\{\frac{\gamma_1-1}{2\gamma_1}\left[1 + P_{21}\left(\frac{\gamma_1+1}{\gamma_1-1}\right)\right]\right\}^{1/2} \qquad (38)$$

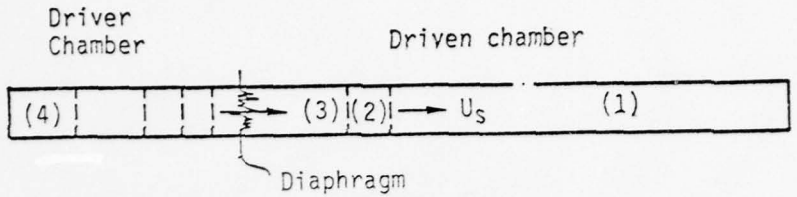

Figure 16a. Shock tube schematic

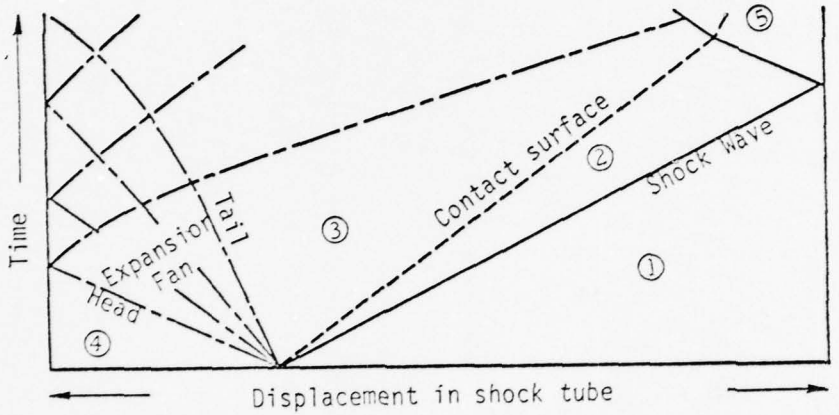

Figure 16b. Shock tube x-t diagram

and the Mach number behind the shock is

$$M_2 = \left(\frac{P_{21}-1}{\gamma_1}\right)\left\{\frac{\gamma_1-1}{2\gamma_1}\ P_{21}\left(\frac{\gamma_1+1}{\gamma_1-1}\ +\ P_{21}\right)\right\}^{-1/2} \tag{39}$$

The shock induced velocity is

$$\frac{U_2}{a_1} = \left(\frac{P_{21}-1}{\gamma_1}\right)\left\{\frac{\gamma_1-1}{2\gamma_1}\ \left[\left(\frac{\gamma_1+1}{\gamma_1-1}\right)\ P_{21}\ +\ 1\right]\right\}^{-1/2} \tag{40}$$

and by continuity

$$\rho_{21} = U_{s/}(U_s - U_2) \tag{41}$$

Real gas effects become important for shocks on the order of 1000 psi in air due to dissociation, and these effects are accounted for in the charts of Reference 56.

The ideal strong shock limit for a simple air/air shock tube is found from Equation 37 which reduces to

$$P_{21}^2\ -\ 2\ \left(1 + \frac{\gamma(\gamma+1)}{(\gamma-1)^2}\right)P_{21}\ +\ 1\ =\ 0 \tag{42}$$

for an infinite driver pressure. For $\gamma = 1.4$ Equation 42 has the solution $P_{21} = 44$ or $P_2 = 650$ psi.

Equation 37 can be rewritten as

$$\frac{P_{21}}{P_{41}} = \left\{1 - \left[f\ (\gamma_1,\gamma_4)\ C_{V14}\ T_{14}\ P_{21}\right]^{1/2}\right\}^{\frac{\gamma_4-1}{2\gamma_4}} \tag{43}$$

which indicates that high shock strengths can be achieved by employing a low molecular weight gas such as hydrogen or helium in the driver section ($C_V \propto M_w^{-1}$) or by heating the driver gas. Figure 17 gives some example performance characteristics for air/air, helium/air and heated ($T = 16{,}000^{\circ}R$) helium/air shock tubes.

Since it is not practical to maintain a driver gas at extremely high temperatures for long periods of time, it is desirable to instantaneously heat the gas just before the diaphragm is burst. One reliable, economic and efficient method for rapidly heating the driver gas to extremely high temperatures is by the discharge of an electric arc through the driver chamber. The potential for the arc is obtained by use of a capacitor bank, and the arc is initiated by a small starter wire. Such shock tubes have produced shock Mach numbers of 15 (P_2 ~4000 psi) in atmospheric test sections.

Combustible driver gases also have been used to produce high shock strengths. Hydrogen/oxygen mixtures can produce a shock Mach number of 8.5 (P_2 ~1200 psi) in an atmospheric test section. Hydrogen presents a safety hazard so extreme care must be taken in its use. A third alternative is explosive drivers. In this approach, the driver section is collapsed by an exterior explosive loading, and the collapsing cylinder drives a shock wave into the driven section. Explosive driver shock tubes have produced shock Mach numbers of 20 (P_2 ~8000 psi) in an atmospheric test section.

8.2 SHOCK TUBE FACILITY SURVEY

A brief survey was conducted to identify shock tubes to measure airblast loads on scaled models of the M-X shelter. Simulation criteria were established and ordered to enable objective selection of the most advantageous facility. The criteria are:

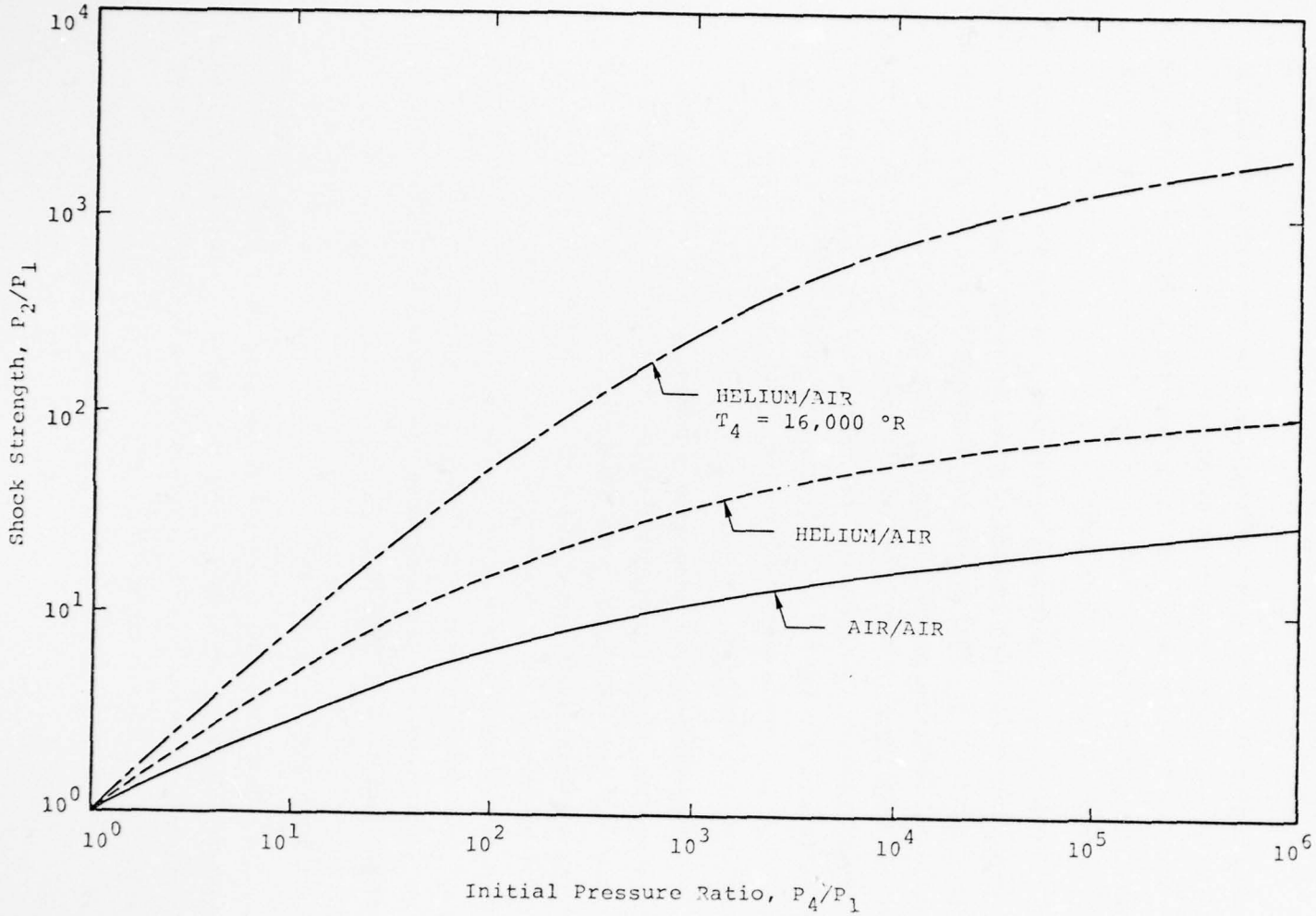

Figure 17. Shock strength vs. initial pressure ratio

- Shock overpressure ≃ 600 psi in stmosphere
- Large test section
- Availability
- Turnaround time
- Cost
- Location

The first requirement eliminated most laboratory shock tubes, but is deemed necessary since shock loading phenomena may be absolute value dependent (Reference 58). A large test section is required to accommodate the maximum size model. Turn around time and availability are important considerations in order to meet time urgent M-X development schedules (e.g., DABS S-2, S-3 test dates).

Five laboratory shock tubes were located which meet the general selection criteria. These are located at CALSPAN, BRL, NASA Ames Research Center and CERF. The Physics International (PI) Shock Tube is also considered.

CALSPAN has a 6-inch I.D. and an 8-inch I.D. shock tube. The heated hydrogen driver sections produce a shock overpressure of approximately 600 psi in an atmospheric test section (Reference 59). The BRL High Pressure Shock Tube is driven by the detonation of hydrogen/oxygen mixtures. Shock waves in excess of 1000 psi have been generated in the 8-inch test section; the overpressure is in excess of 175 psi in a downstream 22-inch test section (References 60 and 61.

The NASA Electric Arc Shock Tube should be able to achieve overpressures of 2000 to 4000 psi in a 4-inch I.D. atmospheric test section (Reference 62); however, atmospheric tests have not been run. Energy for the driver is supplied by a one megajoule capacitor storage system. CERF has a 13-inch I.D. shock tube capable of approximately 550 psi overpressure in atmosphere at the present test section location (Reference 63). The driver section contains a hydrogen/oxygen mixture

which is detonated by 14 spark plugs. Higher overpressures in atmosphere can be obtained by moving the test section closer to the driver. Higher shock strength ($\frac{\Delta P}{P_a}$) can be obtained by evacuating the driven section.

On the basis of the selection criteria, the CERF 13-inch Shock Tube is superior to the other laboratory shock tubes because it has the largest test section (for a 600 psi overpressure) and because it is located near the AFWL. The remaining criteria are generally matched by all of the facilities, although contractor facilities may be more expensive than non-profit or government facilities.

The PI explosive driver shock tube needs to be assessed in a different light. Overpressures on the order of 8000 to 15000 psi can be achieved in a small diameter atmospheric test section, and these shocks could be expanded into a fairly large test section at reduced (but still quite high) overpressures. The PI facility currently has a cylindrical driven section capable of withstanding 5000 psi which transitions into a 1 foot wide by 3 foot high by 20 foot long rectangular test section capable of withstanding 1000 psi shocks (Reference 64).

The PI facility has some unique capabilities, but there seems to be no reason to select it over the CERF 13-inch Shock Tube. Overpressures higher than can be achieved at CERF (1200 psi) are not required for shelter tests. A larger shelter model might be mounted on the 3 foot wall of the existing test section, but a greater increase than this would be required to justify the additional cost (expendable driver sections) and turnaround time (1 shot per week versus 3-4 per day). Finally, the CERF facility has the advantage of proximity to AFWL while the PI facility is at a remote site in Traci, California.

SECTION 9
RECOMMENDED TEST PROGRAM

SAI recommends a laboratory program to measure air blast loading in support of the M-X shelter design effort. The combination of laboratory experiments, code calculations and large scale proof tests will provide a basis for confident prediction of M-X shelter loads.

A series of shock tube tests are suggested using scaled models of the M-X shelter. The suggested program philosophy is directed towards sound experiments using simple reliable diagnostics so as to guarantee quality data. Standard shock tube techniques should be employed for classical waveforms and a technique developed to produce clean precursor waveforms. M-X shelter air blast loading histories could be synthesized from the shelter loads data.

We recommend that the shock tube test program be conducted at the CERF Thirteen Inch Shock Tube. The CERF shock tube was selected over other candidate shock tubes because of its large test section, its ability to produce a 600 psi shock in atmosphere, and because of its proximity to AFWL.

In the event that the CERF shock tube is not available, the tests could be conducted in the 22 inch section of the BRL High Pressure Shock Tube. The BRL tube has the advantage of allowing larger models; sizes quoted in the following discussion could be increased by the ratio 22/13. Since the BRL shock tube cannot provide a 600 psi overpressure wave into atmosphere (the limit is about 170 psi), the test section could be pumped down to 4 psi such that the criteria incident shock pressure ratio is reproduced. This procedure is not as desirable as conducting the tests at atmospheric pressure, but is meaningful since the numerical calculations can be made for both conditions.

The scale of the experiment is dictated by the internal diameter of the CERF shock tube. With a tube diameter of 13 inches, the shelter model would be scaled down by a factor of 1000. This would allow shelter model rotation to any incidence angle within the test section, and the model would be small enough to avoid wall interactions during shock transit. Both the shelter berm and the ramp should be simulated.

The recommended approach is to measure the shock loading on the major faces of the model. Initial choices of model orientation could be (1) head on, (2) side on, and (3) 40 degrees incidence, although the test design allows any incidence angle. Both classical and precursor waveforms should be tested.

9.1 SHOCK TUBE EXPERIMENT DESIGN-CLASSICAL WAVEFORMS

M-X shelter shock loading should be measured using a scaled model of the shelter supported on a ground plane spanning the shock tube centerline. The shelter model we recommend (Figure 18) is approximately 7½ inches long (including the ramp), and the shelter model roof protrudes approximately 1/4 inch above the ground plane. This model size (1/1000 scale) was chosen to avoid shock tube wall interference (the vertical clearance must be at least seven times the roof height to avoid bow shock reflection according to AFWL/DYM calculations) and to allow the complete model to be rotated to any angle within the shock tube (the rotation requirement dominates). When the model is in the head-on position, the shelter edges are approximately 1.5 shelter widths (15 shelter heights) from the shock tube walls. When the model is in the side-on position, the shelter end is approximately one shelter width from the closest wall. The shelter model above grade blockage ratio is only about 1 percent, which is more than adequate from steady flow considerations.

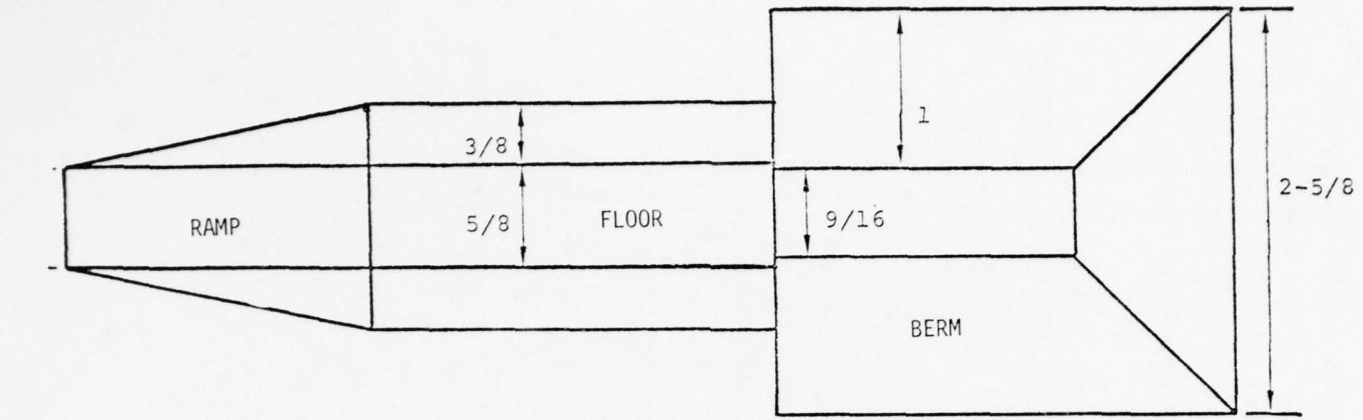

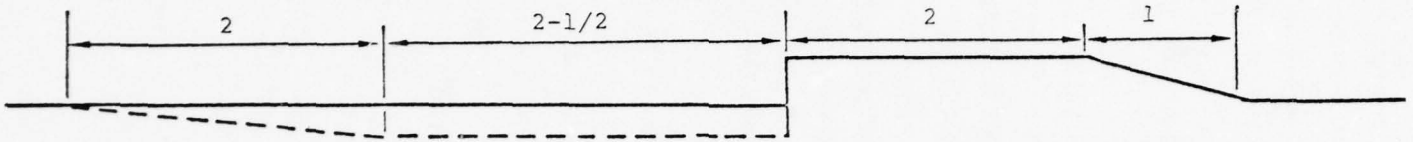

NOTE: MODEL DIMENSIONS IN INCHES

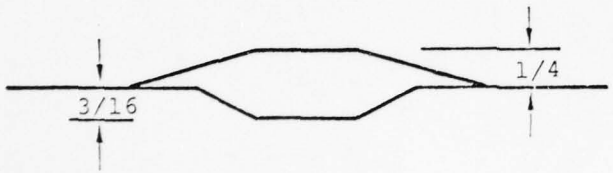

Figure 18. Shelter model dimensions

Model construction and mounting is a key part of the experiment design. We recommend that the experimenter build a knife edge ground plane (18 inch by 13 inch x 2-3/4 inch) spanning the circular shock tube (Figure 19). The shock wave will then propagate over the ground plane in the classical fashion. Bolt holes are already available in the shock tube centerline to mount the ground plane which will probably be inverted for easy access.

The shelter model should be machined as an integral part of a round insert (Figure 20) which we recommend be secured to the ground plane in the desired model orientation by eight half inch Allen head bolts. A similar insert on the ground plane backside would cover the area housing the pressure transducers. All bolts and pressure transducers would be mounted from the backside to preserve the model surface. Model orientation can be changed by simply loosening the eight Allen head bolts and rotating the inserts. Instrument cables would be routed through the ground plane and passed out of existing ports in the side of the shock tube.

The shelter model should be mounted towards the back of the ground plane to assure that a clean shock wave strikes the model. The ramp leading edge should be six inches behind the ground plane leading edge, and the shelter door should thus be $10\frac{1}{2}$ inches from the leading edge (in the end-on position). Figure 21 demonstrates the recommended model orientations.

Shock pressure could be measured forward of the ramp, on the floor, on the door, on the roof, on the side walls on the end, and beside the shelter (e.g., Figure 22). The recommended transducer mounting geometry is indicated in Figure 23. Repeat tests should be required with some transducers (e.g., in the door) interchanged because of the size of transducers.

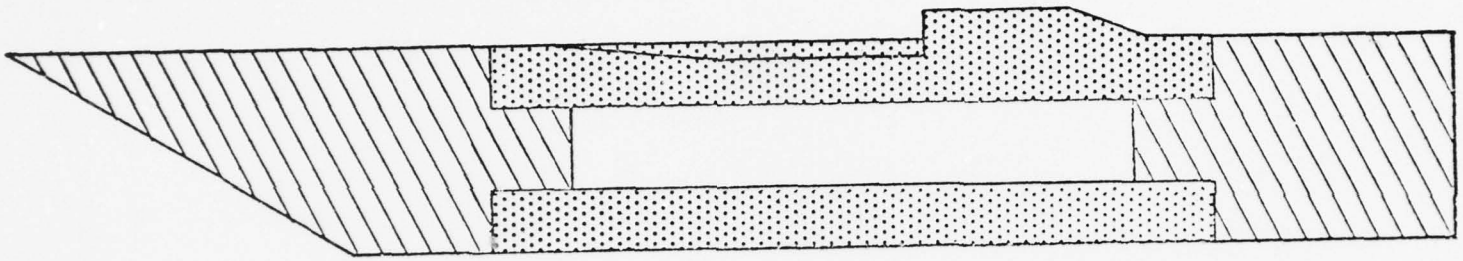

1/2 SCALE

Figure 19. Shock tube ground plane cross-section

AD-A064 149 SCIENCE APPLICATIONS INC MCLEAN VA F/G 18/3
THEORETICAL AIR BLAST LOADING ESTIMATES ON THE M-X SHELTER, THE--ETC(U)
JUN 78 B S CHAMGERS, D T HOVE, R I ISSA DNA001-77-C-0059
UNCLASSIFIED SAI-78-503-AO DNA-4610F NL

2 OF 2
AD
A064149

END
DATE
FILMED
3-79
DDC

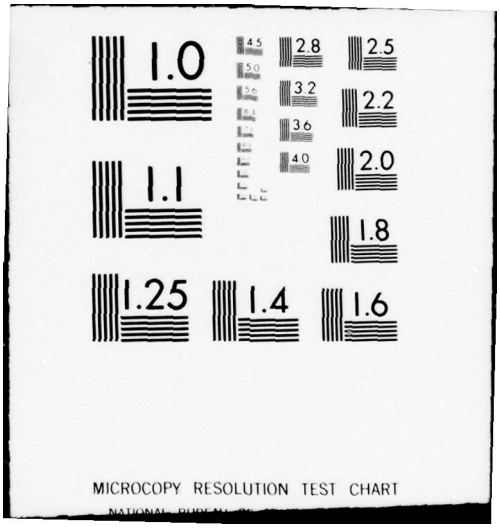
1.0
1.1
1.25
1.4
1.6
1.8
2.0
2.2
2.5
2.8
3.2
3.6
4.0
4.5
5.0
MICROCOPY RESOLUTION TEST CHART

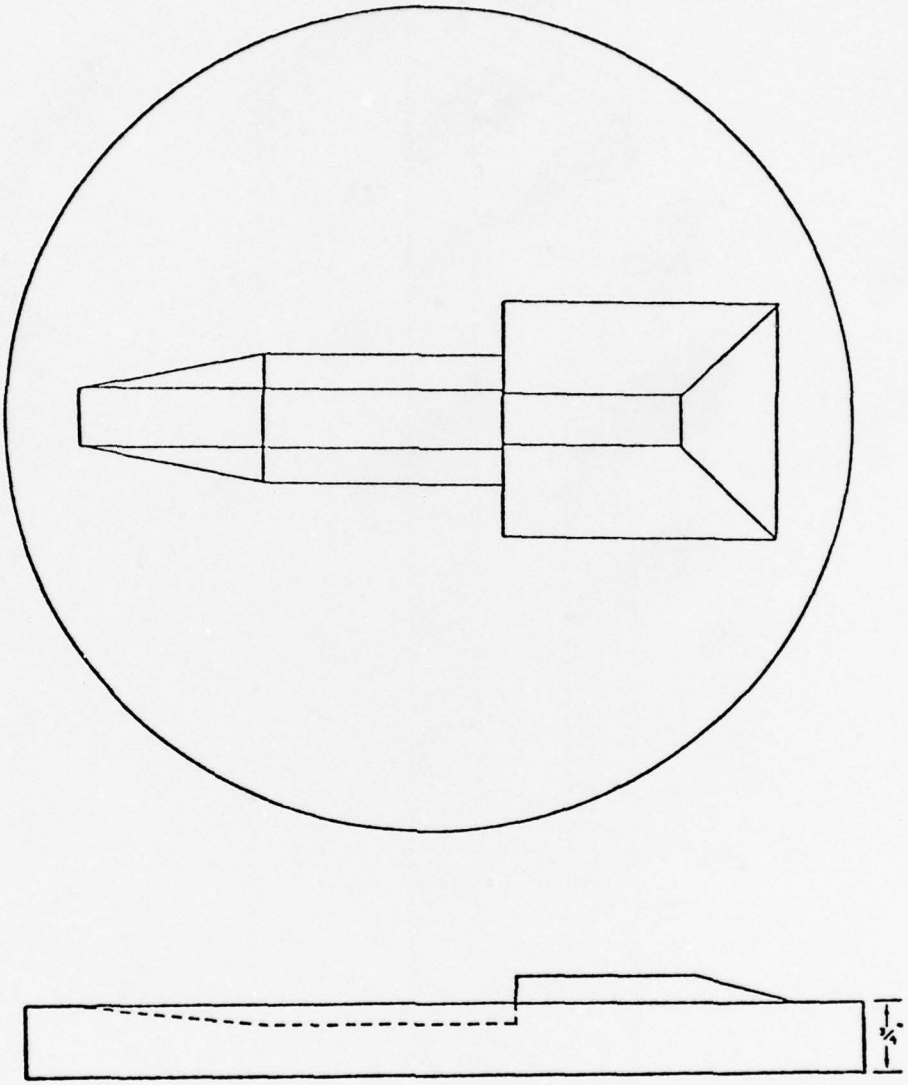

Figure 20. Test model insert

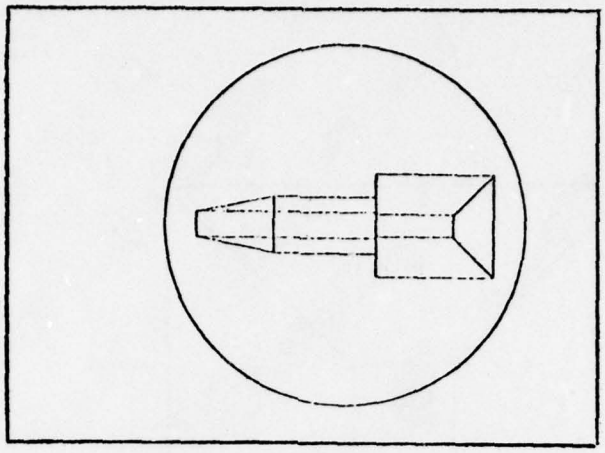

(a) END-ON INCIDENCE

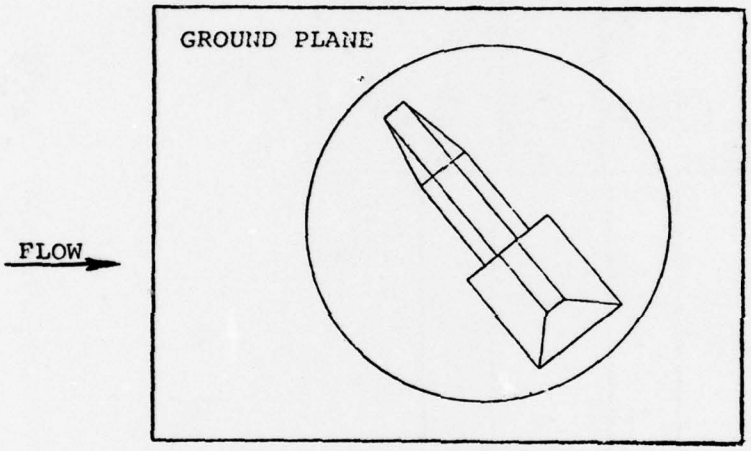

(b) 40 DEGREE INCIDENCE

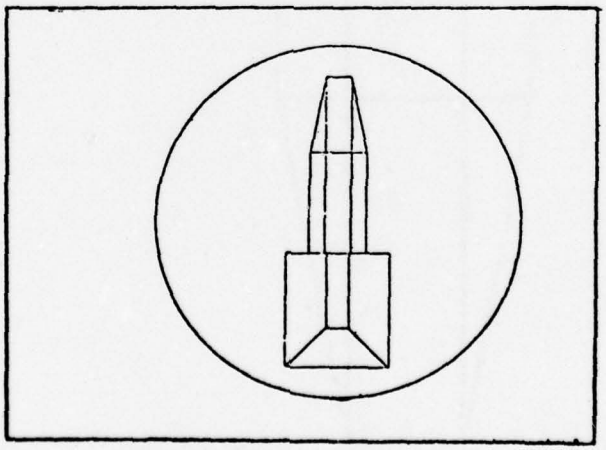

(c) SIDE-ON INCIDENCE

Figure 21. Selected model orientations

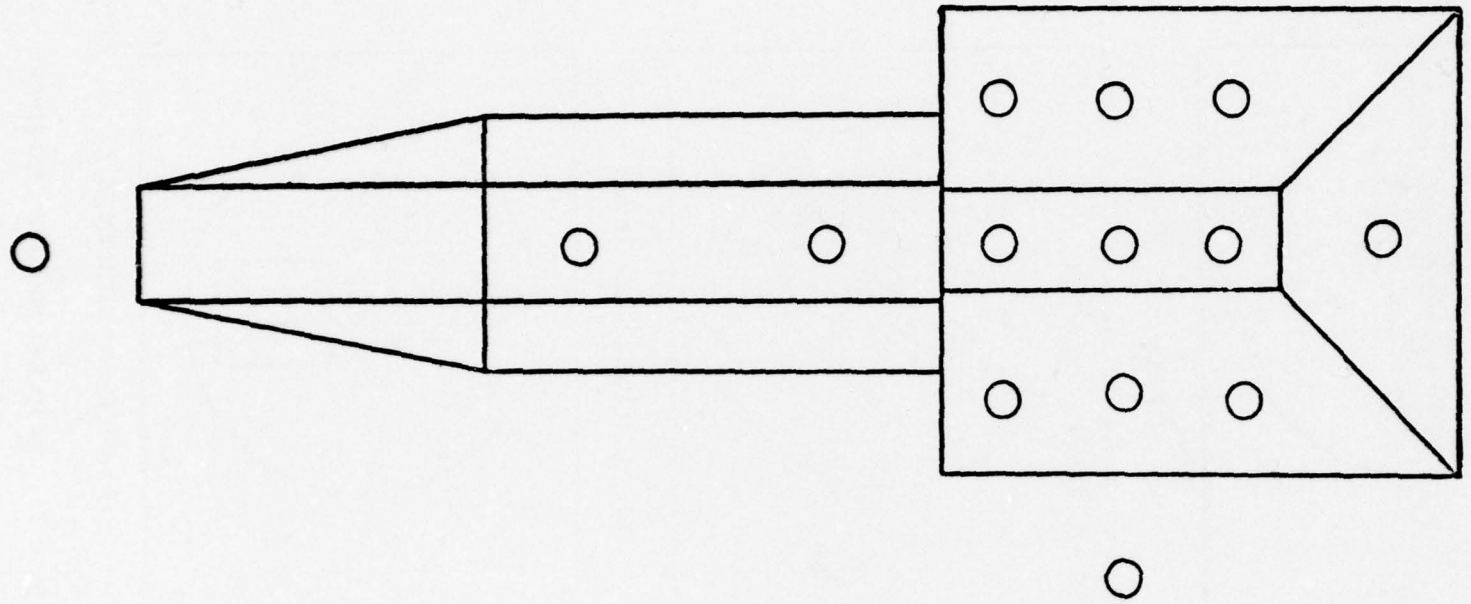

Figure 22. Pressure transducer locations

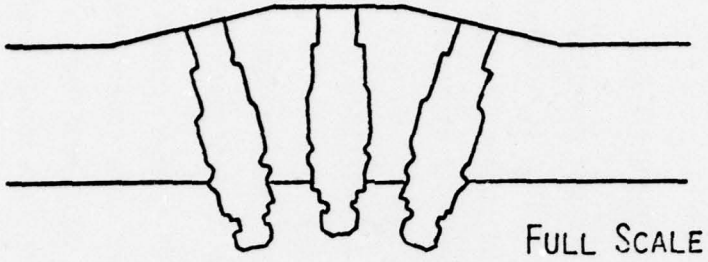

Figure 23. Example transducer installation

The model and ground plane could be constructed out of 250,000 psi ground Maraging steel. This material is easy to machine in its soft state but becomes very hard when heat treated to 500°F. A $\sqrt{32}$ surface finish if specified on the ground plane and model surface will avoid unduly influencing the pressure distributions. The boundary layer thickness is expected to be on the order of 70 mils for a one foot travel, so excessive surface roughness could change the flowfield. Material hardness is required to maintain the surface finish during handling and impingement of shock tube debris.

9.2 SHOCK TUBE EXPERIMENT DESIGN - PRECURSOR WAVEFORMS

Precursor waveforms for nuclear bursts are generated due to the higher sound speed in a heated (~1000°K according to Reference 23) air layer ahead of the shock wave. Experience on nuclear events indicates that the shock wave in the heated layer propagates at about the same speed as the primary shock, but because the shock Mach number is lower, the pressure immediately behind the shock is lower than for the primary wave. A series of secondary shocks eventually returns the pressure to (nearly) the freefield value, but the process produces an extended rise time. An analytical model of this phenomena is described in Appendix A.

Precursor waveforms have been studied through numerical hydrocode calculations, such as at the AFWL. SHELL and more recent HULL code calculations (References 2, 3, 65 and 66) have confirmed that a precursor can be caused when energy is deposited in near surface zones thereby raising the air sound speed. An AFWL calculational program is currently underway; but it is not clear when the predictions will be available.

To create precursor waveforms in a shock tube, it is necessary to provide a layer of higher sound speed gas next to the surface. This has been accomplished by heating the gas or by substituting alternate low molecular weight gases. Griffith (Reference 67) and Gion (Reference 68) chose to heat a flat plate and rapidly insert the plate into an open end shock tube. Several authors (Reference 23) created precursors

by running shocks into various gases. With the exception of Gion, the previous experiments are at least 20 years old and all were for low ($\Delta P<100$) incident overpressures. Instrumentation was limited to optical measurements of the precursor structure. The present program proposes to create precursor waveforms at 550 psi incident overpressure and to measure the pressure waveforms and shelter loads.

A sample of a fit to experimental data on precursor waveforms indicates a toe to peak pressure ratio of 1:10. Based on the analysis of Appendix A, this could be accomplished by heating the air to $>1000^{o}K$ or by substituting a light gas such as Helium (Figure 24) near the surface of the ground plane described in Section 9.1. This provides an increase in sound speed by factors of 2 to 3. As the shock tube wave strikes the layer, the precursor toe will race out ahead of the incident shock in a transient process until a "quasi-steady situation" is achieved. Griffith found that the distance required was about 10 times the layer thickness and that the precursor toe length was about 2 layer thicknesses. The height of the precursor has been observed to be on the order of the layer thickness (Reference 23). Thus, by making the high sound speed layer one inch high, the precursor should have time to develop, the entire scaled model will be engulfed by the precursor, and any interface problems (e.g., thin diaphragm) will not affect the shelter loading.

Heating the gas layer to $\sim 1000^{o}K$ does not seem to be a viable concept. If the ground plane were instantaneously heated to $1000^{o}K$ and held there, the air layer would be heated by conduction, and the temperature profiles (Figure 25 are given by

$$\frac{T-T_o}{T_p-T_o} = 1 - \text{erf}\left(\frac{y}{\sqrt{4\alpha t}}\right) \qquad (44)$$

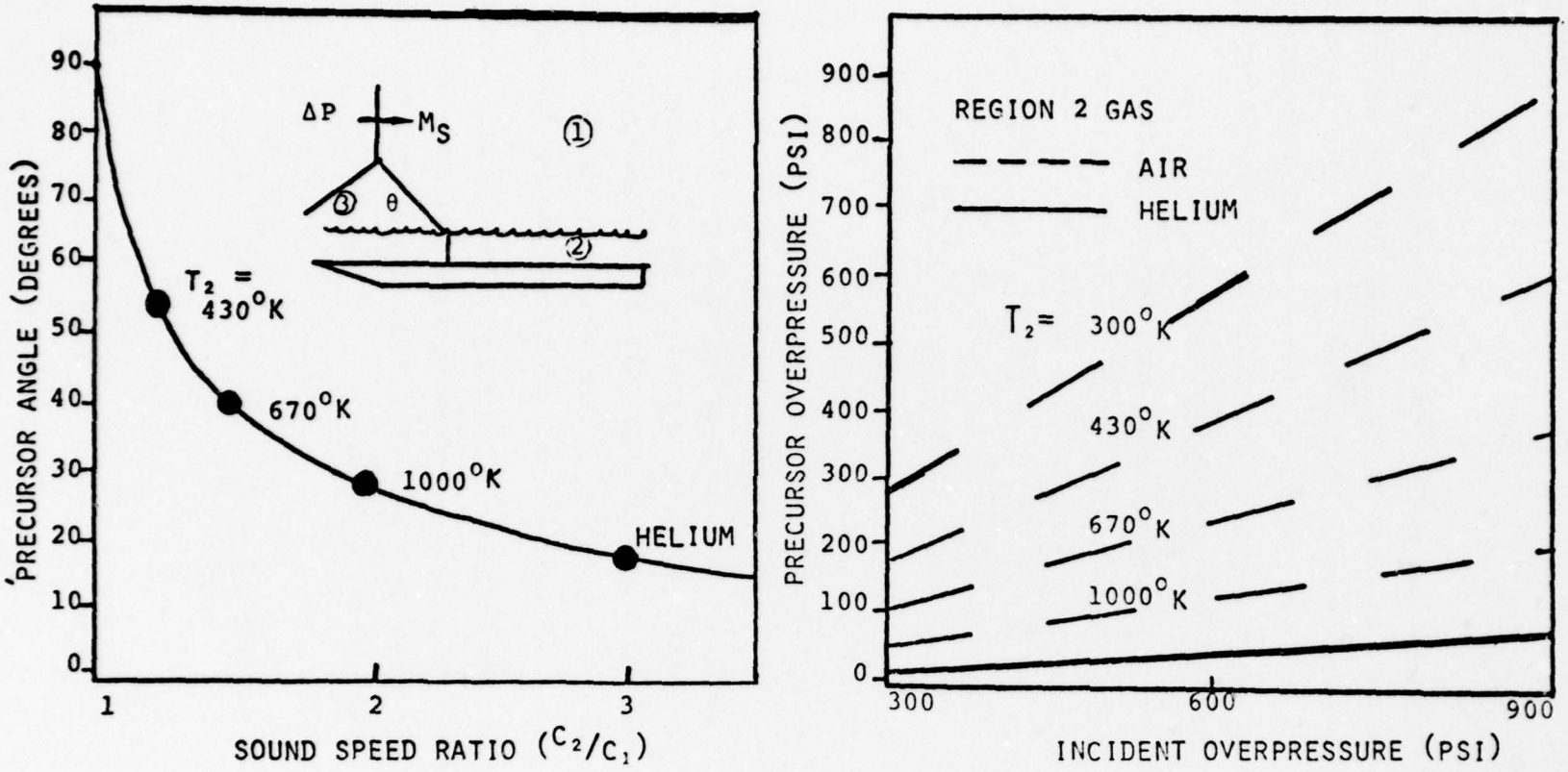

Figure 24. Precursor formation in CERF shock tube

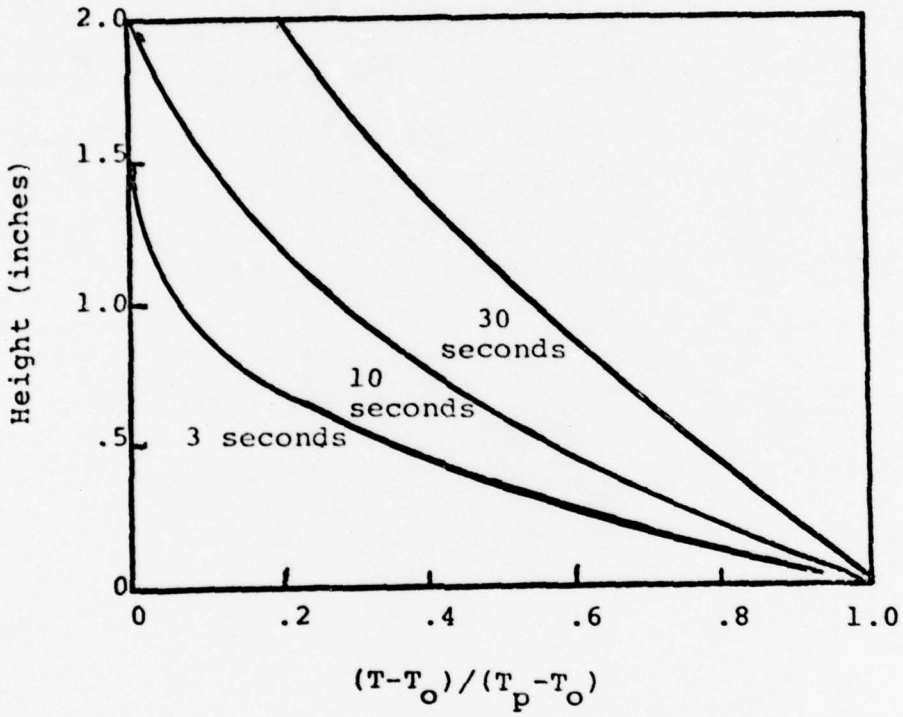

Figure 25. Heated air layer temperature profiles

where T_o is the initial air temperature (300^oK), T_p is the plate temperature, y is height above the plate, $\alpha = \left(\frac{k}{\rho c_p}\right)$ is the thermal diffusivity of the air and t is time (Reference 69). The quantity $\sqrt{\alpha t}$ is a characteristic thermal penetration distance

$$\frac{T-T_o}{T_p-T_o} \simeq 1/2$$

which for air is $y \sim \sqrt{0.04t}$ where y is in inches and t is in seconds.

If we wish to confine most of the heat to a layer 1 inch thick, the plate would have to be heated in a time small ($\tilde{<}0.1$) compared to 10 seconds. For a uniform heating of the steel ground plane to a temperature of 1000^oK in one second, the total heat required is

$$q = m C_p \Delta T \tag{45}$$

$$= 200 \text{ (lbs)} \; 0.1 \left(\frac{BTU}{lb\,^oF}\right) 700 \; (^oK) \; \frac{5}{9} \left(\frac{^oF}{^oK}\right) 252 \left(\frac{cal}{BTU}\right)$$

$$\simeq 2 \times 10^6 \text{ cal}$$

and the power requirement (100 percent efficiency) is

$$\dot{q} = \frac{q}{\Delta t} \tag{46}$$

$$= \frac{2 \times 10^6}{1} \left(\frac{cal}{sec}\right) 4.186 \left(\frac{joules}{cal}\right)$$

$$\simeq 8.4 \text{ MW}$$

which is a considerable amount indeed. Gion solved this problem by slowly heating the plate and rapidly inserting the plate into the (low overpressure) shock tube; at CERF the shock tube must remain closed.

An alternate method not requiring as much energy is flash heating the surface of the ground plane. A small version of the SAI Flashbulb could deliver 200 cal/cm^2 sec for about 100 msec (Reference 70). The surface temperature of the plate would be

$$T\ (y=o) = \frac{2\phi}{k}\sqrt{\frac{\alpha t}{\pi}} \tag{47}$$

where ϕ is the surface flux and k is the material conductivity. For a steel ground plane the maximum surface temperature would be

$$T(y=o) = \frac{2x200\left(\frac{cal}{cm^2 sec}\right)\sqrt{\frac{0.1x0.1\ (cm^2)}{\pi}}}{0.124\ \left(\frac{cal}{sec\ cm\ ^oK}\right)}$$

$$T(y=o) \simeq 180^oK$$

The coupled flux would have to be 5 times higher or 30 times longer to achieve the desired surface temperature.

The energy requirements might be reduced by laminating a thin layer of nonconducting material under the surface of the ground plane, but cost and strength requirements would seem to override. Furthermore, there are other problems associated with heating the ground plane. The melt temperature of steel is about 1800^{o}K so strength properties would be seriously degraded at temperatures greater than 1000^{o}K. Thermal expansion $\left(\beta \simeq 10^{-5}{}^oK^{-1}\right)$ would require a mounting system capable of dealing with at least 0.13 inches of lateral expansion. Finally, high frequency piezoelectric pressure transducers (Section 9.4) to be mounted in the plate are quite temperature sensitive.

A more viable way of achieving the high sound speed layer is through the use of alternate gases. The speed of sound for a γ-law gas is given by

$$c = \sqrt{\gamma RT} \tag{48}$$

Consequently, the sound speed can be increased by increasing γ or by decreasing the molecular weight $\left(R = \frac{R}{m}\right)$. Helium is a good possibility ($\gamma = 1.67$, $m = 4$), but Ausherman (Reference 71) pointed out that a more direct simulation could be achieved by using a mixture of hydrogen and nitrogen. Since both gases are diatomic, $\gamma = 1.4$ as in air. The mass fraction of hydrogen which simulates the sound speed of air at a temperature T_a is given by

$$X_H = \frac{T_{ao}\, m_{Na} - 1}{m_{NH} - 1} \tag{49}$$

where m is the molecular weight and the double subscript implies a ratio. Here a refers to air, N refers to nitrogen and H refers to hydrogen. The sound speed of a precursor hot layer $\left(T_2 \sim 1000^{o}K\right)$ can be achieved easily (Figure 26) and with a great deal of control.

The method of creating the alternate gas layer requires development during the program. Three methods are suggested here. Gases supplied by high pressure bottles (at the appropriate flow rates) could be mixed in an exterior container and injected through a porous surface on the ground plane. The instrumentation area shown in Figure 19 would double as a plenum chamber. With the ground plane inverted, the gases would be stable and mix with the surrounding air by diffusion only. In fact, by varying the shock arrival time and flow rates, the concentration profiles and layer heights could be adjusted.

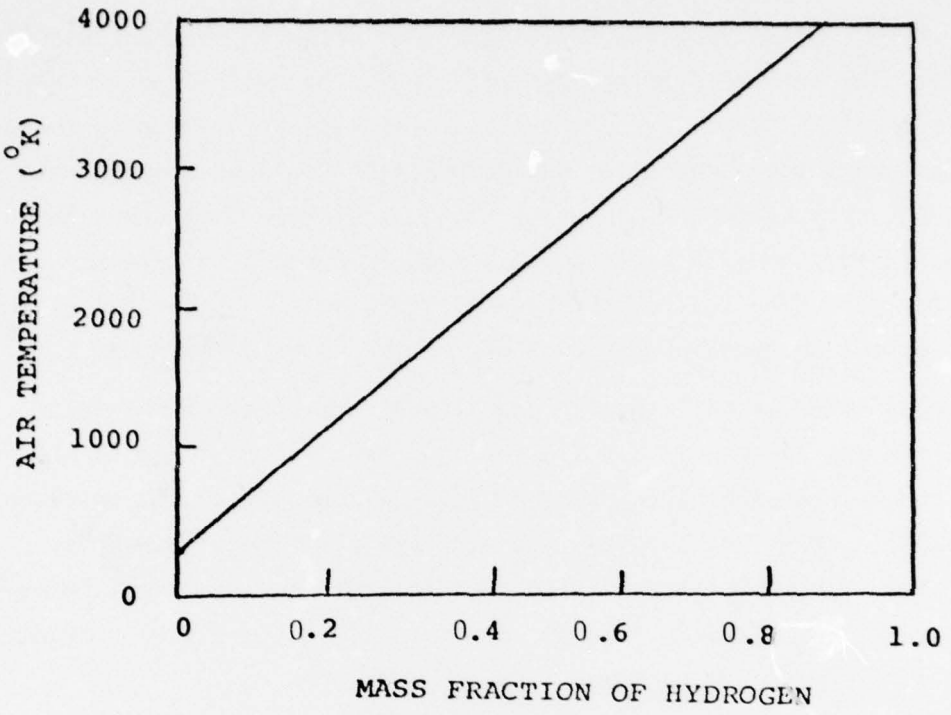

Figure 26. Equivalent air temperature for a hydrogen/nitrogen mixture

Porous metal plates are available commercially with a controlled porosity. The structure of the gas layer could be determined for various plates, flow rates, etc. in a simple laboratory setup which reproduces the shock tube geometry. Gas composition could be sampled with a high frequency concentration probe (Reference 72). Thus, once the model is in the shock tube, it would only be necessary to regulate the flow rates according to the laboratory calibrations. The effect of the porous surface on shock propagation would have to be determined.

Two other methods involve lightweight diaphragm materials to contain the gas layer. In the simplest approach a bag of gas is placed in the shock tube under the inverted ground plane and is held in place by buoyancy. Objections to this approach are that the bag material, even though lightweight and flexible, could influence the shock formation and, perhaps more importantly, could impact the pressure transducers disrupting the pressure signals.

An alternate containment method which eliminates the diaphragm just before shock (model) arrival is being used by Shih of SAI in the AEDC Ballistic Range G. A thin elastic material is stretched over the region being contained (50 gallon drums) along with a thin heated element. At a calibrated time before firing the element is heated, the diaphragm bursts and the tension causes the diaphragm to be pulled away. In the shock tube, the material would be stretched across the tube about an inch below the ground plane and the gas mixture added from the side through a purging process.

9.3 SHOCK TUBE INSTRUMENTATION

Shock wave propagation in the shock tube can be determined by measuring the shock front pressure or the shock speed from which pressure can be determined. SAI recommends that both measurements be made using high frequency quartz pressure transducers and ionization probe time of arrival (TOA) gauges. The same type of pressure transducers could be used on the model.

PRECEDING PAGE BLANK

Tentatively, the PCB Piezotronics model 113A22 quartz pressure transducer to measure shock pressure is recommended. This low impedance, high frequency (1 μsec rise time) transducer employs state-of-the-art integrated circuit technology to provide a simple, reliable instrument for shock tube type pressure measurements. The frequency resolution ~1 MHZ is adequate for the most severe model loading conditions expected. For the head on case, the shock, will be reflected up to 4440 psi on the door and will decay in 18 μsec to 1280 psi with six microseconds delay before the first rarefaction waves arrive at the center of the door. Not only will the peak pressure be well defined (the data analysis will synthesize the rise as a discontinuity) but the transducer will easily follow the pressure decay (i.e., the decay time is long compared to the transducer rise time). In terms of the protype, the decay time will be on the order of 18 msec, and the present experiment will have a scaled time resolution on the order of a msec which again is more than adequate.

The model 113A22 pressure transducer has a 1 to 5000 psi dynamic range with a 5 volt full scale output. Complications associated with charge amplifying systems are eliminated, and the transducers have proved successful in numerous Quartz gauges are temperature sensitive in some applications, but this can be overcome by covering the diaphragm with black plastic tape or RTV. The small diaphragm area (0.218 inch diameter) allows high resolution, and in fact, the transducer could double as a time of arrival gauge. Mounting is by a 3/8-24 thread or a press fit to a 0.25 inch diameter shoulder. Ringing has been suppressed in the transducer design, so special mounting is not required.

Pressure transducer output (voltage) and TOA signals should be appropriately recorded (e.g., a high speed tape recorder). Transducer output will be 1 to 5 volts so signal to noise ratio should be no problem.

9.4 SHOCK TUBE TEST PLAN

Some initial shock tube calibration tests (Series 1) are recommended to assure that desired pressures in the test section can be reproduced. Typical desired performance characteristics are pressures within 5 percent with a 95 percent probability of success. Approximately four tests would be appropriate (one high, one low, two on) to zero in on the desired incident pressure in an empty test section. The next two shots could be conducted with the model support mechanism in place to determine if the flow field is perturbed. Finally, two shots are recommended to be conducted with the model in place with a minimum of instrumentation as a shakedown test. The initial setup and checkout should take two weeks.

Series 2 would test the shelter loads for classical waveforms. The model would be tested first in the head-on position with emphasis on instrumentation of the door. One transducer would measure the incoming wave, two transducers would measure the wave as it propagates along the floor, two others should be located in the door, and finally several other transducers should be located in the major faces of the model. Approximately six tests are recommended in the chosen schedule to get clean repeatable measurements for these first model tests. Three shots would then be conducted for the model in the side-on position with the transducer layout shown in Figure 22. Finally, three shots should be conducted with the model in the 40 degree orientation.

Both the head-on and side-on model orientations should be conducted for the Series 3 precursor experiments. Five shots would be required over a plane surface to diagnose and tune the precursor wave (two shots adjusting the pressure, two shots adjusting the layer, one shot for verification). Three shots would be conducted for each orientation with the model in place.

Four shock tube tests are recommended to be reserved on a contingency basis. These shots would be used to cover failures, to fill in gaps, or to investigate unusual phenomena.

Table 7 summarizes the recommended test series. At least two successful shots at each model orientation are desired. The tests would be considered successful if the incident overpressures scatter less than ± 5 percent and the measured loads scatter less than ± 20 percent. It is possible that the precursor waveforms will show more scatter than this.

It is estimated that the entire program could occupy six weeks of testing time including the two weeks of setup and calibration (Table 8). The estimate is based on three shots per day for the classical waveforms and two shots per day for the precursor waveforms in addition to time for each test section change. A contingency of four shots is recommended to resolve issues surfacing during the test program.

9.5 SHOCK TUBE DATA ANALYSIS

Output from the pressure transducers should be converted to pressures via the calibration curves for each transducer. Both shock front values and pressure profiles would be determined from the Polaroid photographs. Shock front velocities determined from the TOA gauges along the tube could be converted to shock front pressures via equation 46 or the curves available in Reference

Pressure loading data should be compared with numerical calculations (Section 9.6), the engineering estimates from earlier sections of this report, and previous DABS experimental data. Air blast loading histories should be synthesized. Precursor waveforms should be characterized in terms of surface pressure histories and shock structure (if optics were available).

Table 7. Summary test matrix

SERIES	NUMBER	OBJECTIVE	PROBABLE NUMBER OF SHOTS
1	1	Set up/Calibration	8
2	1	Classical, Head-On	6
2	2	Classical, Side-On	3
2	3	Classical, 40 Degrees	3
3	1	Procursor Calibration	5
3	2	Precursor, Head-On	3
3	3	Precursor, Side-On	3
4	1	Contingency	4
			35

Table 8. Shock tube test schedule

TEST	WEEKS					
	1	2	3	4	5	6
1	—	—				
2-1			—			
2-2			—			
2-3				—		
3-1				—		
3-2					—	
3-3						—
4						—

9.6 THEORETICAL SUPPORT

Design of the experiment (especially the precursors) and interpretation of measured results can be greatly aided by numerical calculation of the flow fields. For the classical waveforms, it would be desirable to have a calculation of the flow field over the knife edge ground plane and model to verify that the plane does not disturb the flow and that wall reflections do not interfere. These calculations should be performed by the end of the second week to be useful to the program.

Theoretical calculations would also be of assistance in designing the precursor experiment. Precursor shape, static pressure histories, and dynamic pressure histories are needed. Of particular importance is whether the precursor waveform has reached a "quasi-steady" profile by the time it arrives at the shelter model. Alternate methods of generating the precursor layer should be investigated theoretically to determine which methods most adequately simulate the nuclear precursor shapes.

SECTION 10

SUMMARY AND CONCLUSIONS

10.1 SUMMARY AND CONCLUSIONS FOR AIR BLAST LOADS

An engineering approach was employed to estimate the loads on an M-X Shelter resulting from side-on and end-on incidence of 600 psi peak-pressure blast waves.

Both classical and precursor waveforms were considered. The usual quasi-steady method of calculation was not used for the slant faces since it was found to be inapplicable. An approach in which a reflection factor is determined at each deflection point and in which the whole pulse is scaled by that factor, was used instead.

The calculations show good overall agreement with finite-difference computations and experimental data for the classical shock case. For the precursor waveform, the manner in which the pulse is reflected is not well known and the present calculations can only serve as a guideline. Numberical solutions of the exact equations and/or experiments are required to verify the calculations.

10.2 SUMMARY AND CONCLUSIONS FOR INFLUENCE OF DUST

Existing dust lofting models have been reviewed for applicability in the M-X shelter air blast efforts. These models when utilized with the HULL code (in its interactive dust mode) should be appropriate for assessing the relative importance of dust to the air blast loads on the shelter. Because of the two dimensional effects associated with precursor related phenomena it will be necessary to perform the HULL calculations, designed to assess the importance of dust, also in two dimensions.

Since the models recommended in this report are not yet validated and future advances are anticipated, calculations assessing the importance of dust to M-X should be looked at as engineering estimates rather than definitive representation of the free-field environments.

10.3 SUMMARY AND CONCLUSIONS FOR EXPERIMENTAL PROGRAM PLANNING

Air blast loads predictions for the M-X shelter should be experimentally verified. Both classical and precursor wave forms should be included as well as the effects of shock incidence angle.

Laboratory shock tubes, in particular the CERF 13-inch Shock Tube, provide a convenient, cost effective approach to verifying the predictions.

REFERENCES

1. Issa, R. and Hove, D. "Airblast Loading on the MX Shelter," SAI-77-553-LA (briefing to DNA), Dec. 1976.

2. Ganong, G.P. and Whitaker, W.A., "The Nuclear Blast Precursor," report unpublished.

3. Chambers, B.,"Thermal Layer Predictor," AFWL-TN-76-2, Air Force Weapons Laboratory, Kirtland Air Force Base, NM, 1976.

4. Brode, H.L., "A Review of Nuclear Explosion Phenomena Pertinent to Protective Construction," RAND Report R-425-PR, 1964.

5. Nuclear Weapons Blast Phenomena, DASA 1200-IV, Defense Nuclear Agency, 1973.

6. Air Force Manual for Design and Analysis of Hardened Structure, AFWL-TR-74-102, 1974.

7. Carpenter, H.J., and Brode, H.L., "Height of Burst Air Blast at High Overpressure," Defense Nuclear Agency, 4059T, January 1975.

8. Srinivasa, D., Private communication, December 1976.

9. Chambers, B.S. and Fry, M.A., "AFWL HULL Calculations of 1 MT at 1500 ft (Precursed) Over Ramp-Type Structure," 25 September 1975.

10. Martens, D.P., Capt. USAF and Bradshaw, J.C., 1 Lt. USAF, "Dynamic Airblast Simulator Parametric Test Series, Events I-A, I-B, I-C, I-D, and I-E Data Report," November 1976.

11. Private communication J. Keefer; precursed waveforms, report unpublished.

12. Fry, M.A., Capt. USAF, Ganong, G.P., Maj.USAF and Aubrey, J.W., "Effects on Nonideal Surface on Airblast from One-Megaton Yields," February 1978.

13. Chambers, B., et al., "1 MT Precursor Calculations," AFWL-TN-75-12, Air Force Weapons Laboratory, Kirtland Air Force Base, NM, 1975.

14. Mansfield, J.E., et al.,"HOB Effects on Dust Lofting Mechanisms," report unpublished.

15. Lanz, J.C., "Temperature Distribution Along the Ground in the Thermal Layer Produced by a Nuclear Explosion," report unpublished.

REFERENCES
(continued)

16. Murphy, B.F., "Operation BUSTER, Some Measurements of Overpressure-Time versus Distance for Airburst Bombs," WT-304, March 1952.

17. Porzel, F.B., "HOB for Atomic Bombs," report unpublished.

18. Broida, T.R., et al., "Air Temperatures in the Vicinity of a Nuclear Detonation, Operation TUMBLER," WT-542, September 1952.

19. Inn, E.C., "Air Temperature Measurements over Several Surfaces," WT-1149, 1957.

20. McLoughlin, R.C., "Operation TUMBLER Sound Velocity Changes Near the Ground in the Vicinity of an Atomic Explosion," WT-546, March 1953.

21. McLoughlin, R.C. and Foushee, F.C., "Sound Velocities Near the Ground in the Vicinity of an Atomic Explosion, Operation UPSHOT-KNOTHOLE," WT-776, January 1955.

22. Santilli, A. and Steward, H., "Operation TUMBLER, Mechanically Recorded Measurements of Air Temperature Near the Ground," report unpublished.

23. Moulton, J., "Nuclear Weapons Blast Phenomena, Vol. II," report unpublished.

24. Scoville,H., et al., "Operation TUMBLER, Final Summary Report," report unpublished.

25. Salmon,V., "Operation TUMBLER, Air Pressure versus Time," WT-512, February 1953.

26. Shelton, F.H., "The Precursor, its Formation, Prediction, and Effects," report unpublished.

27. Bouton, E.H., et al., "Operation TUMBLER, Preshock Dust, WT-519, 1952.

28. Broida, A., et al., "Operation TUMBLER, Thermal Radiation from a Nuclear Detonation," WT-543, March 1953.

29. Morris, W.E., et al., "Operation UPSHOT-KNOTHOLE, Program 1.1a and 1.2, Air Blast Measurements," report unpublished.

30. Swift, L.M. and Sachs, D.C., "Operation UPSHOT-KNOTHOLE, Program 1.1b, Air Pressure and Ground Shock Measurements," report unpublished.

REFERENCES
(continued)

31. Broyles, C.D., "Dynamic Pressure versus Time and Supporting Air Blast Measurements, Operation UPSHOT-KNOTHOLE," WT-714, February 1954.

32. Shreve, J.D., "Operation UPSHOT-KNOTHOLE, Program 1.1c, Air Shock Pressure-Time versus Distance from a Tower Shot," report unpublished.

33. "Operation UPSHOT-KNOTHOLE, Summary Report of the Technical Director," report unpublished.

34. Moulton, J.F. and Walthall, E.R., "Operation TEAPOT, Project I.V., Shock Wave Photography," WT-1102, May 1958.

35. "Operation TEAPOT, Technical Summary," report unpublished.

36. Gordon, M.G., et al., "Operation TEAPOT Dust Density versus Time and Distance in the Shock Wave," WT-1113, June 1967.

37. McLoughlin, R.C., "Operation TUMBLER, Project 1.5, Preshock Sound Velocities Near the Ground in the Vicinity of an Atomic Explosion," WT-1104.

38. "Operation TEAPOT, Technical Photography," report unpublished.

39. "Operation TEAPOT, Blast Photography," report unpublished.

40. "Operation REDWING, Shock Photography," report unpublished.

41. "Operation REDWING, Blast Measurements," report unpublished.

42. "Operation REDWING, Thermal Measurements," report unpublished.

43. "Operation REDWING, Documentary Photography," WT-1363.

44. Bryant, E.J. and Keefer, J.H., "Operation PLUMBBOB, Basic Airblast Phenomena," report unpublished.

45. "Operation PLUMBBOB, Non-Ideal Blast Effects," report unpublished.

46. Swatosh, J.J., Jr., et al., "Nuclear Weapons Effects: Dust and Air Temperature Environment," Construction Engineering Research Laboratory Technical Manuscript S-2R, extracted from a final technical report prepared by IIT Research Institute under Contract DACA 73-67-C-0018, February 1971.

47. Trulio, J.G., et al., "The Lofting of Debris and Particulate Ejecta by Blast-Induced Surface Shear," Applied Theory, Inc., ATR-770-14-3(A), 1972.

48. Kirsch, J.W. and Welch, J.E., "Dust Lofting Capabilities of Air Blast Wave Flow Fields," report unpublished.

49. Hartenbaum, B., "Lofting of Particulates by a High Speed Wing," Applied Theory, Inc. Report No. ATR-71-25, DNA 2737, September 1971.

50. Ausherman, D. "Initial Dust Lofting: Shock Tube Experiments," TRW Systems Group Report No. 21830-6003-RU-00, DNA 3162F, September 1973.

51. Landau, L. and Lifshitz, E., Fluid Mechanics, Pergamon Press Ltd (Addison-Wesley, Reading, Mass.) 1959 (U.S.A. Printing 1968).

52. Powers, J. et al., "Precursor Sweep-Up Dust Cloud Model and Thermal Layer Model Development," Science Applications, Inc. Report No. SAI-75-594-WA, December 1975 (to be published as a DNA report).

53. Knasel, T.M., "Experimental Studies of Soil Thermal Irradiation, Vol. I - Soil Blow-Off Data Analysis," Science Applications, Inc. Report No. SAI-78-540-WA, April 1977 (to be published as a DNA report).

54. Chambers, B., et al., "Theoretical Calculations of Early Phenomenology--200 KT at 32 KM," report unpublished.

55. Chambers, B., AFWL FB10 User Tape, 1966, report unpublished.

56. Glass, I.I. and Hall, J.G., "Handbook of Supersonic Aerodynamics, Section 18, Shock Tubes," NAVORD Report 1488 (Vol. 6), December 1959.

57. "Principles and Application of Shock Tubes and Shock Tunnels," NASA TM-X-69941, October 1963.

58. Personal communication from AFWL/DYM.

59. Personal communication with M. Whitliff, CALSPAN.

60. "Blast and Shock Simulation Facilities in the United Kingdom, Canada, and the United States," DASA 1627 Revised, March, 1967.

61. Personal communication with J. Keefer, BRL.

62. Personal communication with R. Dannenberg, NASA Ames.

63. Personal communication with N. Baum, CERF.

64. Personal communication with K. Seifert, Physics International.

65. Needham, C.E., "Theoretical Calculations for a Precursor Simulation," March 1968.

66. Chambers, B., et al., "AFWL HULL Calculations of 1 MT at 1500 Feet Over Ideal and Heated Surfaces," March 1976.

67. Griffith, W.C., "Interaction of a Shock Wave with a Thermal Boundary Layer," Journal of Aerospace Sciences, January 1956.

68. Gion, E., "Ballistic Research Laboratories Simulate Nuclear Burst Thermal Layer," Army Research Magazine, also, BRL 1899, "Plane Shock-Thermal Layer Interactions," July 1976.

69. Carslaw, H.S. and Jaeger, J.C., Conduction of Heat in Solids, 2nd Edition, Oxford Press, 1959.

70. Personal communication with J. Dishon, SAI.

71. Ausherman, D.R., "Interaction of Blast Waves with Thermal Layers," TRW Systems Group, DNA 3786F, 19 January 1976.

72. Brown, G.L. and Rebello, M.R., "A Small, Fast-Response Probe to Measure Composition of a Binary Gas Mixture," AIAA Journal, May 1972, pp 649 to 652.

73. Personal communication with J. Keefer, BRL.

74. Liner, R.T., et al., "Nuclear Precursor Phenomenology and Sweep-up Dust Cloud Model Development," DNA 3781F (SAI-74-627-WA) November 1975.

PRECEDING PAGE BLANK

APPENDIX A

PRECURSOR WAVEFORMS

Ample evidence exists from nuclear tests (Reference 73) that nonclassical (precursor) waveforms are created as a result of an interaction of thermal radiation with the ground. The precursor directly results from the propagation of the air blast into the heated (higher sound speed) air in front of the nuclear blast wave. Thus a wave, the precursor gets ahead of the flow above it forming a toe. The nonlinear hydrodynamics causes the precursor waveforms to be characterized by a slow,* irregular rise to the peak overpressure. A two-dimensional representation of the shock wave geometry and relevant variables (Figure 27) introduces a scheme for calculating the precursor properties developed by SAI (Reference 74). A shock fixed coordinate system was employed, and the crucial assumption was made that the shock geometry is steady in this coordinate system. The solid lines correspond to shock waves, the dashed line corresponds to a contact surface, the wavy solid line corresponds to the slipstream, and the solid-dashed lines are for reference purposes. This technique has met with appreciable success in modeling various aspects of the flow.

*Slow when compared to the shock over an ideal surface, the latter which essentially rises instantaneously.

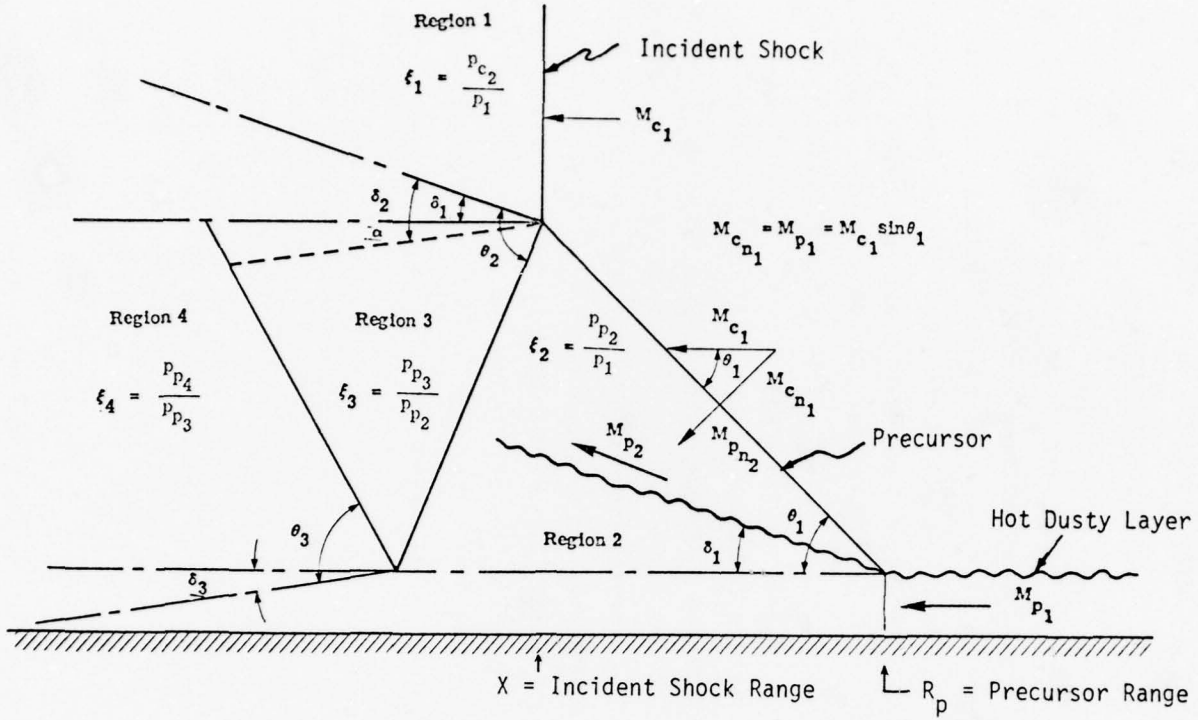

Figure 27. Schematic representation of precursor flow field

The oblique portion of the precursor wave is calculated from

$$\theta_1 = \sin^{-1}(M_{p_1}/M_{c_1}) \ . \tag{50}$$

and the pressure jump across the precursor is determined from

$$\xi_2 \equiv \frac{p_{p_2}}{p_1} = \frac{2\gamma M_{c_1}^2 \sin^2\theta_1 - (\gamma - 1)}{\gamma + 1} \tag{51}$$

which in functional notation may be expressed as

$$\xi_2 = f(M_{c_1}, \theta_1) \ . \tag{52}$$

The inclination from the horizontal of the slipstream in the precursor region is given by

$$\delta_1 = \tan^{-1}\left[\frac{2\cot\theta_1(M_{c_1}^2 \sin^2\theta_1 - 1}{2+M_{c_1}^2(\gamma+1 - 2\sin^2\theta_1)}\right] \tag{53}$$

Using the above quantities, the Mach number may be determined as

$$M_{p_2} = \sqrt{\frac{(\gamma-1)\xi_2 + (\gamma+1)}{2\gamma\xi_2}} \Big/ \sin(\theta_1-\delta_1) \tag{54}$$

which may be expressed in functional form as

$$M_{p_2} = \frac{g(\xi_2)}{\sin(\theta_1-\delta_1)} \ . \tag{55}$$

The above expressions define all the relevant quantities in region 2 in Figure 27.

In order to define the properties in regions 3 and 4, an iterative procedure is used. First, the properties in region 3 are approximated by assuming a value for the inclination from the horizontal, α, of the slipstream. As a first approximation, it is assumed that

$$\delta_2 = \delta_1 + \alpha_i \ . \tag{56}$$

Knowing δ_2 and M_{p_2}, it is possible to determine the shock angle, θ_2, from the following relation:

$$\sin^6\theta_2 + b \sin^4\theta_2 + c \sin^2\theta_2 + d = 0 \tag{57}$$

where

$$b = \left(\frac{M_{p_2}^2 + 2}{M_{p_2}^2} \right) - \gamma \sin^2\delta_2$$

$$c = \frac{2M_{p_2}^2 + 1}{M_{p_2}^4} + \left[\frac{(\gamma+1)^2}{4} + \frac{\gamma-1}{M_{p_2}^2} \right] \sin^2\delta_2$$

$$d = - \frac{\cos^2\delta_2}{M_{p_2}^4} \ .$$

The above equation is a cubic equation in $\sin^2\theta$ and is solved by a trigonometric method. Having found the appropriate root for the above equation and hence found the value of θ_2, the pressure ratio and Mach number in region 3 may be determined from

$$\xi_3 \equiv \frac{p_{p_3}}{p_{p_2}} = f(M_{p_2}, \theta_2) \tag{58}$$

$$M_{p_3} = \frac{g(\xi_3)}{\sin(\theta_2 - \delta_2)} \quad . \tag{59}$$

Now recall that in region 4 the flow must be parallel to the ground surface, so that

$$\delta_3 = \alpha \tag{60}$$

and θ_3 is found from Equation (57) using M_{p_3} and δ_3 in place of M_{p_2} and δ_2. The pressure ratio and the Mach number in region 4 are then determined from

$$\xi_4 \equiv \frac{p_{p_4}}{p_{p_3}} = f(M_{p_3}, \theta_3) \tag{61}$$

$$M_{p_4} = \frac{g(\xi_4)}{\sin(\theta_3 - \alpha)} \quad . \tag{62}$$

After these quantities have been determined, a test is made in order to determine if the pressure in region 4 is equal to the pressure in region 1, that is

$$\xi_2 x \xi_3 x \xi_4 = \xi_1 = \frac{p_{c_2}}{p_1} \quad . \tag{63}$$

If this requirement on the pressure is not satisfied, regions 3 and 4 properties are recomputed with

$$\delta_2 = \delta_1 + \alpha_{i+1} \tag{64}$$

where

$$\alpha_{i+1} = \alpha_i + \phi$$

and ϕ is an increment in the slipstream inclination that may be either positive or negative depending on whether the pressure in region 4 is either less than or greater than the pressure in region 1. The iteration procedure continues until the requirements on the flow deflection and the pressure in region 4 are satisfied. When these requirements are satisfied, the velocities (with the coordinate system fixed at ground zero) in the precursor regions are defined as follows:

Region 2:

$$a_{p_2} = a_1 \sqrt{\xi_2 \left[\frac{(\gamma-1)\xi_2+(\gamma+1)}{(\gamma+1)\xi_2+(\gamma-1)} \right]} = a_1 \eta\ (\xi_2) \tag{65}$$

$$U_{p_2} = M_{p_2}\ a_{p_2} \tag{66}$$

$$u_{p_2} = U_p - U_{p_2} \cos\delta_1 \tag{67}$$

$$v_{p_2} = U_{p_2} \sin\delta_1 \tag{68}$$

Region 3:

$$a_{p_3} = a_{p_2}\, \eta(\xi_3) \tag{69}$$

$$U_{p_3} = M_{p_3}\, a_{p_3} \tag{70}$$

$$u_{p_3} = U_p - U_{p_3} \cos\delta_2 \tag{71}$$

$$v_{p_3} = U_{p_3} \sin\delta_2 \tag{72}$$

Region 4:

$$a_{p_4} = a_{p_3}\, \eta(\xi_4) \tag{73}$$

$$U_{p_4} = M_{p_4}\, a_{p_4} \tag{74}$$

$$u_{p_4} = U_p - U_{p_4} \tag{75}$$

$$v_{p_4} = 0\ . \tag{76}$$

The above calculation procedure may be used to determine the precursor region flow field properties at any given instant of time after precursor formation.

PRECEDING PAGE BLANK

APPENDIX B

SPECIFIC ENERGY OF BLOW-OFF

In Section 6, a simple analytical model was described for the shielding of the ground surface by dust that had already been blown off into the air. This was then combined with an assumption for dust blow-off to give the total blow-off mass as a function of fluence. The purpose of this appendix is to indicate the experimental support for a blow-off law of the form

$$dM = dQ/E \tag{77}$$

where dM is the mass blown off, dQ is the fluence received at the surface, and E is a specific energy of blow-off (units of cal/gm). This appendix is included for convenience, an earlier version can be found in Reference 14. Essentially this model is attributable to Mansfield while at SAI.

An estimate of the specific energy of mass removal (radiant energy per gram of surface material removed) can be made from the data on gross mass removal in the solar furnace tests for an NTS soil denoted "14 NTS." In these tests, a number of soil samples were exposed to rather large thermal fluences, and weight losses were established by before-and-after weighing. To determine the specific energy of mass removal, it is then necessary to establish the total fluence received by the surface during the experiment. This is somewhat less than the total incident solar fluence due to attenuation of the later part of the pulse by the dust blown off in the earlier part of the pulse. The total fluence received by the surface was measured by a calorimeter at the surface and indeed indicated a lower surface flux toward the end of the exposure. This is described by a transmission factor f(Q), defined as the fraction of the incident solar flux that reaches the

surface after a total incident fluence Q has been received, that is, at time t

$$\begin{aligned} &\text{Incident flux} && \dot{Q} \\ &\text{Incident fluence} && Q = \dot{Q}t \\ &\text{Surface flux} && \dot{Q}' = f(Q)\ \dot{Q} \\ &\text{Surface fluence} && Q' = \int f(Q)\ \dot{Q}dt \\ & && \quad = \int f(Q)dQ \end{aligned} \tag{78}$$

The experimental surface fluence Q' and blow-off mass M were then combined for each test to give a specific energy of mass removal

$$E = \frac{Q'}{M}, \tag{79}$$

Twenty experimental values for this quantity ranged from 5 to 17.5 kj/gm. There was some indication that this quantity depended on incident flux, but the correlation was not significant ($r^2 < 0.53$). As a result, the data for all flux levels were considered together. To examine the statistical distribution, the data were coded in seven groups starting with E=5 as follows:

Group	From	To
1	5	6.11
2	6.11	7.46
3	7.46	9.11
4	9.11	11.13
5	11.13	13.59
6	13.59	16.6
7	16.6	20.2

These are groups of equal width for ln(E). A linear regression analysis was then performed on the coded data, giving a lognormal distribution with a median E_o = 9.44 kj/gm and an error factor f = 1.83, so that 80% of the values are expected to lie in the range E/f to Ef. The correlation coefficient for this regression was 0.984. The resulting values for the specific energy of mass removal for this soil are

$$5.15 < E < 17.3 \quad \text{kj/gm, 80\% CL}$$

$$E_o = 9.44 \quad \text{kj/gm (median)} \tag{80}$$

$$= 2260 \quad \text{cal/gm.}$$

Thus with 80% CL, the specific energy of blow-off is bounded by

$$1230 < E < 4140 \quad \text{cal/gm of material blown-off} \tag{81}$$

More recent data are included in Section 7 where the recommendations are made regarding dust modeling for air blast calculations.

PRECEDING PAGE BLANK

APPENDIX C

SAI Model for a Truncated Fireball

This appendix describes the truncated fireball model developed by Pomraning and extracted from the reference. (Reference 14). The effective yield for growing fireballs can be treated dynamically to ensure continuity between results.

Fireball Shape Factor

Consider the case of a near-surface burst, for which the fireball intersects the ground. The quantity of interest is $j(r)$, the flux of radiant energy normal to the ground at ground range r. Let the fireball radiate at the range S cal/cm^2-sec. The fireball is assumed to be a diffuse radiator, so the angular distribution of the source is given by

$$f(\mu) = \frac{\mu}{\pi};\ 2\pi \int_0^1 f(\mu)\, d\mu = 1 \tag{82}$$

where μ is the cosine of the angle between the radiation direction and the normal to the radiating surface. Referring to Figure 28 for the complete geometrical nomenclature, $j(r)$ is given by

$$j(r) = \frac{S}{\pi} \int \frac{\mu \cos n}{R^2} \, dA \tag{83}$$

where the integration is over the area of the above-ground portion of the sphere. Referring to the quantity $j/S \equiv K(r, h, R_f)$ as the fireball shape factor

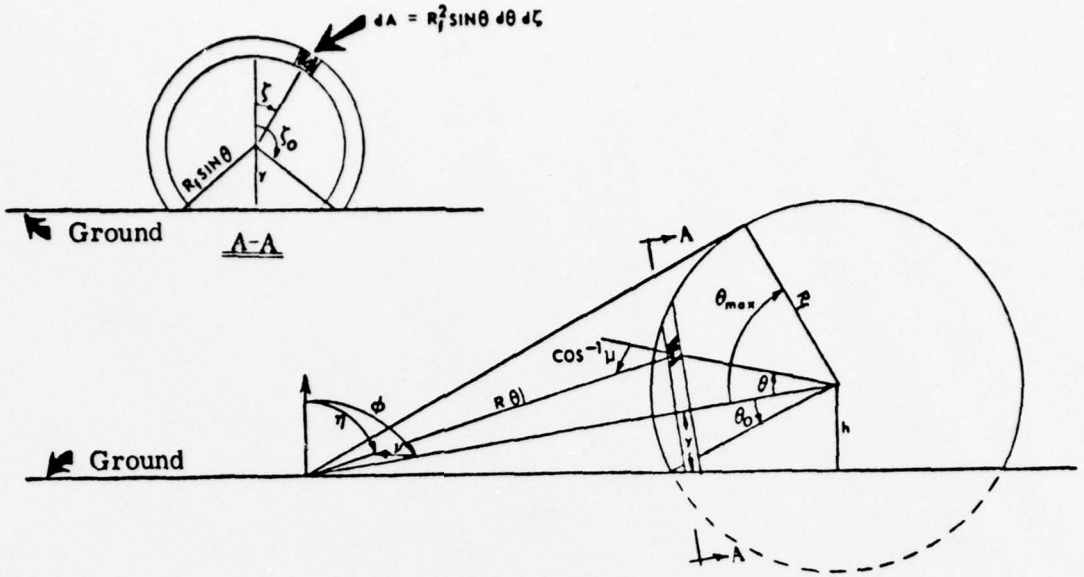

Figure 28. Geometric nomenclature used in derivation of fireball shape factor.

$$K(r, h, R_f) = \frac{1}{\pi} \int_0^{\theta_{max}} \int_{-\zeta_0}^{\zeta_0} \left(\frac{\mu \cos\eta}{R^2} \right) R_f^2 \sin\theta \, d\zeta \, d\theta \quad . \tag{84}$$

The following relationships are required to evaluate the double integral:

$$\cos\eta = \cos\nu \cos\phi + \sin\nu \sin\phi \cos\zeta$$

$$\zeta_0 = \begin{cases} \cos^{-1}(-\cot\nu \cot\phi) & \theta_0 \leq \theta \leq \theta_{max} \\ \pi & 0 \leq \theta \leq \theta_0 \end{cases} .$$

After performing the necessary work to evaluate the integrals, the result can be written as

$$K = \frac{1}{2} + \frac{\sigma}{\pi\gamma^3} \cos^{-1}\left(-\frac{\sigma}{\rho} \sqrt{\gamma^2 - 1} \right) - \frac{1}{\pi} \sin^{-1}\left(\sqrt{\frac{\gamma^2 - 1}{\rho}} \right) - \frac{\sqrt{\gamma^2 - 1}\sqrt{1 - \sigma^2}}{\pi\gamma^2} \tag{85}$$

$$\left(0 \leq \sigma \leq 1, \ \rho \geq \sqrt{1 - \sigma^2} \right)$$

where

$$\sigma = h/R_f$$

$$\rho = r/R_f$$

$$\gamma^2 = \sigma^2 + \rho^2 = \frac{h^2 + r^2}{R_f^2} \quad .$$

For a true air burst, the integration is much more straightforward, since $\zeta_0 = \pi$ over the entire range of θ. For that case

$$K = \frac{\sigma}{\gamma^3} \qquad (\sigma \geq 1,\ \rho \geq 1) \quad . \tag{86}$$

To illustrate the importance of the above formulation, Figure 29 shows the difference between the normal flux as computed by the extended source model and as computed by a point source model as a function of h/R_f, at a ground range corresponding to two source radii. The point source model rapidly becomes inadequate as the fireball height decreases below a fireball radius. With the source centered on the ground, i.e., for a true surface burst, the point source model incorrectly gives zero normal flux at all ranges because of the cosine factor which enters into the normal flux formula. For true air bursts, the extended source and point source models are equivalent.

Although h and r, and their dimensionless counterparts σ and ρ, have been treated as independent variables, they may depend on other variables or parameters. In particular, h and σ are functions of time when fireball rise is taken into account.

Effective Yield and Fireball Radius for Near-Surface Bursts

Detailed fireball calculations have not been made for surface or near-surface bursts, i.e., for fireballs which intersect the ground. However, it has been widely accepted that for bursts very near the surface, most of the energy incident upon the ground is reradiated back into the fireball. Qualitatively, the fireball might appear as a truncated version of a fireball from a slightly higher-than-actual-yield air burst. Taking this viewpoint, an approximation of this effect has been incorporated into our model in terms of a single parameter, which may be interpreted as an effective "reflection" coefficient.

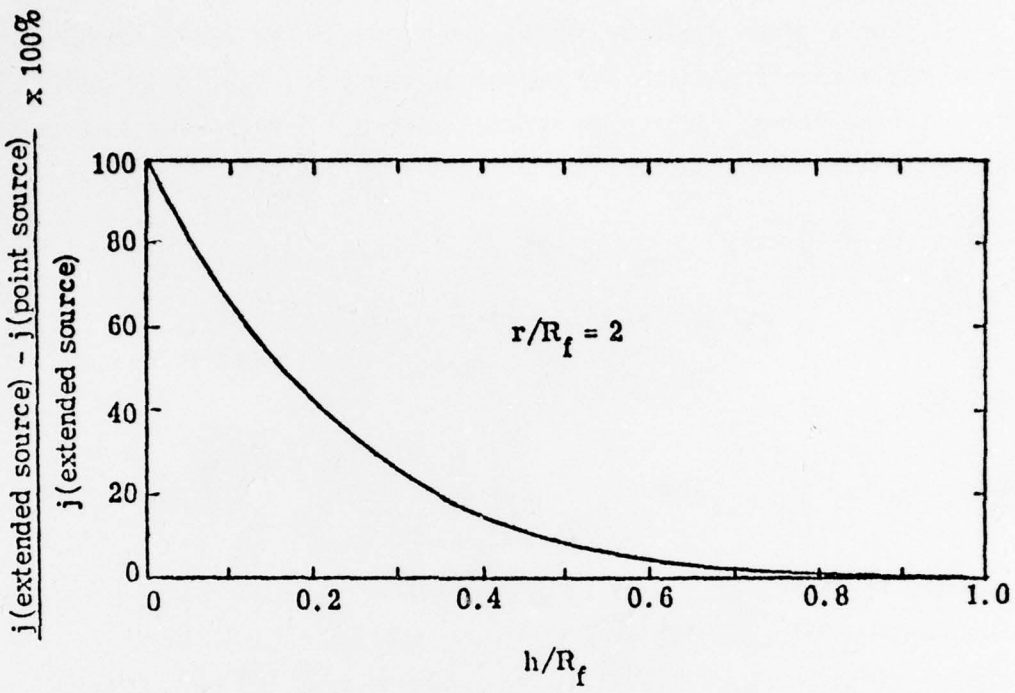

Figure 29. Percent error of point source as a function of h/R_f for $r/R_f = 2$.

For a given yield W, let R_f and V denote the radius and volume of an air burst fireball. For height of burst h ($<R_f$) let R_f' and V' refer to the actual (truncated sphere) fireball. Referring to Figure 30 for further nomenclature, the volumes involved are

$$V = \frac{4}{3}\pi R_f^3$$

$$V_2 = \frac{\pi}{3}(R_f-h)^2(2R_f+h) \qquad (87)$$

$$V_1 = V - V_2$$

$$V' = \frac{4}{3}\pi(R_f')^3 - \frac{\pi}{3}(R_f' - h)^2(2R_f'+h).$$

Assuming fireballs have uniform energy densities, the energy that would have normally occupied V_2 is $W V_2/V$. Introducing the effective "reflection" coefficient ($0 \leq f \leq 1$), it is assumed that the fraction f of this energy is returned to the fireball. The energy contained in the actual fireball, denoted by W', is then $(V_1/V + f V_2/V)W$, or

$$W' = \left[1 - \frac{V_2}{V}(1 - f)\right] W \equiv \omega W \qquad (88)$$

which also defines ω. Finally, it is assumed that the actual fireball adjusts itself so that the energy density is the same as it would be in an air burst of the same yield, i.e., $W'/V' = W/V$, which is equivalent to $V'/V = W'/W = \omega$. Combining the expressions for ω, V_2 and V, introducing the dimensionless parameters $\sigma \equiv h/R_f$ and $x = R_f'/R_f$ and rearranging gives

$$x^3 + \frac{3}{2}\sigma x^2 - \left(\frac{\sigma^3 + 4\omega}{2}\right) = 0 \qquad (89)$$

where

$$4\omega = 4 - (1-f)(1-\sigma)^2(2+\sigma) \quad . \qquad (90)$$

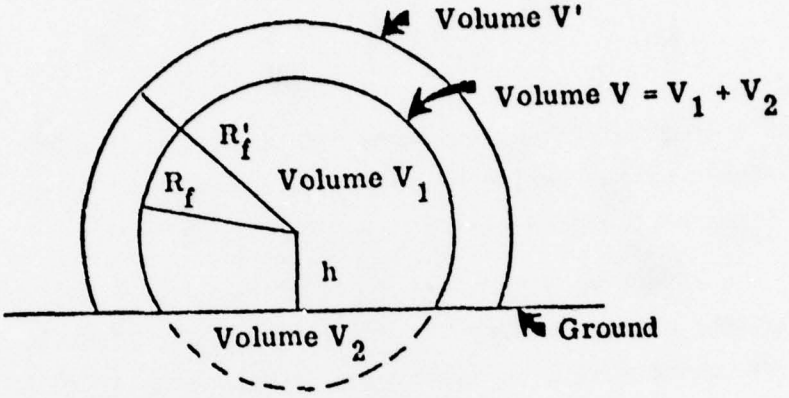

Figure 30. Nomenclature for derivation of effective reflection coefficient.

The real solution of the cubic equation in x is

$$x \equiv \frac{R_f'}{R_f} = \frac{1}{2}\left\{\left[\sqrt{\sigma^3 + 4\omega} + \sqrt{4\omega}\right]^{2/3} + \left[\sqrt{\sigma^3 + 4\omega} - \sqrt{4\omega}\right]^{2/3} - \sigma\right\} . \quad (91)$$

This equation gives the approximate radius of a near-surface burst fireball in terms of the radius of an air burst fireball of the same yield and in terms of the parameter f.

The effective yield, W_{eff}, is defined as the yield that would give the same energy density in a full sphere of radius R_f' as in the truncated sphere which, by assumption, is the same as in an air burst fireball of the true yield. Hence

$$W_{eff} = W\left(\frac{R_f'}{R_f}\right)^3 = Wx^3 \quad . \quad (92)$$

W_{eff} is used in the empirical yield-scaling relationships which give the thermal output and the thermal pulse shape.

For a surface burst ($h = \sigma = 0$) and for $f = 1$ (total "reflection"), $W_{eff} = 2W$ and $R_f' = 2^{1/3}R_f$. For $h = R_f$ ($\sigma = 1$), $W_{eff} = W$ and $R_f' = R_f$ for all values of f. For $f = 0$ (no "reflection"), $W_{eff} = W$ and R_f' for all heights of burst. In general, as illustrated in Figure 31, the above procedure assures a smooth transition to the true air burst parameters as h increases regardless of the value of f selected.

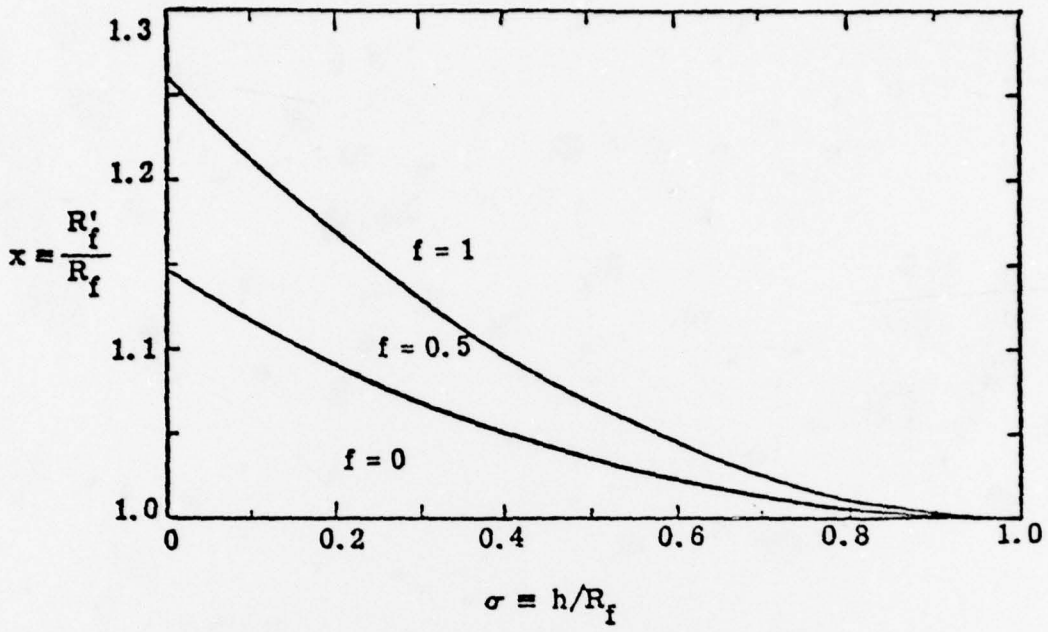

Figure 31a. Variation of $x \equiv R'_f/R_f$ with scaled burst height.

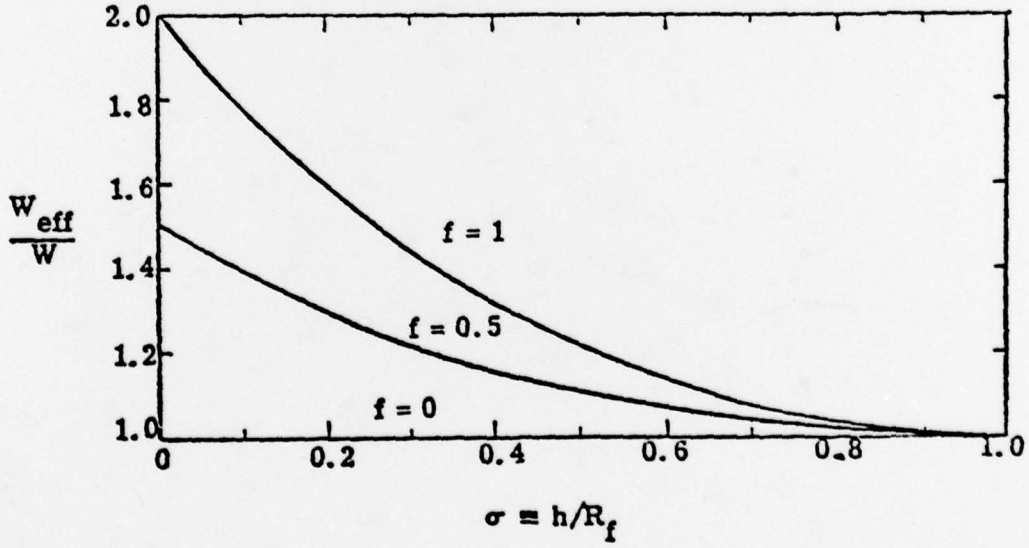

Figure 31b. Variation of effective yield with scaled burst height.

PRECEDING PAGE BLANK

DISTRIBUTION LIST

DEPARTMENT OF DEFENSE

Assistant to the Secretary of Defense
ATTN: Executive Assistant

Defense Advanced Rsch. Proj. Agency
ATTN: TIO

Defense Civil Preparedness Agency
Assistant Director for Research
ATTN: Staff Dir. Rsch., G. Sisson
10 cy ATTN: Admin. Officer

Defense Communications Agency
ATTN: CCTC C670, R. Lipp
ATTN: CCTC/672, F. Moore
ATTN: Code 930

Defense Documentation Center
12 cy ATTN: DD

Defense Intelligence Agency
ATTN: DB-4C, E. O'Farrell
ATTN: DT-1C
ATTN: DT-2
ATTN: RDS-3A
ATTN: DB-4E

Defense Nuclear Agency
ATTN: DDST
4 cy ATTN: TITL
3 cy ATTN: SPSS

Department of Defense Explo. Safety Board
ATTN: T. Zaker

Field Command, Defense Nuclear Agency
ATTN: FCT
ATTN: FCPR
ATTN: FCTMOF

Joint Strat. Tgt. Planning Staff
ATTN: NRI-Stinfo, Library
ATTN: DOXT
ATTN: XPFS
ATTN: JLTW-2

Livermore Division, Field Command, DNA
Department of Defense
ATTN: FCPRL

Under Secy of Def. for Rsch. & Engrg.
ATTN: Strategic & Space Systems (OS)

WWMCCS System Engineering Org.
ATTN: T. Neighbors

DEPARTMENT OF THE ARMY

BMD Advanced Technology Center
Department of the Army
ATTN: 1CRDABH-X
ATTN: CRDABH-S

BMD Program Office
Department of the Army
ATTN: DACS-BMT, J. Shea

DEPARTMENT OF THE ARMY (Continued)

Chief of Engineers
Department of the Army
ATTN: DAEN-RDM
ATTN: DAEN-MCE-D

Deputy Chief of Staff for Ops. & Plans
Department of the Army
ATTN: DEP. Dir. for Nuc. Chem. Matters
ATTN: MOCA-ADL

Harry Diamond Laboratories
Department of the Army
ATTN: DELHD-N-NP
ATTN: DELHD-N-TI

U.S. Army Ballistic Research Labs.
ATTN: DRXBR-BLE, W. Taylor
ATTN: DRDAR-BLE, J. Keefer
ATTN: DRXBR-X, J. Meszaros
2 cy ATTN: Technical Library

U.S. Army Communications Command
ATTN: Technical Reference Division

U.S. Army Engineer Center
ATTN: ATSEN-SY-L

U.S. Army Engineer Div., Huntsville
ATTN: HNDED-SR

U.S. Army Engr. Waterways Exper. Station
ATTN: L. Ingram
ATTN: Library
ATTN: W. Flathau

U.S. Army Foreign Science & Tech. Ctr.
ATTN: Research & Concepts Branch

U.S. Army Material & Mechanics Rsch. Ctr.
ATTN: J. Mescall
ATTN: Technical Library
ATTN: R. Shea

U.S. Army Materiel Dev. & Readiness Cmd.
ATTN: DRXAM-TL
ATTN: DRCDE-D, L. Flynn

U.S. Army Nuclear & Chemical Agency
ATTN: Library

DEPARTMENT OF THE NAVY

Civil Engineering Laboratory
Naval Construction Battalion Center
ATTN: S. Takahashi
ATTN: Code L08A

David W. Taylor Naval Ship R & D Ctr.
ATTN: Code L42-3

Naval Facilities Engineering Command
ATTN: Code 09M22C
ATTN: Code 03A
ATTN: Code 04B

DEPARTMENT OF THE NAVY (Continued)

Naval Material Command
ATTN: MAT 08T-22

Naval Ocean Systems Center
ATTN: Code 4471
ATTN: E. Cooper

Naval Research Laboratory
ATTN: Code 8440, F. Rosenthal
ATTN: Code 2627

Naval Surface Weapons Center
ATTN: Code F31

Commander
Naval Surface Weapons Center
Dahlgren Laboratory
ATTN: Tech. Library & Info. Services Branch

Naval Weapons Center
ATTN: P. Cordle
ATTN: C. Austin
ATTN: Code 533

Naval Weapons Evaluation Facility
ATTN: Code 10
ATTN: R. Hughes

Office of Naval Research
ATTN: Code 474, N. Perrone
ATTN: Code 715
ATTN: Code 461, J. Warner

Office of the Chief of Naval Operations
ATTN: OP 981
ATTN: OP 03EG

Strategic Systems Project Office
ATTN: NSP-272
ATTN: NSP-43

DEPARTMENT OF THE AIR FORCE

Aerospace Defense Command/XPD
ATTN: XP
ATTN: XPDQQ

Air Force Geophysics Laboratory
ATTN: LWW, K. Thompson
ATTN: SUOL Research Library

Air Force Institute of Technology, Air University
ATTN: Library

Air Force Systems Command
ATTN: DLCAM

Air Force Weapons Laboratory
ATTN: DE-I
ATTN: DE, M. Plamondon
ATTN: DES-C, R. Henny
ATTN: SUL
ATTN: DEX
ATTN: DEP

Assistant Chief of Staff
Intelligence
ATTN: IN

DEPARTMENT OF THE AIR FORCE (Continued)

Deputy Chief of Staff
Research, Development, & Acq.
ATTN: AFRDPX
ATTN: AFRDQSM

Deputy Chief of Staff
Programs & Resources
ATTN: PRE

Foreign Technology Division, AFSC
ATTN: NICD, Library

Rome Air Development Center, AFSC
ATTN: Documents Library/TSLD

Aeronautical Systems Division
ATTN: Technical Library

Space & Missile Systems Organization/DE
Air Force Systems Command
ATTN: DEB

Space & Missile Systems Organization/DY
Air Force Systems Command
ATTN: DYS

Space & Missile Systems Organization/MN
Air Force Systems Command
ATTN: MNNH
ATTN: MMH

Strategic Air Command/XPFS
ATTN: NRI-STINFO, Library
ATTN: XPFS

DEPARTMENT OF ENERGY

Lawrence Livermore Laboratory
ATTN: Doc. Con. for Technical Information
Dept. Library

Los Alamos Scientific Laboratory
ATTN: Doc. Con. for Reports Library

Office of Military Application
ATTN: Doc. Con. for Test Office

Sandia Laboratories
Livermore Laboratory
ATTN: Doc. Con. for Library & Security
Classification Div.

Sandia Laboratories
ATTN: Doc. Con. for 3141
ATTN: Doc. Con. for A. Chaban
ATTN: Doc. Con. for L. Vortman

DEPARTMENT OF DEFENSE CONTRACTORS

Aerospace Corp
ATTN: P. Mathur
ATTN: Tech. Info. Services

Agbabian Associates
ATTN: M. Agbabian

Avco Research & Systems Group
ATTN: Library, A830

DEPARTMENT OF DEFENSE CONTRACTORS (Continued)

BDM Corp.
ATTN: Corporate Library
ATTN: A. Lavagnino

BDM Corp.
ATTN: R. Hensley

Boeing Co.
ATTN: R. Holmes
ATTN: Aerospace Library

Battelle Memorial Institute
ATTN: Technical Library
ATTN: R. Klingsmith

California Research & Technology, Inc.
ATTN: K. Kreyenhagen
ATTN: Library

Civil/Nuclear Systems Corp.
ATTN: J. Bratton

Eric H. Wang
Civil Engineering Rsch. Fac.
The University of New Mexico
ATTN: N. Baum

Gard, Inc.
ATTN: G. Neidhardt

General Electric Co.-TEMPO
Center for Advanced Studies
ATTN: DASIAC

Engineering Decision Analysis Co., Inc.
ATTN: R. Kennedy

General Research Corp.
Santa Barbara Division
ATTN: B. Alexander

IIT Research Institute
ATTN: Documents Library

University of Illinois, Consulting Services
ATTN: N. Newmark

Institute for Defense Analyses
ATTN: Classified Library

J. H. Wiggins, Co., Inc.
ATTN: J. Collins

Kaman AviDyne
Division of Kaman Sciences Corp.
ATTN: Library
ATTN: E. Criscione

Kaman Sciences Corp.
ATTN: F. Shelton
ATTN: Library

Lockheed Missiles & Space Co., Inc.
ATTN: TIC-Library

Physics International Co.
ATTN: Technical Library
ATTN: C. Vincent
ATTN: F. Sauer

DEPARTMENT OF DEFENSE CONTRACTORS (Continued)

R & D Associates
ATTN: J. Carpenter
ATTN: C. MacDonald
ATTN: W. Wright, Jr.
ATTN: Technical Information Center
ATTN: H. Brode
ATTN: A. Latter

R & D Associates
ATTN: H. Cooper

Rand Corp.
ATTN: C. Mow

Science Applications, Inc.
ATTN: Technical Library

Science Applications, Inc.
ATTN: B. Chambers, III

Science Applications, Inc.
ATTN: D. Hove
ATTN: R. Issa

Southwest Research Institute
ATTN: A. Wenzel
ATTN: W. Baker

SRI International
ATTN: G. Abrahamson

Systems, Science & Software, Inc.
ATTN: D. Grine
ATTN: Library
ATTN: T. Cherry
ATTN: T. Riney

TRW Defense & Space Sys. Group
ATTN: P. Bhutta
ATTN: I. Alber
ATTN: Technical Information Center
ATTN: D. Baer
ATTN: R. Plebuch
2 cy ATTN: P. Dai

TRW Defense & Space Sys. Group
San Bernardino Operations
ATTN: E. Wong

Weidlinger Assoc., Consulting Engineers
ATTN: M. Baron

Weidlinger Assoc., Consulting Engineers
ATTN: J. Isenberg